

ТОНКИЕ ХИМИЧЕСКИЕ ТЕХНОЛОГИИ Chemical

Technologies

- Theoretical Bases of Chemical Technology
- **Chemistry and Technology of Organic Substances**
- Chemistry and Technology of Medicinal Compounds and Biologically **Active Substances**
- **Biochemistry and Biotechnology**
- Synthesis and Processing of Polymers and Polymeric Composites
- Chemistry and Technology of Inorganic Materials
- Analytical Methods in Chemistry and Chemical Technology
- Mathematical Methods and Information Systems in Chemical Technology



18(2) 2023



ТОНКИЕ XИМИЧЕСКИЕ Fine Chemical Technologies

Tonkie Khimicheskie Tekhnologii = Fine Chemical Technologies

Vol. 18, No. 2, 2023

Тонкие химические технологии = Fine Chemical Technologies **Том 18, № 2, 2023**

https://doi.org/10.32362/2410-6593-2023-18-2 www.finechem-mirea.ru

Theoretical Bases of Chemical Technology

Chemistry and Technology of Organic Substances

Chemistry and Technology of Medicinal Compounds and Biologically Active Substances

Biochemistry and Biotechnology

Synthesis and Processing of Polymers and Polymeric Composites

Chemistry and Technology of Inorganic Materials

Analytical Methods in Chemistry and Chemical Technology

Mathematical Methods and Information Systems in Chemical Technology

https://doi.org/10.32362/2410-6593

Tonkie Khimicheskie Tekhnologii = Fine Chemical Technologies 2023, Vol. 18, No. 2

The peer-reviewed scientific and technical journal Fine Chemical Technologies highlights the modern achievements of fundamental and applied research in the field of fine chemical technologies, including theoretical bases of chemical technology, chemistry and technology of medicinal compounds and biologically active substances, organic substances and inorganic materials, biochemistry and biotechnology, synthesis and processing of polymers and polymeric composites, analytical and mathematical methods and information systems in chemistry and chemical technology.

Founder and Publisher

Federal State Budget
Educational Institution of Higher Education
"MIREA – Russian Technological University"
78, Vernadskogo pr., Moscow, 119454, Russian Federation.
Publication frequency: bimonthly.
The journal was founded in 2006. The name was Vestnik MITHT

until 2015 (ISSN 1819-1487).

The journal is included into the List of peer-reviewed science

press of the State Commission for Academic Degrees and Titles of the Russian Federation.

The journal is indexed:

SCOPUS, DOAJ, Chemical Abstracts, Science Index, RSCI, Ulrich's International Periodicals Directory

Editor-in-Chief:

Andrey V. Timoshenko – Dr. Sci. (Eng.), Cand. Sci. (Chem.),
Professor, MIREA – Russian Technological University,
Moscow, Russian Federation. Scopus Author ID 56576076700,
ResearcherID Y-8709-2018,
https://orcid.org/0000-0002-6511-7440,
timoshenko@mirea.ru

Deputy Editor-in-Chief:

Valery V. Fomichev – Dr. Sci. (Chem.), Professor, MIREA – Russian Technological University, Moscow, Russian Federation. Scopus Author ID 57196028937, http://orcid.org/0000-0003-4840-0655, fomichev@mirea.ru

Executive Editor:

Sergey A. Durakov – Cand. Sci. (Chem.), Associate Professor, MIREA – Russian Technological University, Moscow, Russian Federation, Scopus Author ID 57194217518, ResearcherID AAS-6578-2020, http://orcid.org/0000-0003-4842-3283, durakov@mirea.ru

Editorial staff:

Managing Editor Science editors

Desktop publishing

Cand. Sci. (Eng.) Galina D. Seredina Dr. Sci. (Chem.), Prof. Tatyana M. Buslaeva Dr. Sci. (Chem.), Prof. Anatolii A. Ischenko Dr. Sci. (Eng.), Prof. Valery F. Kornyushko Dr. Sci. (Eng.), Prof. Anatolii V. Markov Dr. Sci. (Chem.), Prof. Yuri P. Miroshnikov Dr. Sci. (Chem.), Prof. Vladimir A. Tverskoy Larisa G. Semernya

86, Vernadskogo pr., Moscow, 119571, Russian Federation. Phone: +7 (499) 600-80-80 (#31288)

E-mail: seredina@mirea.ru

The registration number ΠΗ № ΦC 77–74580 was issued in December 14, 2018 by the Federal Service for Supervision of Communications, Information Technology, and Mass Media of Russia.

The subscription index of Pressa Rossii: 36924

ISSN 2686-7575 (Online)

Тонкие химические технологии = Fine Chemical Technologies 2023, том 18, № 2

Научно-технический рецензируемый журнал «Тонкие химические технологии» освещает современные достижения фундаментальных и прикладных исследований в области тонких химических технологий, включая теоретические основы химической технологии, химию и технологию лекарственных препаратов и биологически активных соединений, органических веществ и неорганических материалов, биохимию и биотехнологию, синтез и переработку полимеров и композитов на их основе, аналитические и математические методы и информационные системы в химии и химической технологии.

Учредитель и издатель

федеральное государственное бюджетное образовательное учреждение высшего образования «МИРЭА – Российский технологический университет» 119454, РФ, Москва, пр-т Вернадского, д. 78. Периодичность: один раз в два месяца. Журнал основан в 2006 году. До 2015 года издавался под названием «Вестник МИТХТ» (ISSN 1819-1487).

Журнал входит в Перечень ведущих рецензируемых научных журналов ВАК РФ.

Индексируется:

SCOPUS, DOAJ, Chemical Abstracts, РИНЦ (Science Index), RSCI, Ulrich's International Periodicals Directory

Главный редактор:

Тимошенко Андрей Всеволодович – д.т.н., к.х.н., профессор, МИРЭА – Российский технологический университет, Москва, Российская Федерация. Scopus Author ID 56576076700, ResearcherID Y-8709-2018, https://orcid.org/0000-0002-6511-7440, timoshenko@mirea.ru

Заместитель главного редактора:

Фомичёв Валерий Вячеславович — д.х.н., профессор, МИРЭА — Российский технологический университет, Москва, Российская Федерация. Scopus Author ID 57196028937, http://orcid.org/0000-0003-4840-0655, fomichev@mirea.ru

Выпускающий редактор:

Дураков Сергей Алексеевич – к.х.н., доцент, МИРЭА – Российский технологический университет, Москва, Российская Федерация, Scopus Author ID 57194217518, ResearcherID AAS-6578-2020, http://orcid.org/0000-0003-4842-3283, *durakoy@mirea.ru*

Редакция:

Зав. редакцией Научные редакторы

к.т.н. Г.Д. Середина д.х.н., проф. Т.М. Буслаева д.х.н., проф. А.А. Ищенко д.т.н., проф. В.Ф. Корнюшко д.т.н., проф. А.В. Марков д.х.н., проф. Ю.П. Мирошников д.х.н., проф. В.А. Тверской Л.Г. Семерня

Компьютерная верстка

119571, Москва, пр. Вернадского, 86, оф. Л-119. Тел.: +7 (499) 600-80-80 (#31288) E-mail: seredina@mirea.ru

Регистрационный номер и дата принятия решения о регистрации СМИ: ПИ $\mbox{N}_{\mbox{\tiny $}}$ ФС 77-74580 от 14.12.2018 г. СМИ зарегистрировано Федеральной службой по надзору в сфере связи, информационных технологий и массовых коммуникаций (Роскомнадзор).

Индекс по Объединенному каталогу «Пресса России»: 36924

© MIREA - Russian Technological University, 2023

Editorial Board

Andrey V. Blokhin – Dr. Sci. (Chem.), Professor, Belarusian State University, Minsk, Belarus. Scopus Author ID 7101971167, ResearcherID AAF-8122-2019 https://orcid.org/0000-0003-4778-5872 blokhin@bsu.by.

Sergey P. Verevkin – Dr. Sci. (Eng.), Professor, University of Rostock, Rostock, Germany. Scopus Author ID 7006607848, ResearcherID G-3243-2011, https://orcid.org/0000-0002-0957-5594, sergey.verevkin@uni-rostock.de.

Konstantin Yu. Zhizhin – Corresponding Member of the Russian Academy of Sciences (RAS), Dr. Sci. (Chem.), Professor, N.S. Kurnakov Institute of General and Inorganic Chemistry of the RAS, Moscow, Russian Federation. Scopus Author ID 6701495620, ResearcherID C-5681-2013, http://orcid.org/0000-0002-4475-124X, kyuzhizhin@igic.ras.ru.

Igor V. Ivanov – Dr. Sci. (Chem.), Professor, MIREA – Russian Technological University, Moscow, Russian Federation.
Scopus Author ID 34770109800, ResearcherID I-5606-2016, http://orcid.org/0000-0003-0543-2067, ivanov_i@mirea.ru.

Carlos A. Cardona – PhD (Eng.), Professor, National University of Columbia, Manizales, Colombia. Scopus Author ID 7004278560, http://orcid.org/0000-0002-0237-2313, ccardonaal@unal.edu.co.

Oskar I. Koifman—Academician at the RAS, Dr. Sci. (Chem.), Professor, President of the Ivanovo State University of Chemistry and Technology, Ivanovo, Russian Federation.

Scopus Author ID 6602070468, ResearcherID R-1020-2016, http://orcid.org/0000-0002-1764-0819, president@isuct.ru.

Elvira T. Krut'ko – Dr. Sci. (Eng.), Professor, Belarusian State Technological University, Minsk, Belarus. Scopus Author ID 6602297257, ela krutko@mail.ru.

Anatolii I. Miroshnikov — Academician at the RAS, Dr. Sci. (Chem.), Professor, M.M. Shemyakin and Yu.A. Ovchinnikov Institute of Bioorganic Chemistry of the RAS, Member of the Presidium of the RAS, Chairman of the Presidium of the RAS Pushchino Research Center, Moscow, Russian Federation.

Scopus Author ID 7006592304, ResearcherID G-5017-2017, aiv@ibch.ru.

Aziz M. Muzafarov – Academician at the RAS, Dr. Sci. (Chem.), Professor, A.N. Nesmeyanov Institute of Organoelement Compounds of the RAS, Moscow, Russian Federation.

Scopus Author ID 7004472780, ResearcherID G-1644-2011,

https://orcid.org/0000-0002-3050-3253,

aziz@ineos.ac.ru.

Редакционная коллегия

Блохин Андрей Викторович – д.х.н., профессор Белорусского государственного университета, Минск, Беларусь. Scopus Author ID 7101971167, ResearcherID AAF-8122-2019 https://orcid.org/0000-0003-4778-5872 blokhin@bsu.by.

Верёвкин Сергей Петрович – д.т.н., профессор Университета г. Росток, Росток, Германия. Scopus Author ID 7006607848, ResearcherID G-3243-2011, https://orcid.org/0000-0002-0957-5594, sergey.verevkin@uni-rostock.de.

Жижин Константин Юрьевич – член-корр. Российской академии наук (РАН), д.х.н., профессор, Институт общей и неорганической химии им. Н.С. Курнакова РАН, Москва, Российская Федерация. Scopus Author ID 6701495620, ResearcherID C-5681-2013, http://orcid.org/0000-0002-4475-124X, kyuzhizhin@jgic.ras.ru.

Иванов Игорь Владимирович – д.х.н., профессор, МИРЭА – Российский технологический университет, Москва, Российская Федерация. Scopus Author ID 34770109800, ResearcherID I-5606-2016, http://orcid.org/0000-0003-0543-2067, ivanov i@mirea.ru.

Кардона Карлос Ариэль – PhD, профессор Национального университета Колумбии, Манизалес, Колумбия. Scopus Author ID 7004278560, http://orcid.org/0000-0002-0237-2313, ccardonaal@unal.edu.co.

Койфман Оскар Иосифович – академик РАН, д.х.н., профессор, президент Ивановского государственного химико-технологического университета, Иваново, Российская Федерация. Scopus Author ID 6602070468, ResearcherID R-1020-2016, http://orcid.org/0000-0002-1764-0819, president@isuct.ru.

Крутько Эльвира Тихоновна – д.т.н., профессор Белорусского государственного технологического университета, Минск, Беларусь. Scopus Author ID 6602297257, ela krutko@mail.ru.

Мирошников Анатолий Иванович – академик РАН, д.х.н., профессор, Институт биоорганической химии им. академиков М.М. Шемякина и Ю.А. Овчинникова РАН, член Президиума РАН, председатель Президиума Пущинского научного центра РАН, Москва, Российская Федерация. Scopus Author ID 7006592304, ResearcherID G-5017-2017, aiv@ibch.ru.

Музафаров Азиз Мансурович – академик РАН, д.х.н., профессор, Институт элементоорганических соединений им. А.Н. Несмеянова РАН, Москва, Российская Федерация. Scopus Author ID 7004472780, ResearcherID G-1644-2011, https://orcid.org/0000-0002-3050-3253, aziz@ineos.ac.ru.

Ivan A. Novakov — Academician at the RAS, Dr. Sci. (Chem.), Professor, President of the Volgograd State Technical University, Volgograd, Russian Federation.

Scopus Author ID 7003436556, ResearcherID I-4668-2015, http://orcid.org/0000-0002-0980-6591, president@vstu.ru.

Alexander N. Ozerin – Corresponding Member of the RAS, Dr. Sci. (Chem.), Professor, Enikolopov Institute of Synthetic Polymeric Materials of the RAS, Moscow, Russian Federation.

Scopus Author ID 7006188944, ResearcherID J-1866-2018, https://orcid.org/0000-0001-7505-6090, ozerin@ispm.ru.

Tapani A. Pakkanen – PhD, Professor, Department of Chemistry, University of Eastern Finland, Joensuu, Finland.
Scopus Author ID 7102310323,
tapani.pakkanen@uef.fi.

Armando J.L. Pombeiro – Academician at the Academy of Sciences of Lisbon, PhD, Professor, President of the Center for Structural Chemistry of the Higher Technical Institute of the University of Lisbon, Lisbon, Portugal. Scopus Author ID 7006067269, ResearcherID I-5945-2012, https://orcid.org/0000-0001-8323-888X, pombeiro@ist.utl.pt.

Dmitrii V. Pyshnyi – Corresponding Member of the RAS, Dr. Sci. (Chem.), Professor, Institute of Chemical Biologyand Fundamental Medicine, Siberian Branch of the RAS, Novosibirsk, Russian Federation.

Scopus Author ID 7006677629, ResearcherID F-4729-2013, https://orcid.org/0000-0002-2587-3719, pyshnyi@niboch.nsc.ru.

Alexander S. Sigov – Academician at the RAS, Dr. Sci. (Phys. and Math.), Professor, President of MIREA – Russian Technological University, Moscow, Russian Federation.

Scopus Author ID 35557510600, Researcher ID L-4103-2017, sigov@mirea.ru.

Alexander M. Toikka – Dr. Sci. (Chem.), Professor, Institute of Chemistry, Saint Petersburg State University, St. Petersburg, Russian Federation. Scopus Author ID 6603464176, ResearcherI D A-5698-2010, http://orcid.org/0000-0002-1863-5528, a.toikka@spbu.ru.

Andrzej W. Trochimczuk – Dr. Sci. (Chem.), Professor, Faculty of Chemistry, Wrocław University of Science and Technology, Wrocław, Poland. Scopus Author ID 7003604847, andrzej.trochimczuk@pwr.edu.pl.

Aslan Yu. Tsivadze – Academician at the RAS, Dr. Sci. (Chem.), Professor, A.N. Frumkin Institute of Physical Chemistry and Electrochemistry of the RAS, Moscow, Russian Federation. Scopus Author ID 7004245066, ResearcherID G-7422-2014, tsiv@phyche.ac.ru.

Новаков Иван Александрович – академик РАН, д.х.н., профессор, президент Волгоградского государственного технического университета, Волгоград, Российская Федерация. Scopus Author ID 7003436556, ResearcherID I-4668-2015, http://orcid.org/0000-0002-0980-6591, president@vstu.ru.

Озерин Александр Никифорович – член-корр. РАН, д.х.н., профессор, Институт синтетических полимерных материалов им. Н.С. Ениколопова РАН, Москва, Российская Федерация. Scopus Author ID 7006188944, ResearcherID J-1866-2018, https://orcid.org/0000-0001-7505-6090, ozerin@ispm.ru.

Пакканен Тапани – PhD, профессор, Департамент химии, Университет Восточной Финляндии, Йоенсуу, Финляндия. Scopus Author ID 7102310323, tapani.pakkanen@uef.fi.

Помбейро Армандо — академик Академии наук Лиссабона, PhD, профессор, президент Центра структурной химии Высшего технического института Университета Лиссабона, Португалия. Scopus Author ID 7006067269, ResearcherID I-5945-2012, https://orcid.org/0000-0001-8323-888X, pombeiro@ist.utl.pt.

Пышный Дмитрий Владимирович – член-корр.РАН, д.х.н., профессор, Институт химической биологии и фундаментальной медицины Сибирского отделения РАН, Новосибирск, Российская Федерация. Scopus Author ID 7006677629, ResearcherID F-4729-2013, https://orcid.org/0000-0002-2587-3719, pyshnyi@niboch.nsc.ru.

Сигов Александр Сергеевич – академик РАН, д.ф.-м.н., профессор, президент МИРЭА – Российского технологического университета, Москва, Российская Федерация. Scopus Author ID 35557510600, ResearcherID L-4103-2017, sigov@mirea.ru.

Тойкка Александр Матвеевич – д.х.н., профессор, Институт химии, Санкт-Петербургский государственный университет, Санкт-Петербург, Российская Федерация. Scopus Author ID 6603464176, Researcher ID A-5698-2010, http://orcid.org/0000-0002-1863-5528, a.toikka@spbu.ru.

Трохимчук Андржей – д.х.н., профессор, Химический факультет Вроцлавского политехнического университета, Вроцлав, Польша. Scopus Author ID 7003604847, andrzej.trochimczuk@pwr.edu.pl.

Цивадзе Аслан Юсупович – академик РАН, д.х.н., профессор, Институт физической химии и электрохимии им. А.Н. Фрумкина РАН, Москва, Российская Федерация. Scopus Author ID 7004245066, ResearcherID G-7422-2014, tsiv@phyche.ac.ru.



18(2) 2023

CONTENTS

СОДЕРЖАНИЕ

Theoretical Bases of Chemical Technology

Klauzner P.S., Rudakov D.G., Anokhina E.A., Timoshenko A.V.

Application of diabatic extractive distillation schemes with preliminary separation of azeotropic components for separation of acetone—toluene—*n*-butanol mixture

Kolesnikova I.N., Lobanov N.V., Lobanov V.N., Shishkov I.F.

Quantum chemical research of the molecular structure of 3,4-dicyanofuroxan

Synthesis and Processing of Polymers and Polymeric Composites

Brekhova K.A., Simonov-Emel'yanov I.D., Pykhtin A.A.

Projection of structure and compositions of resistance to burning polymer composite materials with flame retardants based on magnesium hydroxide

Теоретические основы химической технологии

Клаузнер П.С., Рудаков Д.Г., Анохина Е.А., Тимошенко А.В.

83 Применение схем неадиабатической экстрактивной ректификации с предварительным отделением азеотропообразующих компонентов для разделения смеси ацетон—толуол—н-бутанол

Колесникова И.Н., Лобанов Н.В., Лобанов В.Н., Шишков И.Ф.

98 Исследование равновесной структуры молекулы 3,4-дицианофуроксана

Синтез и переработка полимеров и композитов на их основе

Брехова К.А., Симонов-Емельянов И.Д., Пыхтин А.А.

109 Проектирование структуры и составов стойких к горению полимерных композиционных материалов с наполнителямиантипиренами на основе гидроксида магния

Vasilyev I.Yu.
Biocomposite materials
based on polyethylene and amphiphilic
polymer-iron metal complex

Analytical Methods in Chemistry and Chemical Technology

Ischenko A.A., Lazov M.A., Mironova E.V., Putin A.Yu., Ionov A.M., Storozhenko P.A. Analysis of nanoparticles and nanomaterials using X-ray photoelectron spectroscopy

Васильев И.Ю.

123 Биокомпозиционные материалы на основе полиэтилена и амфифильного полимерного металлокомплекса железа

Аналитические методы в химии и химической технологии

Ищенко А.А., Лазов М.А., Миронова Е.В., Путин А.Ю., Ионов А.М., Стороженко П.А.

135 Анализ наночастиц и наноматериалов методом рентгеновской фотоэлектронной спектроскопии

THEORETICAL BASES OF CHEMICAL TECHNOLOGY

теоретические основы химической технологии

ISSN 2686-7575 (Online)

https://doi.org/10.32362/2410-6593-2023-18-2-83-97

UDC 660:51.001.57+66



RESEARCH ARTICLE

Application of diabatic extractive distillation schemes with preliminary separation of azeotropic components for separation of acetone—toluene—*n*-butanol mixture

Pavel S. Klauzner[∞], Danila G. Rudakov, Elena A. Anokhina, Andrey V. Timoshenko

MIREA – Russian Technological University (M.V. Lomonosov Institute of Fine Chemical Technologies), Moscow, 119571 Russia

[™]Corresponding author, e-mail: klauzner@mirea.ru

Abstract

Objectives. The study aims to investigate the effectiveness of the use of various options for organizing the process of diabatic distillation in the separation of a mixture of acetone–toluene–n-butanol by extractive distillation using dimethylformamide as an entrainer in a scheme with preliminary separation of azeotropic components.

Methods. As the main research method, mathematical modeling in the Aspen Plus V. 12 software package was used. As a model for describing vapor-liquid equilibrium, the local composition Non-Random Two Liquid equation model was used. Parametric optimization of diabatic schemes was carried out according to the criterion of reduced energy costs.

Results. Based on the scheme for extractive distillation of an acetone-toluene-n-butanol mixture with preliminary separation of azeotropic components, five options for organizing diabatic distillation schemes were considered, both with and without use of a compressor to reach a required flows temperature.

Conclusion. It is shown that the use of diabatic schemes in the extractive distillation of a acetone–toluene–n-butanol mixture with dimethylformamide makes it possible to diminish the reduced energy costs by 8.9–43.5%. Meanwhile the maximum reduction in energy consumption is achieved in a scheme where upper vapor flows of two other columns are used to heat the azeotropic components separating column.

Keywords: extractive distillation, heat integration, diabatic distillation, energy saving

For citation: Klauzner P.S., Rudakov D.G., Anokhina E.A., Timoshenko A.V. Application of diabatic extractive distillation schemes with preliminary separation of azeotropic components for separation of acetone–toluene–n-butanol mixture. Tonk. Khim. Tekhnol. = Fine Chem. Technol. 2023;18(2):83–97 (Russ., Eng.). https://doi.org/10.32362/2410-6593-2023-18-2-83-97

НАУЧНАЯ СТАТЬЯ

Применение схем неадиабатической экстрактивной ректификации с предварительным отделением азеотропообразующих компонентов для разделения смеси ацетон—толуол—*н*-бутанол

П.С. Клаузнер[™], Д.Г. Рудаков, Е.А. Анохина, А.В. Тимошенко

МИРЭА – Российский технологический университет (Институт тонких химических технологий им. М. В. Ломоносова), Москва, 119571 Россия
[™]Автор для переписки, e-mail: klauzner@mirea.ru

Аннотация

Цели. Исследование энергетической эффективности применения неадиабатической экстрактивной ректификации при разделении смеси ацетон-толуол-н-бутанол с диметилформамидом в качестве разделяющего агента в схеме с предварительным отделением азеотропообразующих компонентов.

Методы. В качестве основного метода исследования применялось математическое моделирование с использованием программного комплекса Aspen Plus V. 12. Моделирование парожидкостного равновесия производилось по уравнению локальных составов Non-Random Two Liquid. Параметрическая оптимизация неадиабатических схем проводилась по критерию приведенных энергетических затрат.

Результаты. На основе схемы экстрактивной ректификации смеси ацетон-толуол-н-бутанол с предварительным отделением азеотропообразующих компанентов было рассмотрено пять вариантов организации схем неадиабатической ректификации, как с использованием компрессора для достижения необходимой температуры потоков, так и без него. **Выводы.** Показано, что применение неадиабатической экстрактивной ректификации в схеме разделения смеси ацетон-толуол-н-бутанол с диметилформамидом с предварительным отделением азеотропообразующих компонентов позволяет снизить приведенные энергетические затраты на 8.9–43.5%, при этом максимальное снижение энергозатрат достигается в схеме с использованием для обогрева колонны отделения азеотропообразующих компонентов верхних паровых потоков двух других колонн.

Ключевые слова: экстрактивная ректификация, теплоинтеграция, недиабатическая ректификация, энергосбережение

Для цитирования: Клаузнер П.С., Рудаков Д.Г., Анохина Е.А., Тимошенко А.В. Применение схем неадиабатической экстрактивной ректификации с предварительным отделением азеотропообразующих компонентов для разделения смеси ацетон—толуол—*н*-бутанол. *Тонкие химические технологии*. 2023;18(2):83—97. https://doi.org/10.32362/2410-6593-2023-18-2-83-97

INTRODUCTION

The extractive distillation (ED) method is used in the basic organic and petrochemical synthesis industries to separate non-ideal mixtures. However, the use of ED in large-tonnage processes is associated with significant energy consumption, which makes reducing energy costs for its implementation an important task. As in the case of conventional distillation, various methods can be used for this, including internal [1–3] and external [4–6] thermal integration, as well as a combination of these approaches [7–9].

One approach to reducing energy costs in the ED process involves the use of diabatic distillation schemes, in which the external supply (or removal) of heat to the column plates is carried out by means of integrating heat flows between different scheme devices. Although distillation schemes offer numerous diabatic advantages over other thermal integration approaches the specific [10],features patterns of their application in ED have as yet been little studied.

In a previous work [11], we evaluated the efficiency of the use of diabatic energy distillation in the ED scheme of a mixture of acetone-toluene-n-butanol with dimethylformamide (DMF), in which the entrainer is used in the first column of the scheme. Based on this scheme, four diabatic distillation schemes were proposed, two of which proved to be workable without increasing the pressure of steam flows in compressors, while in the other two, compression of flows in the compressor was necessary to ensure the temperature difference necessary for heat exchange. It was shown that, due to this organization of the diabatic process, the applicable energy costs can be reduced by 11-17%; however, in this case, diabatic distillation schemes with a compressor do not offer significant energy efficiency advantages compared to schemes without a compressor.

The work set out to synthesize diabatic distillation schemes based on another variant of the conventional ED scheme of a mixture of acetone-toluene-*n*-butanol with DMF involving preliminary isolation of azeotrope-forming components (Fig. 1) and evaluate their energy efficiency.

CALCULATION SECTION

Modeling and determination of optimal scheme parameters were performed in the Aspen Plus v.12.1

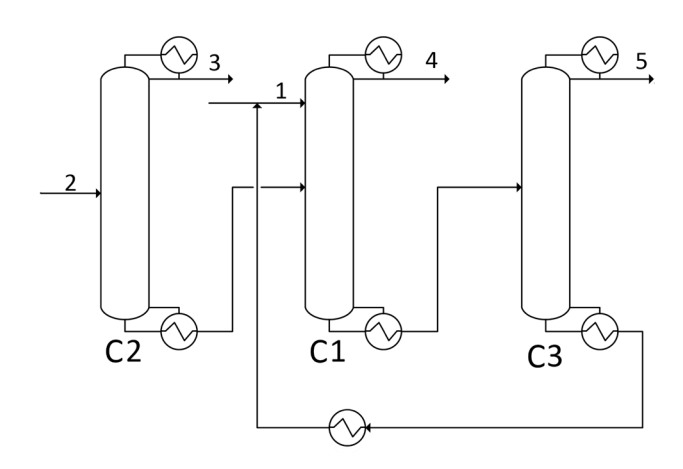


Fig. 1. Scheme of extractive distillation of the acetone–toluene–*n*-butanol mixture with dimethylformamide as the entrainer with preliminary separation of azeotropic components. Hereinafter: C1 – extractive distillation column, C2 – acetone–toluene separation column, C3 – entrainer regeneration column; 1 – entrainer (DMF); 2 – feed; 3 – acetone; 4 – toluene, 5 – *n*-butanol.

software package (*Aspen Technology*, USA). As initial data for the development of diabatic distillation schemes, the results of optimizing the conventional ED scheme of the studied mixture set out in the dissertation of E.A. Anokhina¹ were used (Fig. 1). In order to describe the vapor—liquid equilibrium in the acetone—toluene—*n*-butanol system with DMF, the Non-Random Two Liquid equation of local compositions of, whose parameters were also published by E.A. Anokhina, was used.

As in our previous work [11], the calculations of the schemes were carried out on 1000 kg/h of the initial mixture containing 71.3 wt % acetone, 14.7 wt % toluene, and 14.0 wt % *n*-butanol. The temperature of the feed stream was 61.8°C; the pressure was 101.3 kPa. The pressure of the top of the columns was assumed to be 101.3 kPa; columns with theoretical plates were considered. The calculations were carried out in the design-verification variant having a fixed product flow quality, which was set to be the same as in the work [11] and the dissertation of E.A. Anokhina—namely, at a 99.5 wt % concentration of acetone and n-butanol, a toluene concentration of 99.6 wt %, and a DMF concentration of 99.99 wt %. The optimal operating parameters of the conventional scheme are given in Table 1.

¹ Anokhina E.A. *Extractive distillation in complexes with partially coupled heat and material flows*. Dr. Sci. Thesis (Eng.). Moscow; 2020. 549 p. (in Russ.)

For the practical implementation of diabatic distillation schemes, it is necessary to ensure that the temperature difference of the flow, whose heat is intended for use (i.e., the heat source), as well as the temperature on the plates of the distillation section of the columns into which this heat is directed (the heat receiver), is sufficient to provide the driving force of heat exchange. As in our previous work [11], when modeling schemes, the temperature difference ΔT between the heat source and receiver was assumed to be at least 10°C. To assess the feasibility of implementing diabatic ED schemes with specified heat transfer parameters and preliminary

selection of the required compression ratio $E_{\rm comp}$ in the compressor, an analysis of the temperature profiles of all columns of the conventional scheme was carried out as shown in Fig. 2.

As can be seen, the highest temperatures are observed on the plates of the rectifying sections of columns C1 and C3. Since the temperature on the plates of the rectifying section of column C2 is much lower, only the upper steam flows of columns C1 and C3 were considered for the purposes of ensuring heat transfer in diabatic schemes. Thus, based on the analysis of profiles, five variants of diabatic distillation schemes can be proposed (Fig. 3).

Table 1. Optimal operating parameters of extractive distillation scheme with preliminary separation of azeotropic components (Footnote 1)

Parameters	C1	C2	С3			
$N_{ m total}$	45	18	44			
$N_{_{ m F}}$	35	10	9			
$N_{ m s}$	20	-	-			
$Q_{ m reb},{ m kW}$	92.3	153.1	107.1			
$Q_{\rm cond}$, kW	78.3	146.3	107.1			
R	4.4	0.44	3.7			
$T_{\rm cond}$, °C	110.3	56.2	117.8			
$T_{ m reb}$, $^{\circ}{ m C}$	142.0	105.9	151.8			
S, kg/h	395.3	_	_			
$T_{\rm s}$, °C	100	-	-			
$Q_{ ext{total}}$, kW	352.6					

Note: C1 is the extractive distillation column; C2 is the acetone separation column; C3 is the entrainer regeneration column; N_{total} is the total number of plates in a column; N_{F} is the feed plate number in a column; N_{S} is the number of the plate with the entrainer in a column; Q_{reb} is the reboiler heat duty; Q_{cond} is the condenser heat duty; R is the reflux ratio; T_{cond} is the condenser temperature; T_{reb} is the reboiler temperature; T_{Cond} is the entrainer flow rate; T_{S} is the entrainer temperature; T_{cond} is the total heat duty.

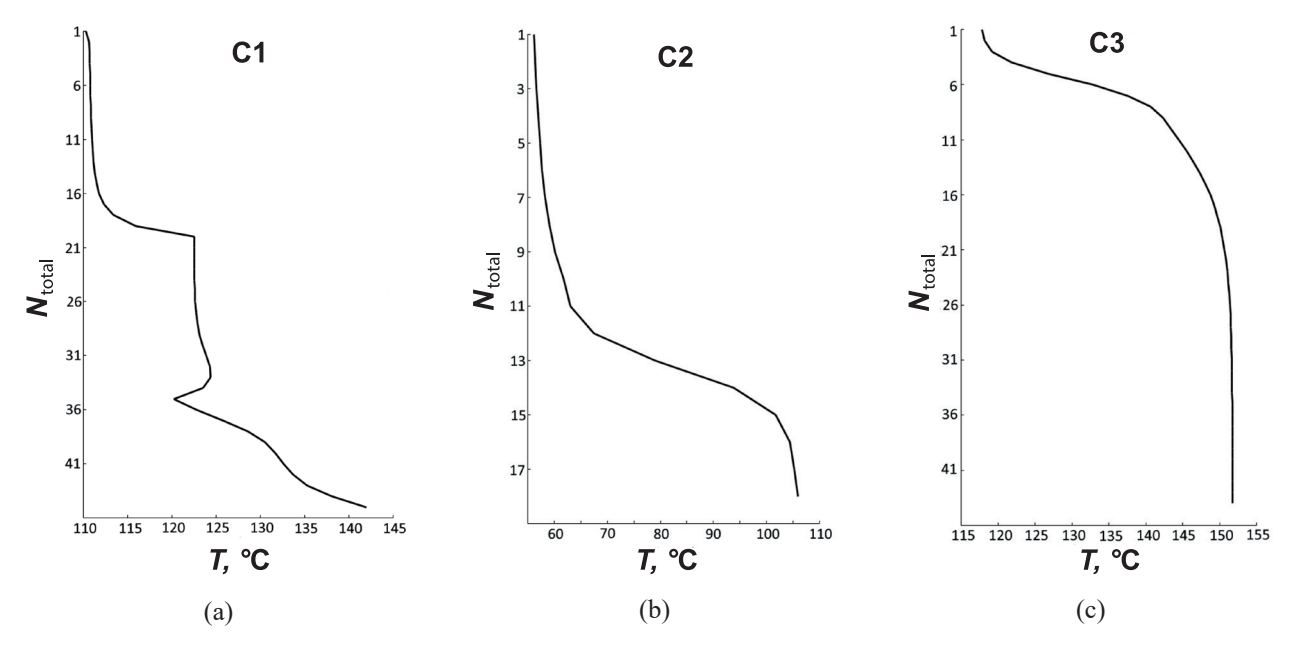


Fig. 2. Temperature profiles of columns of conventional extractive distillation scheme: (a) column C1, (b) column C2, (c) column C3.

Scheme I (Fig. 3a). The upper steam flow of the C3 column is used to heat the C2 column. In this case, the flow temperature is sufficient to provide heat supply to any plate of the distillation section of the C2 column without additional compression.

Scheme II (Fig. 3b). Heating of the C2 column is provided using the upper steam flow of the C1 column. In this case, heat supply without the use of a compressor is possible on plates from the 11th to the 14th.

Scheme III (Fig. 3c). Heating of the C2 column is carried out simultaneously with the use of steam flows of the C1 and C3 columns.

Scheme IV (Fig. 3d). The upper steam flow of column C1 is used to heat column C3. In this case, in order to ensure a given temperature difference ΔT between the heat source and receiver, it is necessary to use a compressor with a compression ratio of at least 2.4.

Scheme V (Fig. 3e). To heat the column C1, the upper steam flow of the column C3 is used. In this case, in order to provide the driving force of heat exchange, it is also necessary to compress the flow with compression ratio $1.6 \leq E_{\rm comp} \leq 2.2$. When $E_{\rm comp} > 2.2$ it is possible to supply heat to the reboiler of the column C1 and, thus, the implementation of an adiabatic scheme with a heat pump.

Note that in the schemes using a compressor, a preheater is installed in front of it to prevent possible cavitation. The thermal duty on the preheater is designated by $Q_{\rm PH}$.

A comparison of diabatic distillation schemes with the conventional ED scheme was carried out according to the criterion of reduced energy costs (Q_{cons}) , which were calculated according to the formula proposed by the authors [12]:

$$Q_{\text{cons}} = Q_{\text{total}} + 3W_{\text{comp}},\tag{1}$$

where $Q_{\rm total}$ is the total energy costs in the column reboilers, kW; $W_{\rm comp}$ is the power consumed by the compressor, kW.

The correct relative evaluation of schemes involves comparing their energy consumption with an optimal set of operating parameters for each of them. The optimal parameters of the conventional ED scheme, which are defined in the dissertation of E.A. Anokhina (Footnote 1), are presented in Table 1.

The criterion for optimizing diabatic schemes was the given energy costs, $Q_{\rm cons}$. The optimization parameters were the position of the heat supply plate to the stripping section of the column, $N_{\rm HE}$; the amount of heat supplied, $Q_{\rm HE}$; and the compression ratio in the compressor, $E_{\rm comp}$, necessary to ensure the accepted value ΔT . At the same time, the optimization procedure had some features for each of the schemes under consideration.

As already mentioned, the temperature of the flow coming out of the top of the column C3 ($T_{\rm cond} = 117.8$ °C) in Scheme I is sufficient

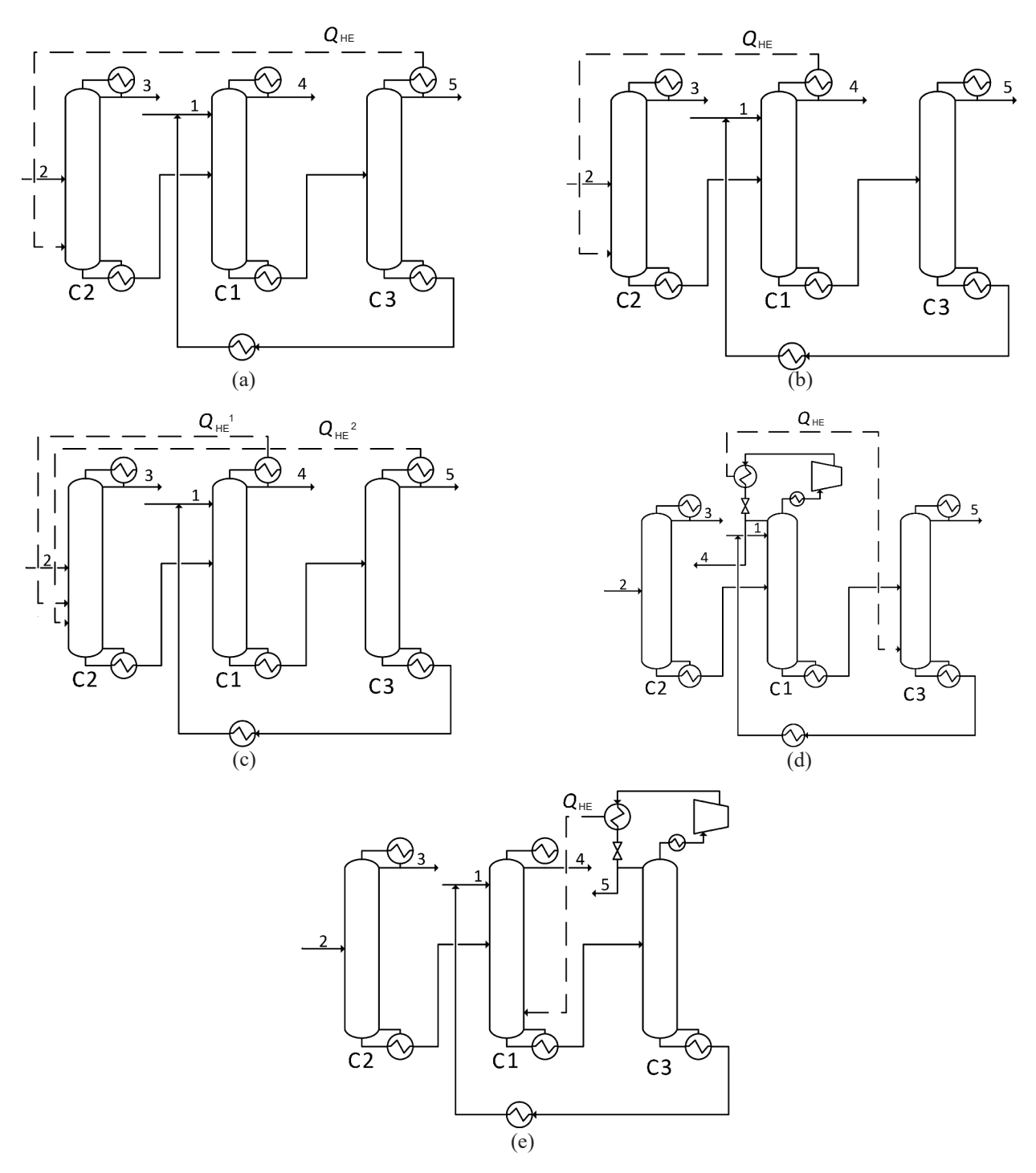


Fig. 3. Diabatic extractive distillation schemes: (a) Scheme I, (b) Scheme II, (c) Scheme III, (d) Scheme IV, (e) Scheme V.

to provide heat supply to any of the plates of the stripping section of the column C2. At the same time, all the heat given off by this flow at full condensation, 107.2 kW, can be used. Thus, for this scheme, the only optimization parameter is the position of the heat supply plate $N_{\rm HE}$. The results reflecting the search for the optimal position of $N_{\rm HE}$ are presented in Table 2.

It can be seen that, the closer the heat supply plate $N_{\rm HF}$ is located to the reboiler, the lower the

reflux ratio and the duty on the column reboiler. The most effective variant is the heat supply to the lower (17th) plate of the column. The optimal operating parameters of Scheme I are presented in Table 3.

The optimization of Scheme II was carried out similarly, the only difference being that here the temperature of the upper steam flow of column C1 ($T_{\rm cond}=110.3\,^{\circ}{\rm C}$) is sufficient only to supply heat to the plates of the distillation section of column C2 from the 11th to the 14th. The results

Table 2. Dependence of the parameters of column C2 for diabatic Scheme I on the position of the heat supply stage N_{HE}

		O C2 LW	R^{C2}
$N_{ m HE}$	$Q_{ m HE}$, kW	$Q_{\rm reb}^{\ \ C2}$, kW	K*-
11	107.2	57.18	0.56
12	107.2	53.38	0.52
13	107.2	51.16	0.52
14	107.2	49.52	0.48
15	107.2	48.20	0.47
16	107.2	47.16	0.46
17	107.2	46.39	0.45

Note: $N_{\rm HE}$ is the heat supply plate number in the heat exchanger; $Q_{\rm HE}$ is the exchanger heat duty; C2 is the acetone separation column; $Q_{\rm reb}^{\rm C2}$ is the reboiler heat duty in C2; $R^{\rm C2}$ is the reflux ratio in C2.

Table 3. Optimal operation parameters for diabatic Scheme I

Parameters	C1	C2	С3			
$N_{ m total}$	45	18	44			
$N_{ m HE}$	-	17	-			
$Q_{\rm reb}$, kW	92.3	46.4	107.1			
R	4.4	0.45	3.7			
Q_{HE} , kW	-	107.2	_			
$Q_{\rm cons}$, kW	245.8					

Note: N_{total} is the total number of plates in the column; N_{HE} is the heat supply plate number in the heat exchanger; Q_{reb} is the reboiler heat duty; R is the reflux ratio; Q_{HE} is the exchanger heat duty; Q_{cons} is the reduced energy consumption in the scheme with thermal integration.

of determining the optimal position of $N_{\rm HE}$ in the C2 column of Scheme II are presented in Table 4, and the optimal operating parameters for the diabatic Scheme II are shown in Table 5.

For Scheme III, it is necessary to determine the optimal positions of two heat supply

plates— $N_{\rm HE}^{-1}$ (from column C1) and $N_{\rm HE}^{-2}$ (from column C3)—into column C2, as well as the amount of heat supplied transferred from the steam flow of column C1 $(Q_{\rm HE}^{-1})$ and the steam flow of column C3 $(Q_{\rm HE}^{-2})$. The optimization results are shown in Table 6.

Table 4. Dependence of the parameters of column C2 for diabatic Scheme II on the position of the heat supply stage N_{HE}

$N_{ m HE}$	$Q_{ m HE}$, kW	$Q_{ m HE}$, kW $Q_{ m reb}^{ m C2}$, kW		
11	78.3	80.27	0.50	
12	78.3	77.95	0.48	
13	78.3	76.93	0.47	
14	78.3	76.29	0.46	

Note: $N_{\rm HE}$ is the heat supply plate number in the heat exchanger; $Q_{\rm HE}$ is the exchanger heat duty; C2 is the acetone separation column; $Q_{\rm reb}^{\rm C2}$ is the reboiler heat duty in C2; $R^{\rm C2}$ is the reflux ratio in C2.

Table 5. Optimal operation parameters for diabatic Scheme II

Parameters	C1	C2	C3			
$N_{ m total}$	45	18	44			
$N_{ m HE}$	_	14	_			
$Q_{ m reb}$, kW	92.3	76.3	107.1			
R	4.4	0.46	3.7			
Q_{HE} , kW	-	78.3	-			
$Q_{\rm cons}$, kW	275.7					

Note: N_{total} is the total number of plates in the column; N_{HE} is the heat supply plate number in the heat exchanger; Q_{reb} is the reboiler heat duty; R is the reflux ratio; Q_{HE} is the exchanger heat duty; Q_{cons} is the reduced energy consumption in the scheme with thermal integration.

It can be seen that the amount of heat released during the complete condensation of steam flows at the position $N_{\rm HE}{}^2=16$ or $N_{\rm HE}{}^2=17$ is excessive; when implementing such a scheme, additional heat supply to the reboiler of the C2 column is not required. At the same time, the lowest values of the reflux ratio in the C2 column are observed at $N_{\rm HE}{}^1=13$ and $N_{\rm HE}{}^2=17$. The optimal operating parameters of Scheme III are presented in Table 7.

In Scheme IV (Fig. 3d), the temperature of the upper steam flow of column C1 ($T_{cond} = 110.3$ °C)

of insufficient to provide heating distillation section of column C3. To achieve the necessary temperature difference, it is necessary to increase the flow pressure in the compressor. Thus, for this scheme it is necessary to determine both the optimal position of the plate $N_{\rm HE}$ and the optimal value of the compression ratio in the compressor $E_{\rm comp}$. It follows from Eq. (1) that the minimum value of the reduced energy costs (Q_{cons}) will be achieved with a minimum W_{comp} , and, accordingly, with a minimum E_{comp} , at difference necessary temperature

Table 6. Results of the search for optimal operating parameters of the diabatic Scheme III

$N_{ m HE}^{-1}$	$N_{ m HE}^{-2}$	$Q_{\rm HE}^{-1}$, kW	$Q_{\rm HE}^{2}$, kW	R^{C2}	$Q_{\rm reb}^{\rm C2}$, kW	
	11	78.3	107.2	0.92	27.91	
11	12	78.3	107.2	0.87	22.80	
	13	78.3	107.2	0.82	17.67	
	14	78.3	107.2	0.76	11.95	
	15	78.3	107.2	0.70	5.25	
	16	68.6	107.2	0.59	0.00	
	17	54.0	107.2	0.47	0.00	
	11	78.3	107.2	0.87	23.25	
	12	78.3	107.2	0.86	22.17	
	13	78.3	107.2	0.81	17.04	
12	14	78.3	107.2	0.76	11.29	
	15	78.3	107.2	0.69	4.49	
	16	66.0	107.2	0.57	0.00	
	17	52.6	107.2	0.46	0.00	
	11	78.3	107.2	0.83	18.55	
Ī	12	78.3	107.2	0.82	17.45	
Ī	13	78.3	107.2	0.81	16.47	
13	14	78.3	107.2	0.75	10.70	
	15	78.3	107.2	0.68	3.80	
	16	64.7	107.2	0.56	0.00	
	17	51.9	107.2	0.45	0.00	
	11	78.3	107.2	0.78	13.32	
	12	78.3	107.2	0.76	12.15	
	13	78.3	107.2	0.75	11.11	
14	14	78.3	107.2	0.74	10.15	
	15	78.3	107.2	0.68	3.13	
	16	63.2	107.2	0.54	0.00	
	17	51.3	107.2	0.49	0.00	

Note: $N_{\rm HE}^{-1}$ is the heat supply plate number in the heat exchanger to column C2 from column C1; $N_{\rm HE}^{-2}$ is the heat supply plate number in the heat exchanger to column C2 from column C3; $Q_{\rm HE}^{-1}$ is the exchanger heat duty from the steam flow of column C1; $Q_{\rm HE}^{-2}$ is the exchanger heat duty from the steam flow of column C3; C2 is the acetone separation column; $Q_{\rm reb}^{-C2}$ is the reboiler heat duty in C2; $R^{\rm C2}$ is the reflux ratio in C2.

Table 7. Optimal operation parameters for diabatic Scheme III

Parameters	C1	C2	С3	
$N_{ m total}$	45	18	44	
$N_{ m HE}^{-1}$	_	13	-	
$N_{ m HE}^{-2}$	_	17	_	
$Q_{ m reb}$, kW	92.3	0	107.1	
R	4.4	0.45	3.7	
$Q_{\rm HE}^{-1}$, kW	_	51.9	_	
$Q_{\rm HE}^{-2}$, kW	_	107.2	-	
$Q_{\rm cons}$, kW		199.4		

Note: N_{total} is the total number of plates in the column; N_{HE}^{-1} is the heat supply plate number in the heat exchanger to column C2 from column C3; Q_{reb} is the reboiler heat duty; R is the reflux ratio; Q_{HE}^{-1} is the exchanger heat duty from the steam flow of column C1; Q_{HE}^{-2} is the exchanger heat duty from the steam flow of column C3; Q_{PH}^{-1} is the heat duty in the preheater; E_{comp} is the compressor compression ratio; W_{comp} is the compressor power consumption; Q_{cons} is the reduced energy consumption in the scheme with heat integration.

Table 8. Results of the search for optimal operating parameters of the diabatic Scheme IV

$E_{ m comp}$	W _{comp} , kW	$N_{_{ m HE}}$	$Q_{_{ m HE}}$, kW	$Q_{\rm reb}^{ C3}$, kW	$Q_{_{\mathrm{PH}}}$, kW	Q _{cons} , kW
2.4	9.0	10	71.4	99.7	4.5	131.2
2.5	9.5	12	71.3	96.2	4.5	129.2
2.6	9.9	14	71.0	92.9	4.5	127.1
2.7	10.3	15	70.9	91.3	4.9	127.1
2.8	10.8	43	70.9	36.8	5.2	74.4

Note: E_{comp} is the compressor compression ratio; W_{comp} is the compressor power consumption; N_{HE} is the heat supply plate number in the heat exchanger; Q_{HE} is the exchanger heat duty; C3 is the extractive distillation column; $Q_{\text{reb}}^{\text{C3}}$ is the reboiler heat duty in C3; Q_{PH} is the heat duty in the preheater; Q_{cons} is the reduced energy consumption in the scheme with thermal integration.

between the heat source and receiver is provided. At the same time, the minimum value of $E_{\rm comp}$ depends on the position of the heat supply plate. The results of optimization of Scheme IV are shown in Table 8.

It is interesting to note that, with an increase in Ecomp from 2.4 to 2.7, the range of plates in the exhaustive section, to which heat supply in the C3 column is possible, increases smoothly; with $E_{\rm comp}=2.8$, there is a sharp jump, and heat supply becomes possible to any plate of the stripping section of the column. This is probably due to the characteristics of the temperature profile along the height of the column C3 (Fig. 2c), in the stripping section of which there is a zone where the temperature along the height of the column practically does not change. The optimal operating parameters of Scheme IV are presented in Table 9.

The optimization of Scheme V was carried out in a similar way. The results are presented in Tables 10 and 11.

RESULTS AND DISCUSSION

Table 12 shows the values of the reduced energy consumption for the conventional two-column ED scheme and the diabatic ED schemes obtained on its basis. The decrease of the reduced energy consumption $\Delta Q_{\rm cons}$ was calculated by Eq. (2):

$$\Delta Q_{\text{cons}} = (Q_{\text{total}} - Q_{\text{cons}}) / Q_{\text{total}} \times 100\%, \tag{2}$$

where $Q_{
m total}$ is the total energy costs in the reboilers of the columns of the conventional ED scheme, and $Q_{
m cons}$ is the reduced energy costs of the diabatic distillation scheme.

Table 12 shows that the greatest reduction in energy consumption compared to the conventional scheme is provided by diabatic Schemes I, II, and III, in which there are no compressors.

Table 9. Optimal operation parameters for diabatic Scheme IV

Parameters Parameters	C1	C2	С3				
$N_{ m total}$	45	18	44				
$N_{ m HE}$							
$Q_{\rm reb}$, kW	92.3	153.1	36.8				
R	4.4	0.44	3.7				
Q_{HE} , kW	_	_	70.9				
Q_{PH} , kW	5.2	_	_				
$E_{ m comp}$	2.8	_	_				
W_{comp} , kW	10.8	_	-				
$Q_{\rm cons}$, kW	319.8						

Note: N_{total} is the total number of plates in the column; N_{HE} is the heat supply plate number in the heat exchanger; Q_{reb} is the reboiler heat duty; R is the reflux ratio; Q_{HE} is the exchanger heat duty; Q_{PH} is the heat duty in the preheater; E_{comp} is the compressor compressor ratio; W_{comp} is the compressor power consumption; Q_{cons} is the reduced energy consumption in the scheme with thermal integration.

Table 10. Results of the search for optimal operating parameters of the diabatic Scheme V

$oldsymbol{E}_{ ext{comp}}$	W _{comp} , kW	$N_{_{ m HE}}$	$Q_{\rm HE}$, kW	$Q_{ m reb}^{ m C1}$, kW	$Q_{_{\mathrm{PH}}}$, kW	$Q_{ m cons}$, kW
1.6	1.1	37	10.8	89.3	0.2	92.8
1.7	1.3	38	12.4	87.4	0.3	91.6
1.8	1.4	39	14.4	85.4	0.3	89.9
1.9	2.0	42	27.9	71.7	0.5	78.2
2.0	3.1	43	40.1	59.6	0.7	69.6
2.2	4.0	44	44.3	50.1	0.9	63.0

Note: E_{comp} is the compressor compression ratio; W_{comp} is the compressor power consumption; N_{HE} is the heat supply plate number in the heat exchanger; Q_{HE} is the exchanger heat duty; C1 is the extractive distillation column; $Q_{\text{reb}}^{\text{C1}}$ is the reboiler heat duty in C1; Q_{PH} is the heat duty in the preheater; Q_{cons} is the reduced energy consumption in the scheme with thermal integration.

Table 11. Optimal operation parameters for diabatic Scheme V

Parameters Parameters	C1	C2	С3	
$N_{ m total}$	45	18	44	
$N_{ m HE}$	44	-	_	
$Q_{\rm reb}$, kW	50.1	153.1	107.1	
R	4.4	0.44	3.7	
Q_{HE} , kW	44.3	_	_	
Q_{PH} , kW	_	_	0.9	
$E_{ m comp}$	_	_	2.2	
W _{comp} , kW	_	_	4.0	
$Q_{\rm cons}$, kW		323.2		

Note: N_{total} is the total number of plates in the column; N_{HE} is the heat supply plate number in the heat exchanger; Q_{reb} is the reboiler heat duty; R is the reflux ratio; Q_{HE} is the exchanger heat duty; Q_{PH} is the heat duty in the preheater; E_{comp} is the compressor compression ratio; W_{comp} is the compressor power consumption; Q_{cons} is the reduced energy consumption in the scheme with thermal integration.

Table 13	E	- 62 - :	- C	::	:			1:-4:1	11 _ 4:	1
Table 12.	Energy	efficiency	OΙ	various	variants	ΟI	extractive	aisti	Haulon	schemes

D	Scheme								
Parameters	Convent.	I	II	III	IV	V			
$Q_{ ext{total}}, ext{kW}$	352.6	245.8	275.7	199.4	282.2	304.5			
W _{comp} , kW	0	0	0	0	10.8	4.0			
$Q_{\rm cons}$, kW	352.6	245.8	275.7	199.4	319.8	323.2			
$\Delta Q_{ m cons}$, %	0	30.3	21.8	43.5	9.3	8.9			

Note: Q_{total} is total energy costs in reboilers of the columns in the conventional scheme; W_{comp} is the compressor power consumption; Q_{cons} is the reduced energy consumption in the heat integration scheme; ΔQ_{cons} is the decrease in the reduced energy consumption in the heat integration scheme.

At the same time, the energy efficiency of Scheme I is higher than Scheme II, since more heat is released during condensation of the steam flow of column C3 than during condensation of the steam flow of column C1; as a result, the energy consumption in the reboiler of column C2 in Scheme I is reduced by 3.3 times, while in Scheme II, consumption is reduced by only 2 times compared to the conventional scheme. The maximum decrease of the reduced energy consumption is achieved in Scheme III: in this scheme, additional heat supply to the reboiler of column C2 $(Q_{reb}^{C2} = 0)$ is not required, since steam flows coming out from above columns C1 and C3 adequately provide its heating, while compression of steam flows using a compressor to increase their temperature is also not required. The energy efficiency of Schemes IV and V is significantly lower than that of Schemes I-III, although the energy consumption in the reboiler of the column C3 of Scheme IV is reduced by 2.9 times, while in the reboiler of the column C1 of Scheme V, energy consumption is reduced by 1.8 times compared with the energy consumption of the corresponding columns of the conventional scheme. This is due both to the presence of compressors in Schemes IV and V, as well as to the fact that the share of column C1 and column C3 in the total energy consumption of the conventional Scheme 2 is 26.2 and 30.4%, respectively, and the share of column C2 is 43.4%; therefore, reducing energy consumption in the

reboilers of these columns makes a smaller contribution to reducing the energy consumption of the Scheme 2 than the reduction of energy consumption in the reboiler of the C2 column.

CONCLUSIONS

Thus, five variants of schemes with thermal integration of columns due to diabatic distillation were synthesized based on the conventional ED scheme of an acetone-toluene-n-butanol mixture with preliminary separation of azeotropeforming components. The optimal parameters of these schemes are determined by the criterion of reduced energy costs. The schemes of diabatic ED are shown to be characterized by 8.9-43.5% lower reduced energy consumption than the conventional two-column scheme. At the same time, the greatest reduction in energy consumption is achieved in the scheme of diabatic distillation, in which steam flows coming from above two other columns are used to heat the separation column of azeotrope-forming components: ED columns and DMF regeneration columns.

Acknowledgments

The study was supported by the Ministry of Science and Higher Education of the Russian Federation, the state assignment for RTU MIREA, No. 0706-2020-0020.

Authors' contributions

- **P.S. Klauzner** planning and conducting research, analyzing research materials, writing the manuscript;
- **D.G. Rudakov** conducting research, analyzing research materials;

E.A. Anokhina – management and scientific consulting;
 A.V. Timoshenko – formulation of the scientific concept, general management.

The authors declare no conflicts of interest.

REFERENCES

- 1. Wang C., Guang C., Cui Y., Wang C., Zhang Z. Compared novel thermally coupled extractive distillation sequences for separating multi-azeotropic mixture of acetonitrile/benzene/methanol. *Chem. Eng. Res. Des.* 2018;136:513–528. https://doi.org/10.1016/j.cherd.2018.06.017
- 2. Yang A., Sy Y, Chien I.L., Jin S., Yan C., Wei S., Shen W., *et al.* Investigation of an energy-saving double-thermally coupled extractive distillation for separating ternary system benzene/toluene/cyclohexane. *Energy*. 2019;186:115756. https://doi.org/10.1016/j.energy.2019.07.086
- 3. Anokhina E.A., Timoshenko A.V., Akishin A.Y., Remizova A.V. Benzene purification from thiophene using dimethylformamide as an entrainer in thermally coupled extractive distillation columns. *Chem. Eng. Res. Des.* 2019;146:391–403. https://doi.org/10.1016/j.cherd.2019.04.003
- 4. You X., Rodriguez-Donis I., Gerbaud V. Improved design and efficiency of the extractive distillation process for acetone–methanol with water. *Ind. Eng. Chem. Res.* 2015;54(1):491–501. https://doi.org/10.1021/ie503973a
- 5. You X., Gu J., Peng C., Rodriguez-Donis I., Liu H. Optimal design of extractive distillation for acetic acid dehydration with *N*-methyl acetamide. *Chem. Eng. Process.: Process Intensif.* 2017;120:301–316. https://doi.org/10.1016/j.cep.2017.07.025
- 6. You X., Rodriguez-Donis I., Gerbaud V. Reducing process cost and CO_2 emissions for extractive distillation by double-effect heat integration and mechanical heat pump. *Appl. Energy.* 2016;166:128–140. https://doi.org/10.1016/j.apenergy.2016.01.028
- 7. Klauzner P.S., Rudakov D.G., Anokhina E.A., Timoshenko A.V. Use of Partially Thermally Coupled Distillation Systems and Heat Pumps for Reducing the Energy Consumption in the Extractive Distillation of an Isobutanol–Isobutyl Acetate Mixture Using Dimethylformamide. *Theor. Found. Chem. Eng.* 2020;54(3):397–406. https://doi.org/10.1134/S0040579520030070

- [Original Russian Text: Klauzner P.S., Rudakov D.G., Anokhina E.A., Timoshenko A.V. Use of Partially Thermally Coupled Distillation Systems and Heat Pumps for Reducing the Energy Consumption in the Extractive Distillation of an Isobutanol–Isobutyl Acetate Mixture Using Dimethylformamide. *Teoreticheskie osnovy khimicheskoi tekhnologii*. 2020;54(3):276–285. https://doi.org/10.31857/S0040357120030070]
- 8. Xu Y., Li J., Ye Q., Li Y. Design and optimization for the separation of tetrahydrofuran/isopropanol/water using heat pump assisted heat-integrated extractive distillation. *Sep. Purif. Technol.* 2021;277:119498. https://doi.org/10.1016/j.seppur.2021.119498
- 9. Jana A.K. Performance analysis of a heat integrated column with heat pumping. *Sep. Purif. Technol.* 2019;209:18–25. https://doi.org/10.1016/j.seppur.2018.07.011
- 10. Nova-Rincón A., Ramos M.A., Gómez J.M. Simultaneous optimal design and operation of a diabatic extractive distillation column based on exergy analysis. *Int. J. Exergy.* 2015;17(3):287–312. https://doi.org/10.1504/ IJEX.2015.070500
- 11. Klauzner P.S., Rudakov D.G., Anokhina E.A., Timoshenko A.V. Energy efficiency of diabatic distillation schemes for an acetone–toluene–*n*-butanol mixture with an entrainer in the first column. *Tonk. Khim. Tekhnol.* = *Fine Chem. Technol.* 2023;18(1):7–20 (in Russ.). https://doi.org/10.32362/2410-6593-2023-18-1-7-20
- 12. Aurangzeb Md., Jana A.K. Vapor recompression with interreboiler in a ternary dividing wall column: Improving energy efficiency and savings, and economic performance. *Appl. Therm. Eng.* 2018;147:1009–1023. https://doi.org/10.1016/j.applthermaleng.2018.11.008

About the authors:

- **Pavel S. Klauzner,** Cand. Sci. (Eng.), Assistant, Department of Chemistry and Technology of Basic Organic Synthesis, M.V. Lomonosov Institute of Fine Chemical Technologies, MIREA Russian Technological University (86, Vernadskogo pr., Moscow, 119571, Russia). E-mail: klauzner@mirea.ru. ResearcherID AAJ-7842-2021, RSCI SPIN-code 6922-6509, https://orcid.org/0000-0001-5844-549X
- **Danila G. Rudakov**, Cand. Sci. (Eng.), Associate Professor, Department of Chemistry and Technology of Basic Organic Synthesis, M.V. Lomonosov Institute of Fine Chemical Technologies, MIREA Russian Technological University (86, Vernadskogo pr., Moscow, 119571, Russia). E-mail: rudakov@mirea.ru. Scopus Author ID 37018548000, ResearcherID M-5241-2014, RSCI SPIN-code 2366-9449, https://orcid.org/0000-0002-9892-7909

Elena A. Anokhina, Dr. Sci. (Eng.), Professor, Department of Chemistry and Technology of Basic Organic Synthesis, M.V. Lomonosov Institute of Fine Chemical Technologies, MIREA – Russian Technological University (86, Vernadskogo pr., Moscow, 119571, Russia). E-mail: anokhina.ea@mail.ru. Scopus Author ID 6701718055, ResearcherID E-5022-2016, RSCI SPIN-code 8161-7762

Andrey V. Timoshenko, Dr. Sci. (Eng.), Professor, Department of Chemistry and Technology of Basic Organic Synthesis, M.V. Lomonosov Institute of Fine Chemical Technologies, MIREA – Russian Technological University (86, Vernadskogo pr., Moscow, 119571, Russia). E-mail: timoshenko@mirea.ru. Scopus Author ID 56576076700, ResearcherID Y-8709-2018, RSCI SPIN-code 5687-7930, https://orcid.org/0000-0002-6511-7440

Об авторах:

Клаузнер Павел Сергеевич, к.т.н., ассистент кафедры химии и технологии основного органического синтеза Института тонких химических технологий им. М.В. Ломоносова ФГБОУ ВО «МИРЭА – Российский технологический университет» (119571, Россия, Москва, пр-т Вернадского, д. 86). E-mail: klauzner@mirea.ru. ResearcherID AAJ-7842-2021, SPIN-код РИНЦ 6922-6509, https://orcid.org/0000-0001-5844-549X

Рудаков Данила Григорьевич, к.т.н., доцент кафедры химии и технологии основного органического синтеза Института тонких химических технологий им. М.В. Ломоносова ФГБОУ ВО «МИРЭА – Российский технологический университет» (119571, Россия, Москва, пр-т Вернадского, д. 86). E-mail: rudakov@mirea.ru. Scopus Author ID 37018548000, ResearcherID M-5241-2014, SPIN-код РИНЦ 2366-9449, https://orcid.org/0000-0002-9892-7909

Анохина Елена Анатольевна, д.т.н., профессор кафедры химии и технологии основного органического синтеза Института тонких химических технологий им. М.В. Ломоносова ФГБОУ ВО «МИРЭА – Российский технологический университет» (119571, Россия, Москва, пр-т Вернадского, д. 86). E-mail: anokhina.ea@mail.ru. Scopus Author ID 6701718055, ResearcherID E-5022-2016, SPIN-код РИНЦ 8161-7762

Тимошенко Андрей Всеволодович, д.т.н., профессор кафедры химии и технологии основного органического синтеза Института тонких химических технологий им. М.В. Ломоносова ФГБОУ ВО «МИРЭА – Российский технологический университет» (119571, Россия, Москва, пр-т Вернадского, д. 86). E-mail: timoshenko@mirea.ru. Scopus Author ID 56576076700, ResearcherID Y-8709-2018, SPIN-код РИНЦ 5687-7930, https://orcid.org/0000-0002-6511-7440

The article was submitted: September 13, 2022; approved after reviewing: November 26, 2022; accepted for publication: March 23, 2023.

Translated from Russian into English by N. Isaeva Edited for English language and spelling by Thomas A. Beavitt

THEORETICAL BASES OF CHEMICAL TECHNOLOGY

ТЕОРЕТИЧЕСКИЕ ОСНОВЫ ХИМИЧЕСКОЙ ТЕХНОЛОГИИ

ISSN 2686-7575 (Online)

https://doi.org/10.32362/2410-6593-2023-18-2-98-108

UDC 544.144.22



RESEARCH ARTICLE

Quantum chemical research of the molecular structure of 3,4-dicyanofuroxan

Inna N. Kolesnikova¹, Nikolay V. Lobanov¹,2,3,, Valery N. Lobanov², Igor F. Shishkov¹

¹M.V. Lomonosov Moscow State University (Faculty of Chemistry), Moscow, 119991 Russia ²Joint Institute for High Temperatures, Russian Academy of Sciences, Moscow, 125412 Russia ³MIREA – Russian Technological University (M.V. Lomonosov Institute of Fine Chemical Technologies), Moscow, 119571 Russia

Abstract

Objectives. The study set out to determine the equilibrium parameters of the 3,4-dicyanofuroxan molecule by means of molecule geometry optimization by quantum chemistry methods, verify the adequacy of the methods used, and compare the obtained results with X-ray diffraction analysis (XRD) and gas electron diffraction (GED) data.

Methods. Quantum chemical calculations were carried out using B3LYP, MP2, and CCSD(T) methods with 6-31G(d,p), cc-pVTZ, and aug-cc-pVTZ basis sets.

Results. The equilibrium molecular structure of 3,4-dicyanofuroxan was refined by means of quantum chemical calculations using the Gaussian09 program. The geometrical parameters were compared with the structure of this compound in the solid phase and a number of related compounds in gas and solid phases. It was theoretically established that the planar equilibrium structure of the dicyanofuroxan molecule has C_s symmetry. The structure of the free dicyanofuroxan molecule was found to differ depending on the phase. The B3LYP and CCSD(T) methods describe the molecular structure of dicyanofuroxan more accurately than the MP2 method. A regularity was revealed, according to which an increase in the basis, as a rule, leads to a better agreement of the geometry, regardless of the functional.

[™]Corresponding author, e-mail: lnw94@yandex.ru

Conclusions. The calculations performed are in good agreement with the literature data and results of joint analysis by GED and XRD. The effect of cyano substituents on the ring geometry is observed in comparison with the literature data for the dicyanofuroxan molecule. For the molecule in question, it is better to use the B3LYP/aug-cc-pVTZ method. The values of geometric parameters obtained by this method are in better agreement with the structure in the gas phase. The discrepancies with the experimental XRD results may be due to interactions in the crystal structure. Differences in the geometric parameters obtained on the basis of different functionals and bases make this molecule interesting for experimental structural studies using GED or microwave spectroscopy, which will permit the identification of optimal methods and bases for obtaining the geometric parameters of furoxan class molecules.

Keywords: equilibrium structure, molecular structure, oxadiazoles, furoxans, quantum chemical studies

For citation: Kolesnikova I.N., Lobanov N.V., Lobanov V.N., Shishkov I.F. Quantum chemical research of the molecular structure of 3,4-dicyanofuroxan. *Tonk. Khim. Tekhnol. = Fine Chem. Technol.* 2023;18(2):98–108 (Russ., Eng.). https://doi.org/10.32362/2410-6593-2023-18-2-98-108

НАУЧНАЯ СТАТЬЯ

Исследование равновесной структуры молекулы 3,4-дицианофуроксана

И.Н. Колесникова¹, Н.В. Лобанов^{1,2,3,□}, В.Н. Лобанов², И.Ф. Шишков¹

Аннотация

Цели. Определение равновесных параметров молекулы 3,4-дицианофуроксана посредством оптимизации геометрии молекулы методами квантовой химии, проверка адекватности используемых методов, а также сопоставление полученных результатов с данными рентгенодифракционного анализа (РСА) и газовой электронографии (ГЭ) родственных соединений.

Методы. Квантовохимические расчеты методами B3LYP, MP2 и CCSD(T) с базисными наборами 6-31G(d,p), cc-pVTZ и aug-cc-pVTZ.

Результаты. Уточнена равновесная молекулярная структура 3,4-дицианофуроксана с помощью квантово-химических расчетов в программе Gaussian09. Проведено сравнение геометрических параметров со структурой данного соединения в твердой фазе и с рядом родственных соединений в газовой и твердой фазе. Теоретически установлено, что равновесная структура молекулы дицианофурокса-

 $^{^{1}}$ Московский государственный университет им. М.В. Ломоносова (химический факультет), Москва, 119991 Россия

²Объединенный институт высоких температур Российской академии наук, Москва, 125412 Россия

³МИРЭА – Российский технологический университет (Институт тонких химических технологий им. М.В. Ломоносова), Москва, 119571 Россия

[™]Автор для переписки, e-mail: lnw94@yandex.ru

на является плоской и имеет симметрию C_s . Установлено, что структура свободной молекулы дицианофуроксана в зависимости от фазы различается. Методы CCSD(T) и B3LYP точнее описывает молекулярную структуру дицианофуроксана по сравнению с методом MP2. Выявлена закономерность, согласно которой увеличение базиса, как правило, приводит к лучшему согласованию геометрии независимо от функционала.

Выводы. Проведенные расчеты хорошо согласуются с литературными данными, а также результатами совместного анализа методами ГЭ и РСА. Влияние цианозаместителей на геометрию кольца наблюдается в сравнении с литературными данными для молекулы дицианофуроксана. Для рассматриваемой молекулы лучше использовать метод ВЗLYP/аид-сс-рVTZ. Значения геометрических параметров, полученные этим методом, лучше согласуются со структурой в газовой фазе. Расхождения с экспериментальными результатами РСА могут быть обусловлены взаимодействиями в кристаллической структуре. Различия в геометрических параметрах, полученных на основе разных функционалов и базисов, делают эту молекулу интересной для проведения экспериментального структурного исследования методами ГЭ или микроволновой спектроскопии, что позволит в будущем найти оптимальные методы и базисы для получения геометрических параметров молекул класса фуроксанов.

Ключевые слова: равновесная структура, молекулярная структура, оксодиазолы, фуроксаны, квантово-химические исследования

Для цитирования: Колесникова И.Н., Лобанов Н.В., Лобанов В.Н., Шишков И.Ф. Исследование равновесной структурымолекулы 3,4-дицианофуроксана. *Тонкиехимические технологии*. 2023;18(2):98–108. https://doi.org/10.32362/2410-6593-2023-18-2-98-108

INTRODUCTION

The class of oxadiazoles, representing one of the most promising in the creation of energyintensive compounds, became the focus research attention in the first decades of the 21st century [1] due to the combination of unusual thermochemical characteristics: high enthalpy of formation and thermal stability. The presence of active oxygen in oxadiazole and N-oxide also increases the energy capacity of the molecule [2]. In addition, the chemical properties of oxadiazoles make it easy to introduce groups containing high-energy bonds that increase the total energy of the molecule.

The 3,4-dicyano-1,2,5-oxadiazole-2-oxide (3,4-dicyano-furoxan, DCFO) substance is used in the solution of many urgent problems. Representing an intermediate in the organic synthesis of high-energy materials [3], the substance is used in chemical ignition systems

(it spontaneously ignites upon contact with rocket fuel components [4]), as well as showing pharmacological and biological activity (vasodilator) [5]. In addition, DCFO derivatives have antimalarial properties [6] and potential for application as coagulants and enzymes.

DCFO was synthesized for the first time in 1925 [7]. Subsequently, several more options for DCFO obtaining were proposed in 1962, 1975, 2001, and 2019 [3–5, 8]. For a long time, the 1962 synthesis [8] was the most reliable. However, in 2019 a group of scientists from Maryland developed a reproducible, economical, safe, and highly efficient method for DCFO obtaining, obtaining a crystal of the substance for the first time and confirming the result using X-ray diffraction on a single crystal [5].

At that time, the structure of nitro-containing derivatives of furoxans in the gas phase, such as 3-methyl-4-nitro- and 4-methyl-3-nitrofuroxan,

had already been studied by gas electron diffraction (GED) and quantum chemical calculations [9]. A number of pyridines containing a cyano group were also studied using the same methods [10–12].

In 1996, the first attempt was made to optimize the geometry of the DCFO molecule by means of the Gaussian-92 software package using the Hartree–Fock (HF) method, involving exchange-correlation 3-parametric Becke–Lie–Yang–Parr (B3LYP) density functional and density functional based on the second-order Möller–Plesset perturbation theory (MP2) with basis sets 6-31G(d,p) (HF/6-31G(d,p), B3LYP/6-31G (d,p), and MP2/6-31G(d,p)) [13]. A year later, the obtained calculation data for this substance were compared with the results of ultraviolet and infrared spectroscopy [14].

In 2012, a study was conducted using the Gaussian 09 software package [15]. However, the authors limited themselves to the level of the B3LYP/cc-pVTZ theory. Calculations based on the same methods using different bases are also of interest.

The aim of the present work is to determine the equilibrium structure of the DCFO molecule by optimizing the molecule geometry using B3LYP and MP2 quantum chemistry methods with the 6-31G(d,p)¹, cc-pVTZ², and aug-cc-pVTZ³ bases in the Gaussian 09 program; to carry out a calculation at the theoretical level CCSD(T)⁴ with the basis 6-31G(d,p); to check the adequacy of the methods used; and to compare the results with the data of X-ray diffraction analysis (XRD) and GED for related compounds.

EXPERIMENTAL

Quantum chemical calculations were carried out with by means of the Gaussian 09 software package [16] using the density functional theory method with the B3LYP functional [17, 18] and MP2 perturbation theory [19] with correlationally consistent basis sets 6-31G(d,p) [20], cc-pVTZ [21], and aug-cc-pVTZ [22]. A calculation using the CCSD(T) method [23] was additionally carried out with basis sets 6-31G(d,p). To determine the equilibrium structure of DCFO, complete optimization of the geometry and calculation of the oscillation

frequencies were performed. The atom numbering for the DCFO molecule are shown in the figure.

The Cartesian coordinates of the DCFO optimized using the CCSD(T)/6-31G(d,p), B3LYP/6-31G(d,p), and MP2/cc-pVTZ functionals are presented in the appendix (Tables S1, S2, and S3).

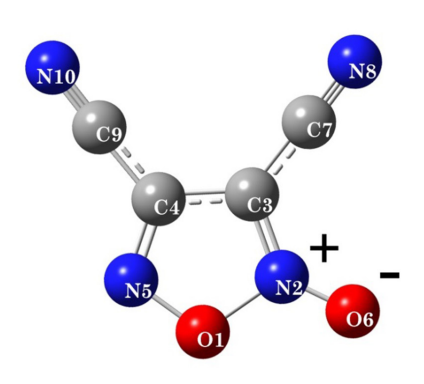


Fig. Atom numbering in the DCFO molecule.

RESULTS AND DISCUSSION

It follows from Table 1 that B3LYP/aug-cc-pVTZ calculations reproduce the C–N and C=O DCFO bond lengths better than MP2 calculations with the same basis set (especially when compared with the latest experimental data for the crystal [4]). This statement is also true for some bond angles. Quantum chemistry calculations show that the planar DCFO molecule has $\rm C_s$ symmetry. XRD revealed that there are 2 forms in the solid phase, the parameters of which differ in the case of bond lengths.

The equilibrium structure calculated by the B3LYP/aug-cc-pVTZ method is in good agreement with the solid phase determined by XRD. The discrepancies between the data are no more than 0.01 Å for the bond lengths, while the values of the bond angles differ by no more than 1°. In contrast to the gas phase, two molecules of the crystalline phase are nonplanar; however, the deviation from the plane does not exceed 4° (Table 1). A comparison of the equilibrium structure of DCFO with the structure in the crystalline phase demonstrates the similarity of the bond lengths of the oxadiazole rings with a maximum deviation not exceeding 0.02 Å and 2° in the bond lengths and bond angles, respectively. This indicates that the B3LYP method is likely to better predict the structure of DCFO in the gas phase. However, due to the different state of aggregation of these structures, their differences can be associated with the effects of intermolecular interactions in the crystal.

¹ 6-31G(d,p) is a valence-split basis set with addition of d-type polarization functions for each atom from Li to Ca and p-type polarization functions for each light atom (H, He).

 ² cc-pVTZ is a triple-zeta correlation consistent basis set.
 ³ aug-cc-pVTZ is an augmented version of the previous basis set with added diffuse features.

⁴ CCSD(T) is a coupled cluster single-double and perturbative triple method.

Table 1. Molecular parameters of DCFO

J		B3LYP			MP2		CCSD(T)	XR	XRD[4]
Parameter	/6-31G(d,p)	ZLAd-22/	/aug-cc-pVTZ	/6-31G(d,p)	ZLAd-22/	/aug-cc-pVTZ	/6-31G(d,p)	-	14
r _e (O1–N2)	1.475	1.472	1.470	1.651	1.552	1.567	1.479	1.458(2)	1.453(3)
r _e (N2–C3)	1.345	1.340	1.339	1.357	1.354	1.353	1.346	1.336(3)	1.346(3)
r _e (C3–C4)	1.430	1.425	1.426	1.408	1.403	1.403	1.426	1.404(3)	1.396(3)
r _e (C4–N5)	1.314	1.306	1.306	1.345	1.337	1.338	1.320	1.301(3)	1.296(3)
r _c (O1–N5)	1.351	1.346	1.347	1.311	1.314	1.312	1.369	1.366(3)	1.356(3)
r _e (N2–O6)	1.205	1.195	1.196	1.201	1.194	1.194	1.215	1.204(2)	1.205(3)
r _e (C3–C7)	1.410	1.405	1.406	1.414	1.408	1.409	1.420	1.418(3)	1.427(3)
r _e (C4–C9)	1.425	1.420	1.421	1.422	1.417	1.417	1.434	1.430(3)	1.422(4)
r _e (C7–N8)	1.163	1.152	1.152	1.185	1.174	1.175	1.174	1.135(3)	1.133(3)
r _c (C9–N10)	1.161	1.150	1.150	1.185	1.174	1.174	1.173	1.136(3)	1.127(4)
A(O1-N2-C3)	105.2	105.2	105.2	100.2	102.1	101.8	105.5	105.4(2)	105.0(2)
A(N2-C3-C4)	106.9	106.9	106.9	110.5	109.0	109.4	107.0	107.2(2)	107.2(2)
A(C3-C4-N5)	111.5	111.4	111.4	112.5	111.6	111.6	112.1	112.2(2)	111.9(2)
A(O1-N5-C4)	107.3	107.6	107.6	109.2	108.2	108.4	106.8	106.7(2)	107.4(2)
A(N2-O1-N5)	109.1	108.9	108.9	107.6	109.0	108.8	108.7	108.5(2)	108.5(2)
A(O1-N2-O6)	119.1	119.0	119.0	120.8	119.9	120.0	119.0	118.4(2)	118.0(2)
A(C3-N2-06)	135.7	135.8	135.8	138.9	138.0	138.2	135.5	136.2(2)	137.0(2)
A(N2-C3-C7)	122.2	122.2	122.3	119.6	120.3	120.2	121.6	121.8(2)	121.6(2)
A(C4-C3-C7)	131.0	130.9	130.8	129.9	130.6	130.3	131.4	131.0(2)	131.0(2)
A(C3-C4-C9)	126.5	126.7	126.7	126.1	126.6	126.5	126.5	126.3(2)	127.4(2)
A(C3-C7-N8)	179.1	179.0	179.0	179.8	179.7	179.7	179.1	178.8	178.9
A(C4-C9-N10)	178.6	178.3	178.2	178.5	178.4	178.1	178.4	177.9	178.0

120.7(2) 175.9 -0.40.3 9.0 14 121.4(2) 177.5 -0.60.3 0.8(6-31G(d,p))CCSD(T) 121.4 180.0 0.0 0.0 /aug-cc-pVTZ 121.8 180.0 0.0 0.0 0.0 0.0 /cc-pVTZ 121.8 180.0 0.0 0.0 0.0 6-31G(d,p)121.3 0.081 0.0 0.0 0.0 0.0 /aug-cc-pVTZ 121.9 180.0 0.0 0.0 0.0 0.0 /cc-pVTZ **B3LYP** 121.9 180.0 0.0 6-31G(d,p)180.0 0.0 0.0 0.0 0.0 121 D(01-N2-C3-C7) D(C7-C3-C4-C9) D(N2-01-N5-C4) D(01-N2-C3-C4) D(C3-C4-N5-01) Parameter A(N5-C4-C9)

Table 1. Continued

value of the angle between the corresponding atoms. D(O1–N2–C3–C4) is the value of the dihedral angle between the corresponding atoms. Bond lengths are given in angstroms. The Note: The DCFO crystal cell consists of two independent molecules 1 and 1A. r.(O1–N2) is the equilibrium bond length between the corresponding atoms. A(O1–N2–C3) is the angles are given in degrees.

The molecular structure of DCFO is relatively described by the B3LYP/aug-cc-pVTZ method: the functional gives the best fit for most bond lengths as compared to the MP2/cc-pVTZ method. The largest differences are observed for the O1-N2 bond: its length of 1.458(4) Å refined according to XRD data correlates with the length determined by the B3LYP/aug-cc-pVTZ method (1.470 Å) and does not coincide when using the MP2/cc-pVTZ method (1.552 Å).The same situation is observed with the O1-N5 bond length: according to XRD, its value is 1.366(5)Å, which is close to the value determined by B3LYP/aug-cc-pVTZ (1.347 Å); moreover, it noticeably differs from the results of MP2/cc-pVTZ (1.314 Å). The worst matches are given by MP2/6-31G(d,p): in this case, the difference for bond lengths reaches 0.1 Å.

The CCSD(T)/6-31G(d,p) method adequately describes the molecule structure, with most of the bond lengths correlating with the experimental data: the calculated O1-N2 bond length is 1.480 Å, while the bond length refined by XRD Å. The O1-N5 1.458(4)bond length calculated by the CCSD(T)/6-31G(d,p) method and obtained by XRD coincides with high precision (1.369 and 1.366(5) Å, respectively).

In this work, we also compared the structural parameters of DCFO with the geometry of related compounds (3-methyl-4-nitrofuroxan and 4-methyl-3-nitrofuroxan) determined by the GED method in [12].

From Table 2, it can be seen that DCFO is similar in parameters to 3-methyl-4-nitrofuroxan: for most bond lengths, the difference is no more than 0.08 Å, while the angles differ by no more than 2°-3°. The most noticeable deviations are in the C3-C7 (0.082 Å), N2-O6 (0.019 Å), and C3-C4 (0.012 Å) bonds. Among the angles, N2-C3-C4 (2.3°) and C3-C4-N5 (2.5°) show the largest discrepancy. The situation changes with the transition to 4-methyl-3-nitrofuroxan. The angles not coincide, while do the lengths of only two bonds (C3-C4 and N2-O6) are close in their values (the difference is less than 0.009 Å). Such significant differences (0.03-0.10 Å) may be due to the effect of substituents.

In general, it can be argued that comparing the results of calculations and MP2 methods with basis B3LYP the 6-31G(d,p),cc-pVTZ, and aug-cc-pVTZ, a tendency for a better agreement there calculated molecular between the parameters experimental values. It can seen that an increase in the basis, as a rule, leads to better geometry matching, regardless of the chosen functional (Table 3).

Quantum chemical research of the molecular structure of 3,4-dicyanofuroxan

Table 2. Comparison of structural parameters of DCFO, 3-methyl-4-nitrofuroxan, and 4-methyl-3-nitrofuroxan

Parameter	DCFO B3LYP/aug-cc-pVTZ	3-methyl-4-nitrofuroxan GED [12]	4-methyl-3-nitrofuroxan GED [12]
r _e (O1–N2)	1.470	1.462(9)	1.382(6)
r _e (N2–C3)	1.339	1.333(9)	1.307(6)
r _e (C3–C4)	1.426	1.414(9)	1.422(6)
r _e (C4–N5)	1.306	1.304(9)	1.340(6)
r _e (O1–N5)	1.347	1.354(9)	1.429(6)
r _e (N2–O6)	1.196	1.215(9)	1.205(6)
r _e (C3–C7)	1.406	1.488(9)	1.488(6)
A(O1–N2–C3)	105.2	107.2(5)	107.5(3)
A(N2–C3–C4)	106.9	104.6(5)	109.2(3)
A(C3–C4–N5)	111.4	113.9(5)	109.2(3)
A(O1–N5–C4)	107.6	106.1(10)	104.7(4)
A(N2-O1-N5)	108.9	108.1(10)	109.4(5)
A(O1-N2-O6)	119.0	118.1(6)	118.6(3)
A(N2-C3-C7)	122.3	121.2(5)	121.1(3)

Note: bond lengths are given in Å; angles are in degrees.

We also compared the C-N bond lengths in DCFO with a number of cyanopyridines, the data for which were obtained by two independent methods (Table 4).

The C-N bond length of DCPO is very similar to that in the corresponding cyanopyridines. The spread of values does not exceed 1%, which can be considered a good indicator, demonstrating

Table 3. Comparison of DCFO selected parameters during various quantum chemical calculations

Method	r _e (O1–N2), Å	r _e (O1–N5), Å
XRD [4]	1.458(2)	1.366(3)
B3LYP/6-31G(d,p)	1.475	1.351
B3LYP/cc-pVTZ	1.472	1.346
B3LYP/aug-cc-pVTZ	1.470	1.347
MP2/6-31G(d,p)	1.651	1.311
MP2/cc-pVTZ	1.552	1.314
MP2/aug-cc-pVTZ	1.567	1.312
CCSD(T)/6-31G(d,p)	1.480	1.369

Table 4. Comparison of bond lengths C-N in DCFO - 2-cyanopiridine - 3-cyanopiridine - 4-cyanopiridine series

DCEO (P31 V	Plang og pVT7)	2-cyanopiri	dine [10]	3-cyanopii	idine [11]	4-cyanopiridine [12]	
DCFO (B3L1)	P/aug-cc-pVTZ)	GED	XRD	GED	XRD	GED	XRD
r _e (C7–N8), Å	1.152	1.158(5)	1.1452(8)	1.157(2)	1.1499(12)	1.159(3)	1.1370(8)
r _e (C9–N10), Å	1.150						
r _e (C4–C9), Å	1.421	1 445(2)	1.440(0)	1 422(2)	1 4202(12)	1 420(2)	1 420(0)
r _e (C3–C7), Å	1.406	1.445(3)	1.448(2)	1.432(2)	1.4303(12)	1.438(3)	1.439(8)

that the chosen method and basis describe the molecule under consideration quite well.

CONCLUSIONS

The equilibrium structure of the DCFO molecule was refined by optimizing the free geometry using quantum chemistry methods. The adequacy of the methods used was checked by comparing the obtained results with those mentioned in the literature. The obtained results are compared with the XRD data for the molecule in the crystalline phase.

Equilibrium geometric structural parameters characterizing the DCFO molecule were obtained

(calculation results are given in Tables 1 and 2). The results are consistent with those of related compounds.

It should be noted that, although structural comparison of solid DCFO with modeling of the molecule properties in the gas phase between the centers of maximum electron density is somewhat difficult, the structures under study are quite similar. The data obtained by XRD correlate with the corresponding geometric parameters of the DCFO backbone calculated by the B3LYP/aug-cc-pVTZ method (r_c(O1–N2) bond length is 1.458(2) and 1.470 Å; r_c(O1–N5) bond length is 1.366(3) and 1.347 Å; r_c(N2–C3) bond length is 1.336(3) and 1.339 Å).

SUPPLEMENTARY

Table S1. Cartesian coordinates of atoms in the DCFO molecule obtained at the level of the CCSD(T)-31G(d,p) theory

No.	Symbol	X	Y	Z
1	О	1.0630	-1.6922	0.0
2	N	1.4296	-0.2798	0.0
3	С	0.2732	0.3759	0.0
4	С	-0.7800	-0.5742	0.0
5	N	-0.2976	-1.7930	0.0
6	О	2.5878	0.0245	0.0
7	С	0.2018	1.7728	0.0
8	N	0.1196	2.9355	0.0
9	С	-2.1677	-0.3032	0.0
10	N	-3.3028	-0.0472	0.0

Table S2. Cartesian coordinates of atoms in the DCFO molecule obtained at the level of the B3LYP/6-31G(d,p) theory

No.	Symbol	X	Y	Z
1	О	-1.81695	-0.83540	0.0
2	N	-1.34222	0.56103	0.0
3	С	0.0	0.47737	0.0
4	С	0.32868	-0.91407	0.0
5	N	-0.74964	-1.66405	0.0
6	О	-2.15078	1.45395	0.0
7	С	0.82413	1.62158	0.0
8	N	1.51834	2.55455	0.0
9	С	1.63809	-1.47669	0.0
10	N	2.71587	-1.90832	0.0

Table S3. Cartesian coordinates of atoms in the DCFO molecule obtained at the level of the MP2/cc-pVTZ theory

No.	Symbol	X	Y	Z
1	0	-1.81233	-0.89477	0.0
2	N	-1.34771	0.58627	0.0
3	С	0.0	0.46095	0.0
4	С	0.33496	-0.90095	0.0
5	N	-0.75514	-1.67493	0.0
6	О	-2.15711	1.46346	0.0
7	С	0.81982	1.60597	0.0
8	N	1.50816	2.55741	0.0
9	С	1.64067	-1.45056	0.0
10	N	2.73510	-1.87474	0.0

Authors' contributions

- **I.N. Kolesnikova** general management, setting research tasks, performing quantum-chemical calculations, and writing the text of the article;
- **N.V. Lobanov** analysis of literature sources, writing the text of the article, performing quantum chemical calculations, preparing bibliography and illustrative materials;
- **V.N. Lobanov** conceptualization of materials, consultations during the research, and editing of the article;
- *I.F. Shishkov* general guidance, setting research tasks, and editing the article.

The authors declare the absence of obvious and potential conflicts of interest related to the publication of this article.

REFERENCES

- 1. Mel'nikova S.F., Tselinskii I.V. 1,2,5-Oxadiazoles as energetic compounds. *Izvestiya Sankt-Peterburgskogo gosudarstvennogo tekhnologicheskogo instituta (tekhnicheskogo universiteta) = Bulletin of the Saint Petersburg State I nstitute of Technology (Technical University)*. 2013;2 (47):25–29 (in Russ.). URL: https://cyberleninka.ru/article/n/proizvodnye-1-2-5-oksadiazola-kak-energonasyschennye-soedineniya (accessed December 09, 2022).
- 2. Sharnin G.P., Falyakhov I.F., Yusupova L.M., Larionova O.A. *Khimiya energoemkikh soedinenii*. Kn. 2. *N-, O-nitrosoedineniya, furoksany, furazany, azidy, diazosoedineniya: uchebnoe posobie (Chemistry of Energy-Intensive Substances*. V. 2. *N-, O-Nitrocompounds, Furoxanes, Furazanes, Azides, Diazocompounds*). Kazan: KNITU; 2011. 376 p. (in Russ.). ISBN 978-5-7882-1200-5
- 3. Grundmann C., Nickel G.W., Bansal R.K. Nitriloxide, XVIII¹⁾ Das Tetramere der Knallsäure (Isocyanilsäure) und seine Derivate. (*Justus Liebigs Annalen der Chemie*) *Eur. J. Org. Chem.* 1975;19(6):1029–1050. https://doi.org/10.1002/jlac.197519750602
- 4. Johnson E.C., Bukowski E.J., Sausa R.C., Sabatini J.J. Safer and Convenient Synthesis of 3,4-Dicyanofuroxan. *Org. Process Res. Dev.* 2019;23(6):1275–1279. https://doi.org/10.1021/acs.oprd.9b00186
- 5. Mel'nikova T.M., Novikova T.S., Khmel'nitskii L.I., Sheremetev A.B. Novel synthesis of 3,4-dicyanofuroxan. *Mendeleev Commun*. 2001;11(1):30–31. https://doi.org/10.1070/MC2001v011n01ABEH001369
- 6. Mott B.T., Cheng K.C.-C., Guha R., *et al.* A furoxan–amodiaquine hybrid as a potential therapeutic for three parasitic Diseases. *Med. Chem. Commun.* 2012;3(12):1505–1511. https://doi.org/10.1039/C2MD20238G
- 7. Wieland H. Die Polymerisation der Knallsäure. Isocyanilsäure und Erythro-cyanilsäure. VII. Mitteilung über die Knallsäure. (*Justus Liebigs Annalen der Chemie*) Eur. J. Org. Chem. 1925;444(1):7–40. https://doi.org/10.1002/jlac.19254440103
- 8. Parker C.O., Emmons W.D., Rolewicz H.A., McCallum K.S. Chemistry of dinitroacetonitrile: Preparation and properties of dinitroacetonitrile and its salts. *Tetrahedron*. 1962;17(1–2):79–87. https://doi.org/10.1016/S0040-4020(01)99006-4
- 9. Belyakov A.V., Oskorbin A.A., Losev, V.A., Rykov A.N., Shishkov I.F., Fershtat L.L., Larin A.A., Kuznetsov V.V., Makhova N.N. The equilibrium molecular structure of 3-methyl-4-nitro- and 4-methyl-3-nitrofuroxans by gas-phase electron diffraction and coupled cluster calculations. *J. Molec. Str.* 2020;1222:128856. https://doi.org/10.1016/j.molstruc.2020.128856
- 10. Vogt N., Khaikin L.S., Rykov A.N., *et al.* The equilibrium molecular structure of 2-cyanopyridine from combined analysis of gas-phase electron diffraction and microwave data and results of *ab initio* calculations. *Struct. Chem.* 2019;30;1699–1706. https://doi.org/10.1007/s11224-019-01393-y
- 11. Khaikin L.S., Vogt N., Rykov A.N., Grikina O.E., Vogt J., Kochikov I.V., Ageeva E.S., Shishkov I.F. The equilibrium molecular structure of 3-cyanopyridine according to gas-phase electron diffraction and microwave data and the results of quantum-chemical calculations. *Mendeleev Commun.* 2018;28(3):236–238. https://doi.org/10.1016/j.mencom.2018.05.002
- 12. Khaikin L.S., Vogt N., Rykov A.N., *et al.* The equilibrium molecular structure of 4-cyanopyridine according to a combined analysis of gas-phase electron diffraction and microwave data and coupled-cluster computations. *Russ. J. Phys. Chem.* 2018;92(10):1970–1974. https://doi.org/10.1134/S0036024418100102

- 13. Pasinszki T., Ferguson G., Westwood N.P.C. Geometric and electronic structure of dicyanofuroxan by experiment and theory. *J. Chem. Soc. Perkin Trans.* 2. 1996;(2):179–185. https://doi.org/10.1039/P29960000179
- 14. Pasinszki T., Westwood N.P.C. Substituted oximes and furoxans as precursors to unstable nitrile oxides. Electronic and geometric structures by ultraviolet photoelectron spectroscopy, infrared spectroscopy and *ab initio* calculations. *J. Mol. Struc.* 1997;408–409:161–169. https://doi.org/10.1016/s0022-2860(96)09631-7
- 15. Vass G., Dzsotján D., Lajgut G.G., Pasinszki T. Photoelectron spectroscopic investigation of the electronic structure of furoxans. *Eur. Chem. Bull.* 2012;1(1–2):22–26. URL: https://www.epa.oszk.hu/02200/02286/00001/pdf/EPA02286_European_Chemical_Bulletin_2012_01-02_Vass_Dzsotjan_Lajgut_etal.pdf
- 16. Frisch M.J., Trucks G.W., Schlegel H.B., Scuseria G.E., Robb M.A., Cheeseman J.R., Scalmani G., Barone V., Petersson G.A., Nakatsuji H., Li X., Caricato M., Marenich A., Bloino J., Janesko B.G., Gomperts R., Mennucci B., Hratchian H.P., Ortiz J.V., Izmaylov A.F., Sonnenberg J.L., Williams-Young D., Ding F., Lipparini F., Egidi F., Goings J., Peng B., Petrone A., Henderson T., Ranasinghe D., Zakrzewski V.G., Gao J., Rega N., Zheng G., Liang W., Hada M., Ehara M., Toyota K., Fukuda R., Hasegawa J., Ishida M., Nakajima T., Honda Y., Kitao O., Nakai H., Vreven T., Throssell K., Montgomery J.A., Peralta Jr. J.E., Ogliaro F., Bearpark M., Heyd J.J., Brothers E., Kudin K.N., Staroverov V.N., Keith T., Kobayashi R., Normand J., Raghavachari K., Rendell A., Burant J.C., Iyengar S.S., Tomasi J., Cossi M., Millam J.M., Klene M., Adamo C., Cammi R., Ochterski J.W., Martin R.L., Morokuma K., Farkas O., Foresman J.B., Fox D.J. Gaussian 09, Revision A.02. Gaussian, Inc., Wallingford CT. 2016. URL: https://gaussian.com/ g09citation/ (accessed December 09, 2022).
- 17. Becke D. Density-functional exchange-energy approximation with correct asymptotic behavior. *Phys. Rev. A.* 1988;38(6):3098–3100. https://doi.org/10.1103/PhysRevA.38.3098
- 18. Lee C., Yang W., Parr R.G. Development of the Colle-Salvetti correlation-energy formula into a functional of the electron density. *Phys. Rev. B.* 1988;37(2):785–789. https://doi.org/10.1103/PhysRevB.37.785
- 19. Møller C., Plesset M.S. Note on an Approximation Treatment for Many-Electron Systems. *Phys. Rev.* 1934;46(7):618–622. https://doi.org/10.1103/PhysRev.46.618
- 20. Petersson A., Bennett A., Tensfeldt T.G., Al-Laham M.A., Shirley W.A., Mantzaris J. A complete basis set model chemistry. I. The total energies of closed-shell atoms and hydrides of the first-row elements. *J. Chem. Phys.* 1988;89(4):2193–2218. https://doi.org/10.1063/1.455064
- 21. Dunning Jr. T.H. Gaussian Basis Sets for Use in Correlated Molecular Calculations. I. The Atoms Boron through Neon and Hydrogen. *J. Chem. Phys.* 1989;90(2):1007–1023. https://doi.org/10.1063/1.456153
- 22. Kendall R.A., Dunning T.H., Harrison R.J. Electron-Affinities of the first-row Atoms Revisited. Systematic Basis Sets and Wave Functions. *J. Chem. Phys.* 1992;96(9):6796–6806. https://doi.org/10.1063/1.462569
- 23. Barnes E.C., Petersson G.A., Montgomery J.A. Jr., Frisch M.J. Martin M.L.J. Unrestricted Coupled Cluster and Brueckner Doubles Variations of W1 Theory. *J. Chem. Theory Comput.* 2009;5(10):2687–2693. https://doi.org/10.1021/ct900260g

Quantum chemical research of the molecular structure of 3,4-dicyanofuroxan

About the authors:

Inna N. Kolesnikova, Cand. Sci. (Chem.), Senior Researcher, Senior Lecturer, Faculty of Chemistry, Lomonosov Moscow State University (1, Leninskie Gory, Moscow, 119992, Russia). E-mail: i_n_kolesnikova@mail.ru. Scopus Author ID 35727242600, ResearcherID L-8003-2016, https://orcid.org/0000-0003-3513-3770

Nikolay V. Lobanov, Postgraduate Student, Ya.K. Syrkin Department of Physical Chemistry, M.V. Lomonosov Institute of Fine Chemical Technologies, MIREA – Russian Technological University (86, Vernadskogo pr., Moscow, 119571, Russia); Junior Researcher, Thermophysical Databases Laboratory (V.P. Glushko Thermocenter), Joint Institute for High Temperatures, Russian Academy of Sciences (13, Izhorskaya ul., Moscow, 125412); Engineer, Gas Electron Diffraction Scientific Laboratory, Faculty of Chemistry, Lomonosov Moscow State University (1, Leninskie Gory, Moscow, 119992, Russia). E-mail: lnw94@yandex.ru. https://orcid.org/0000-0001-5172-746X

Valery N. Lobanov, Leading Engineer, Thermophysical Databases Laboratory (V.P. Glushko Thermocenter), Joint Institute for High Temperatures, Russian Academy of Sciences (13, Izhorskaya ul., Moscow, 125412). E-mail: lwnk@yandex.ru. https://orcid.org/0000-0002-9822-973X

Igor F. Shishkov, Dr. Sci. (Chem.), Leading Researcher, Head of the Gas Electron Diffraction Scientific Laboratory, Faculty of Chemistry, Lomonosov Moscow State University (1, Leninskie Gory, Moscow, 119992, Russia). E-mail: igormg@mail.ru. Scopus Author ID 6701850450, ResearcherID B-2528-2015, https://orcid.org/0000-0002-1132-1905

Об авторах:

Колесникова Инна Николаевна, к.х.н., старший научный сотрудник, старший преподаватель, Химический факультет, $\Phi \Gamma EOV$ BO «Московский государственный университет имени М.В. Ломоносова» (119991, Россия, Москва, Ленинские Горы, д. 1). E-mail: <u>i_n_kolesnikova@mail.ru</u>. Scopus Author ID 35727242600, ResearcherID L-8003-2016, https://orcid.org/0000-0003-3513-3770

Лобанов Николай Валерьевич, аспирант кафедры физической химии им. Я.К. Сыркина Института тонких химических технологий им. М.В. Ломоносова, ФГБОУ ВО «МИРЭА – Российский технологический университет» (119571, Россия, Москва, пр-т Вернадского, д. 86); младший научный сотрудник, лаборатория теплофизических баз данных (Термоцентр им. В.П. Глушко), ФГБУН Объединенный институт высоких температур Российской академии наук (125412, Россия, Москва, ул. Ижорская, д. 13); инженер, научно-исследовательская лаборатория электронографии, Химический факультет, ФГБОУ ВО «Московский государственный университет имени М.В. Ломоносова» (119991, Россия, Москва, Ленинские Горы, д. 1). Е-mail: lnw94@yandex.ru. https://orcid.org/0000-0001-5172-746X

Лобанов Валерий Николаевич, ведущий инженер, лаборатория теплофизических баз данных (Термоцентр им. В.П. Глушко), ФГБУН Объединенный институт высоких температур Российской академии наук (125412, Россия, Москва, ул. Ижорская, д. 13). E-mail: lwnk@yandex.ru. https://orcid.org/0000-0002-9822-973X

Шишков Игорь Фёдорович, д.х.н., ведущий научный сотрудник, заведующий научно-исследовательской лабораторией электронографии, Химический факультет, ФГБОУ ВО «Московский государственный университет имени М.В. Ломоносова» (119991, Россия, Москва, Ленинские Горы, д. 1). E-mail: igormg@mail.ru. Scopus Author ID 6701850450, ResearcherID B-2528-2015, https://orcid.org/0000-0002-1132-1905

The article was submitted: December 22, 2022; approved after reviewing: February 28, 2023; accepted for publication: March 23, 2023.

Translated from Russian into English by M. Povorin Edited for English language and spelling by Thomas A. Beavitt

SYNTHESIS AND PROCESSING OF POLYMERS AND POLYMERIC COMPOSITES

СИНТЕЗ И ПЕРЕРАБОТКА ПОЛИМЕРОВ И КОМПОЗИТОВ НА ИХ ОСНОВЕ

ISSN 2686-7575 (Online)

https://doi.org/10.32362/2410-6593-2023-18-2-109-122

UDC 678.021



RESEARCH ARTICLE

Projection of structure and compositions of resistance to burning polymer composite materials with flame retardants based on magnesium hydroxide

Kristina A. Brekhova[⊠], Igor D. Simonov-Emel'yanov, Alexander A. Pykhtin

MIREA – Russian Technological University (M.V. Lomonosov Institute of Fine Chemical Technologies), Moscow, 119571 Russia

[™]Corresponding author, e-mail: kr-otaku@mail.ru

Abstract

Objectives. To identify general principles for the design of dispersed-filled polymer composite materials (DFPCMs) with different generalized and reduced parameters, as well as types of disperse structure with high fire resistance; to develop an algorithm for the creation of non-combustible polymer composites with flame-retardant fillers.

Methods. Scanning electron microscopy and laser diffraction were used to assess the shape, size, and particle size distribution of flame retardants. According to the presented classification of DFPCMs by structural principle, standard bar samples were obtained to determine the oxygen index (OI) and the fire resistance category.

Results. For the MFS-2 (medium filled system) and HFS (high filled system) structure types, the maximum resistance to burning (category V-0) is achieved with a generalized parameter of $\Theta \le 0.40$ volume fractions; the OI value increases in 2 times (up to ~40%) in relation to the polymer matrix.

Conclusions. In order to obtain a flame retardant DFPCMs (OI = 40%, category V-0) based on ethylene vinyl acetate with OI = 20% and magnesium hydroxide (brucite), the amount of water vapor released during the decomposition of the flame-retardant filler should be at least \sim 250 mL/g with a coke residue \sim 32%. A developed algorithm for calculating compositions and generalized parameters for the creation of DFPCMs having a predetermined type of disperse structure and high resistance to burning is presented.

Keywords: composite materials, disperse structure, oxygen index, resistance to burning, cable composition, EVA, mineral flame retardants

For citation: Brekhova K.A., Simonov-Emel'yanov I.D., Pykhtin A.A. Projection of structure and compositions of resistance to burning polymer composite materials with flame retardants based on magnesium hydroxide. *Tonk. Khim. Tekhnol.* = *Fine Chem. Technol.* 2023;18(2):109–122 (Russ., Eng.). https://doi.org/10.32362/2410-6593-2023-18-2-109-122

НАУЧНАЯ СТАТЬЯ

Проектирование структуры и составов стойких к горению полимерных композиционных материалов с наполнителями-антипиренами на основе гидроксида магния

К.А. Брехова[∞], И.Д. Симонов-Емельянов, А.А. Пыхтин

МИРЭА – Российский технологический университет (Институт тонких химических технологий им. М. В. Ломоносова), Москва, 119571 Россия

В Автор для переписки, e-mail: kr-otaku@mail.ru

Аннотация

Цели. Установить фундаментальные закономерности для проектирования составов дисперсно-наполненных полимерных композиционных материалов (ДНПКМ) с разными обобщенными и приведенными параметрами и типами дисперсной структуры с высокой стойкостью к горению, а также разработать алгоритм создания негорючих полимерных композитов с наполнителями-антипиренами.

Методы. Оценку формы, размера и распределения частиц по размерам для наполнителей-антипиренов всех марок определяли на сканирующем электронном микроскопе и методом лазерной дифракции. Согласно представленной классификации ДНПКМ по структурному принципу были получены стандартные образцы брусков для определения кислородного индекса (КИ) и категории стойкости к горению.

Результаты. Установлено, что для структуры ДНПКМ типа СНС-2 (средне-наполненная система) и ВНС (высоконаполненная система) при обобщенном параметре $\Theta \leq 0.40$ об. д. достигается максимальная стойкость к горению (категория ПВ-0), а значение КИ возрастает в 2 раза (до ~40%) относительно полимерной матрицы.

Выводы. Показано, что для получения стойких к горению ДНПКМ (КИ = 40%, категория ПВ-0) на основе сэвилена с КИ = 20% и гидроксида магния (брусит),

количество выделяющихся паров воды долно составлять не менее ~250 мл/г при разложении наполнителя-антипирена, а коксовый остаток ~32%. Представлен алгоритм расчета составов, обобщенных параметров и создания ДНПКМ с заданным типом дисперсной структуры и высокой стойкостью к горению.

Ключевые слова: композиционные материалы, дисперсная структура, кислородный индекс, стойкость к горению, кабельная композиция, сэвилен, минеральные антипирены

Для цитирования: Брехова К.А., Симонов-Емельянов И.Д., Пыхтин А.А. Проектирование структуры и составов стойких к горению полимерных композиционных материалов с наполнителями-антипиренами на основе гидроксида магния. Тонкие химические технологии. 2023;18(2):109—122. https://doi.org/10.32362/2410-6593-2023-18-2-109-122

INTRODUCTION

One of the urgent tasks in practical materials science consists in the creation of non-combustible polymeric and polymer composite materials (PCM) offering increased resistance to burning and low toxicity of gaseous substances emitted during burning.

The widespread use of dispersed-filled PCM (DFPCM) in industry is partly due to the large number of studies on flame-retardant substances of different chemical composition forming the basis for determining specific conditions for obtaining fire-resistant materials with reduced fire hazard [1–5].

Halogen-containing substances, which decompose when heated to release a halogen atom that inhibits the burning process, are actively used as flame retardants. However, their use is limited by the toxicity of combustion products and wastes involved in the production of halogen-containing polymer compositions, which both comprise significant environment pollutants [6–11].

In terms of halogen-free flame-retardant fillers, mineral powder fillers based on aluminum (Al), magnesium (Mg), and calcium (Ca) hydroxides, which form water vapors during decomposition, have proven most effective. In this case, the endothermic reaction of the filler decomposition with the release of water contributes to cooling, the isolation of the burning zone from available oxygen, and

a reduction of gas exchange at the material surface, as well as reducing smoke formation [12]. In order to obtain burning resistant DFPCMs, the amount of mineral flame-retardant filler in them should be not less than ~45–60 wt % (22–30 vol % at density ~2.5 g/cm³) according to the published data [11–13].

The maximum content φ_{max} of a dispersed flame-retardant filler, which can practically be introduced into a PCM on a matrix of any nature, depends on the maximum packaging $(k_p, \varphi_{\text{max}})$, size (d), shape (k_e) , fractional composition, and particle distribution in the volume of the polymer matrix (PM).

The following are generalized values of the maximum content (ϕ_{max} , vol fract.) of solid dispersed fillers with various particle sizes in DFPCMs, which are in good agreement with experimental data [14]:

- nanoparticles (1–100 nm) $\phi_{max} \approx 0.05$ –0.20 vol fract.
- ultradisperse particles (0.1–1.0 $\mu m)$ $\phi_{max}\approx 0.20$ –0.255 vol fract.
- submicroparticles (1.0–3.0 $\mu m)$ $\phi_{max} \approx$ ≈ 0.255 –0.35 vol fract.
- microparticles (3–10 $\mu m)$ $\phi_{max} \approx 0.35$ –0.45 vol fract.
- macroparticles (10–40 $\mu m)$ $\phi_{max} \approx 0.45$ –0.62 vol fract.
- large particles (larger than 50 $\mu m)$ $\phi_{max} \approx \approx 0.62 \text{--} 0.64$ vol fract.

Analysis of the above data showed that only large and macroparticles of flame-retardant fillers with a size of more than ${\sim}10~\mu m$ or their mixtures with nanoparticles and microparticles can be used to create burning-resistant DFPCMs [14]. When nano-, ultradisperse-, and submicro-particles are used, highly efficient dispersants must be used, which help to increase ϕ_{max} to allow the introduction of flame retardant in the required quantity (up to ${\sim}50{-}60$ wt %).

Unfortunately, since data on the packaging and maximum content of dispersed flame-retardant fillers in DFPCM are virtually non-existent in the scientific and technical literature, it is not possible to determine the structural formation process in such systems.

New models, classifications, and calculations of DFPCM compositions, developed in recent years, generalized and reduced parameters of disperse structure relate dispersed structure types—diluted systems (DS), low-filled systems (LFS), medium-filled systems (MFS), medium-filled systems below the yield point (MFS-1), medium-filled systems above the yield point (MFS-2), and high-filled systems (HFS)—with a set of rheological, physical and mechanical, electrophysical, thermal, and optical characteristics [14]. However, there appear to be no data on burning resistance.

In [15], we considered the flammability of DFPCM flooring with silica inert filler with diameters of 500 μ m and 160 μ m in terms of the relationship of surface heat flux density (q) with generalized parameters, as well as providing a detailed disperse structure typology.

The aim of the present work is to establish fundamental regularities for the design of DFPCM compositions with different generalized and reduced

parameters, as well as various disperse structure types offering high resistance to burning. This can provide the basis for the development of an algorithm for creating non-combustible polymer composites with flame-retardant fillers.

EXPERIMENTAL

DFPCM for cable insulation based on copolymer ethylene vinyl acetate – EVA 11306-075, with melt flow rate 8 g/10 min (*Kazanorgsintez*, Russia) and mineral antipyrine fillers from brucite EcoPiren® (EP) based on magnesium hydroxide $Mg(OH)_2$ (*RGKHO*, Russia) were used as a material basis for the study.

The shape, size, and particle size distribution for all grades of flame-retardant fillers were determined using a Hosokawa-Alpine scanning electron microscope (Germany) and a Malvern Mastersizer 2000 laser analyzer (*Malvern Panalytical*, UK).

Table 1 shows the main characteristics of the dispersed flame-retardant fillers (brucite) of the various EP grades.

Figure 1 shows the structure of the dispersed powder of EP flame-retardant filler.

As can be seen from Fig. 1, magnesium hydroxide particles have a scaly structure with a shape coefficient $k_e \approx 5$ [14]. Due to their shape often differing from lamellar, it is not possible to determine the shape coefficient of flame-retardant particles with the necessary accuracy from a study of micrographs (Fig. 1). The investigated EP dispersed flame-retardant fillers are characterized by a fairly wide particle size distribution. When constructing the structure of DFPCMs, the shape, size, particle size distribution, and the maximum content of the flame-retardant filler

Table 1. Characteristics of flame retardants based on magnesium hydroxide (brucite) of various EcoPiren® (EP) grades and particle sizes

Flame-retardant filler	Particle size change interval, μm	Average particle diameter $d_{\rm av}$, $\mu{\rm m}$	Specific surface area S_s , m^2/g	
EP 2SA	0.6–5.0	2.5	3.50	
EP 3.5	1–10	5.0	2.63	
EP 5.5	1–9	10.0	2.06	
EP 10R	2–47	24.0	1.60	
EP 20R	2–89	45.0	1.23	

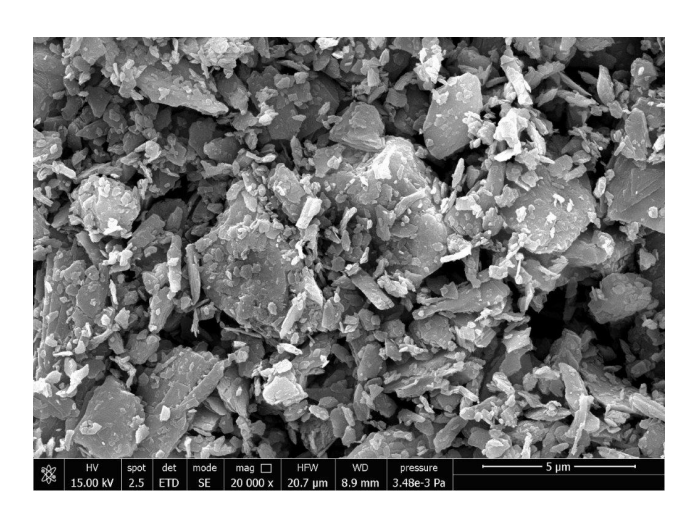


Fig. 1. Structure of the particles of the EP 3.5 flame-retardant filler.

in the PM takes into account the parameter ϕ_{max} (vol fract.), which can be determined using special experimental techniques [16]. The ϕ_{max} values for all investigated flame-retardant fillers (brucite) are given in Table 2.

From the above data follows the incorrectness of determining the parameter ϕ_{max} by bulk density for investigated flame retardants.

The maximum content of the flame-retardant filler in DFPCM ($\phi_{max} \sim 0.62$ vol fract.) is achieved for macroparticles of EP-10R and EP-20R grades with a particle size of 25 and 45 μm , respectively. With a decrease in the particle size to 2.5 μm , ϕ_{max} decreases to 0.25 vol fract. (EP 2SA).

The design of a disperse structure having different types and various generalized parameters, as well as DFPCM compositions based on EVA and flame retardants of various EP grades, was carried out according to the algorithm developed earlier [14].

The content of a dispersed flame-retardant filler (ϕ_f) with a known parameter ϕ_{max} ensures the formation of a given type of structure in the DFPCM (classified according to the generalized parameter Θ), was calculated by Eq. (1) [14]:

$$\varphi_f = (1 - \Theta) \times \varphi_{max}$$
, vol fract. (1)

where Θ is the PM fraction for the formation of interlayers between filler particles in DFPCM.

Figure 2 shows the dependencies of $\varphi_f = f(\Theta)$ for the design of DFPCM compositions with a given type of disperse structure based on EVA and flame-retardant fillers of various EP grades.

The presented data on DFPCM compositions show that when using flame-retardant fillers with a particle size of 2.5–10 μm (EP 2SA grade with $\phi_{max} = 0.25$ vol fract., EP 3.5 with $\phi_{max} = 0.35$ vol fract., and EP 5.5 with $\phi_{max} = 0.43$ vol fract.), it is almost impossible to introduce a sufficient amount of dispersed filler (up to ~ 60 wt %) to obtain materials resistant to burning [14].

In [17], it is shown that the amount of water vapor released from the flame-retardant filler

Table 2. ϕ_{max} values for dispersed powders of flame-retardant fillers of various EP grades

	No. Flame-retardant filler	Particle diameter d _{av} , μm	φ _{max,} vol fract.					
No.			By oil capacity	By the sealing graph	By three concentrations	By bulk density		
1	EP 2SA	2.5	0.27	0.24	0.23	0.157		
2	EP 3.5	5.0	0.36	0.34	0.35	0.168		
3	EP 5.5	10.0	0.47	0.43	0.42	0.195		
4	EP 10R	25.0	0.61	0.6	0.59	0.231		
5	EP 20R	45.0	0.63	0.62	0.61	0.291		

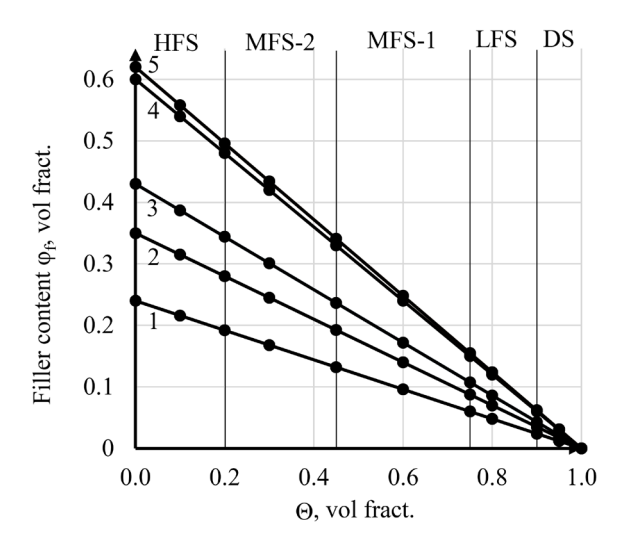


Fig. 2. Dependence of the flame-retardant filler content (ϕ_f) in DFPCM on the generalized parameter Θ for various EP grades:

$$\begin{array}{l} 1-EP\ 2SA\ (\phi_{max}=0.25);\ 2-EP\ 3.5\ (\phi_{max}=0.35);\\ 3-EP\ 5.5\ (\phi_{max}=0.43);\ 4-EP\ 10R\ (\phi_{max}=0.60);\\ 5-EP\ 20R\ (\phi_{max}=0.62). \end{array}$$

(brucite). Depending on the particle diameter, this reaches its maximum value ($V_{\rm H_2O} \sim 430~{\rm mL/g}$) with a particle diameter of more than 10 μm .

Considering the maximum packing (ϕ_{max}) and the amount of water vapor emitted during decomposition, the EP 10R flame-retardant filler $(d_{av}=25~\mu m$ and $\phi_{max}=0.60$ vol fract.) was used to investigate the effect of structure type and parameters and create the burning-resistant DFPCM.

To conduct experimental studies, the following compositions of DFPCM with an EP 10R flame-retardant filler ($d_{av}=25~\mu m,~\phi_{max}=0.60$ vol fract.) and different types of structures were used: DS with $\Theta=0.95$ vol fract., $\phi_f=0.03$ vol fract.; LFS with $\Theta=0.75$ vol fract., $\phi_f=0.15$ vol fract.; MFS-1 with $\Theta=0.60$ vol fract., $\phi_f=0.24$ vol fract. and with $\Theta=0.50$ vol fract., $\phi_f=0.30$ vol fract.; MFS-2 with $\Theta=0.45$ vol fract., $\phi_f=0.33$ vol fract. and with $\Theta=0.30$ vol fract., $\phi_f=0.42$ vol fract. HFS with $\Theta=0.20$ vol fract., $\phi_f=0.48$ vol fract.

DFPCMs based on EVA and EP 10R fillers with different disperse structure types were produced by mixing the raw components on a LabTech LZ80/VS twin-screw extruder (*Labtech Engineering*, Thailand) with a screw diameter of 16 mm at 200°C and a screw speed of 150 rpm.

In order to determine the oxygen index (OI)¹ and the category of resistance to burning (method B)², standard samples in bar form were obtained from DFPCMs with different types of disperse structure using injection molding.

Samples in the form of standard bars were cast on the ARBURG injection molding machine (Germany) at a pressure of 50 MPa, a melt temperature of 200°C, a mold temperature of 30°C, a holding time under pressure of 5 s, and a cooling time of 24 s.

The testing of DFPCMs with different types of disperse structure for resistance to burning and determination of OI was carried out in the Center of Scientific and Technical Department No. 3 of the G.S. Petrov Plastics Research and Testing Institute (Russia).

For determining the burning resistance of DFPCM, the burning and smoldering times of a vertically mounted bar specimen were recorded; based on the test results, the material was assigned a burning resistance category whose parameters are shown in Table 3.

DFPCMs of the V-0 category are characterized by the greatest resistance to burning. Samples that do not conform to the presented categories of resistance to burning are assigned a category—out of category (–), which corresponds to the lowest resistance to burning. For the initial PM EVA the flammability parameters were determined: OI = 20.5% and flammability category—(–).

RESULTS AND DISCUSSION

The results on burning resistance and OI parameters for all investigated samples of DFPCMs based on EVA 11306-075 grade with EP 10R flame-retardant filler are given in Table 4.

According to the results of the experiment, DFPCM with a magnesium hydroxide content of EP 10R not less than ~0.36 vol fract. (~0.59 wt fract.), which corresponds to the disperse structure types MFS-2 ($\Theta \le 0.40$ vol fract.) and HFS ($\Theta \le 0.20$ vol fract.), has the highest category of resistance to burning (V-0).

Polymer materials with the specified category of resistance to burning are approved for the manufacture of electrical products in the cable industry [18]. According to works of A.V. Filina [18] and A.A. Frik³, DFPCM used as electrical insulation materials should have an OI of at least ~32%.

¹ GOST 21793-76. Gosstandart of the USSR. Plastics. Method for determination of the oxygen index. Moscow: State committee for standards of the council of ministers of the USSR; 1976.

² GOST 28157-2018. Interstate standard. Plastics. Methods for determining the resistance to burning. Moscow: Standartinform: 2018.

³ Frik A.A. Research and development of fire-resistant cables using halogen-free materials: Cand. Sci. Thesis. Moscow: VNIIKP; 2016. 20 p. (in Russ.).

Table 3. Criteria for the category of resistance to burning DFPCM

Test in diagrams	Category of resistance to burning			
Test indicators	V-0	V-1	V-2	
Burning time after application of flame, no more than, s	10	30	30	
The total burning time of 5 samples after two-fold application of flame, s		250	250	
Does not burn and smolder before clamping	+	+	+	
Ignition of hygroscopic cotton wool located 300 mm from the sample	_	-	+	
Burning and smoldering of the sample after the second removal of the flame, no more than, s	30	60	60	

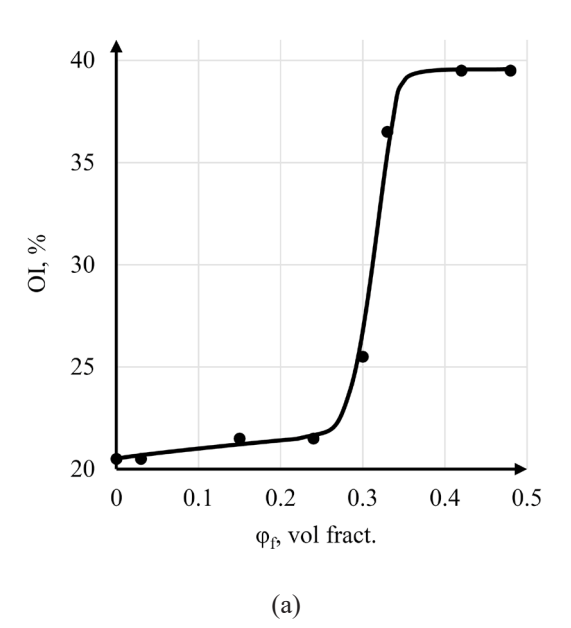
 $\it Note$: "+" – the indicator is achieved; "-" – the indicator is not achieved.

Table 4. Type of structure, generalized parameters, compositions of DFPCM based on EVA + EP 10R and their resistance to burning

DFPCM	Torrest of the state of	Θ, vol fract.	EP 10R (q	o _s) content	Category of resistance	
composition	Type of structure		vol fract.	wt fract.	to burning GOST 28157-2018	
EVA 11306-075	_	1.0	_		(-)	
EVA 11306-075 + EP 10R	DS	0.95	0.03 0.07		(-)	
	LFS	0.75	0.15 0.31		(-)	
	MFS-1	0.60	0.24	0.45	V-2	
		0.50	0.30	0.52	V-2	
		0.45	0.33	0.56	V-1	
	MFS-2	0.40	0.36	0.59	V-0	
		0.30	0.42	0.65	V-0	
	HFS	0.20	0.48	0.70	V-0	

Figure 3 shows the dependence of OI = $f(\phi_p)$ and, for the first time, the OI dependence for DFPCMs on the generalized parameter (Θ) of the disperse structure, forming a basis for relating the disperse structure types with the OI parameter and the burning resistance. Here it should be noted that the traditional OI dependence on ϕ f does not allow the classification of DFPCMs according to the structural principle (DS, LFS, MFS-1, MFS-2, and HFS).

The dependence OI = $f(\Theta)$ for DFPCMs has an S-shaped form and characteristic areas that correspond to different types of disperse structure.



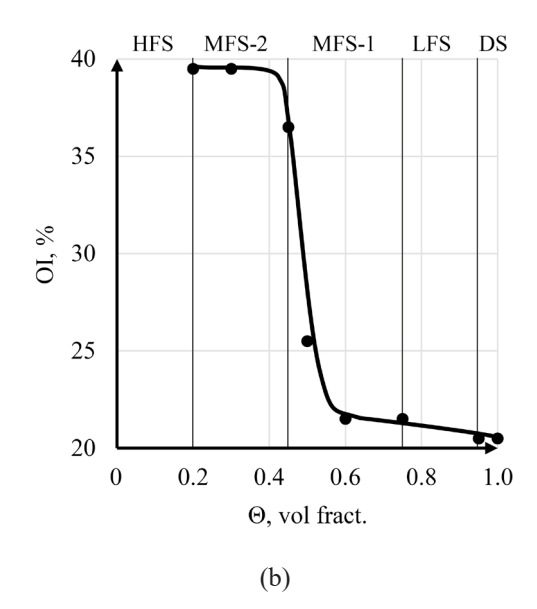


Fig. 3. OI dependence for DFPCM based on EVA:
(a) on the EP 10R flame-retardant filler content,
(b) on the generalized parameter Θ.

In area 1, the OI value increases by only $\sim 10\%$, amounting to $\sim 22\%$ when the EP 10R is introduced into the EVA. These are the DS, LFS, and MFS-1 structure types (up to $\Theta \geq 0.60$ vol fract.).

In area 2, there is a sharp jump in the OI value from 22 to 37% in the formation of DFPCM with the MFS-1 structure type at $\Theta \approx 0.60$ –0.45 vol fract.

In area 3, the OI reaches its maximum value of 40%, which is associated with the formation of MFS-2 (Θ < 0.40–0.30 vol fract.) and HFS (Θ < 0.20 vol fract.) structures in DFPCMs, along with a corresponding increase in the flame-retardant filler (brucite) content.

Thus, for DFPCMs based on EVA with OI = 20.5% and EP 10R flame retardant, it is possible to achieve the OI value in \sim 2 times higher than the OI value characteristic for an unfilled PM at the creation of disperse structures of MFS-2 and HFS types. In this case, the maximum value $\Theta \approx 0.40$ vol fract., EP 10R flame-retardant filler content \approx 0.36 vol fract. (0.59 wt fract.), an OI of \approx 40%, and a category of resistance to burning—V-0.

At OI $\approx 32\%$ (the recommendation given in works of Filina [18] and Frik (Footnote 3)), the cable insulation from DFPCM based on EVA + EP 10R can have a structure like MFS-1 with $\Theta\approx 0.50$ vol fract.; the filler content will decrease and amount to $\phi_{\rm f}\approx 0.30$ vol fract. (0.52 wt fract.).

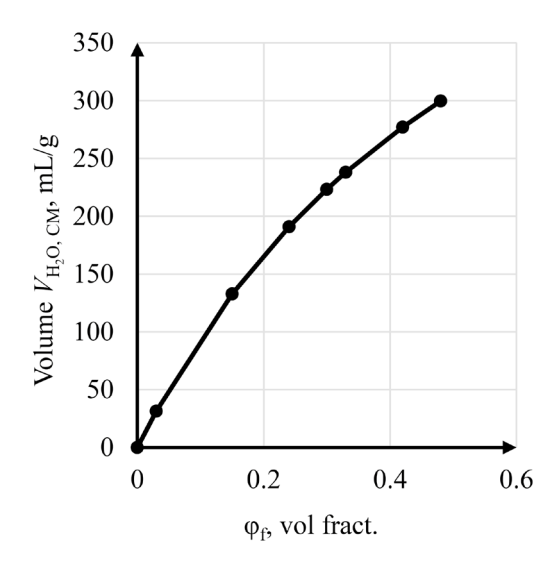
For the first time, data on the influence of disperse structure type on the OI and burning resistance for DFPCM based on EVA and dispersed flame-retardant filler are presented, allowing the purposeful design of compositions offering a predetermined resistance to burning.

The increase in the OI value when EVA is added to the PM with EP 10R flame-retardant filler is due to the decomposition of magnesium hydroxide and the release of water vapor. Water vapor and coke residue formation are the main factors increasing the OI and burning resistance of DFPCMs.

According to thermogravimetric analysis (TGA) [17], we determined the amount of water vapor emitted from 1 g of EP 10R flame-retardant filler (brucite) to be ~425 mL/g; the corresponding coke residue value was 32%.

Figure 4 shows the dependencies of the volume of water vapor emitted during brucite decomposition in DFPCM on the flame-retardant filler content and the generalized parameter Θ , which determines the type of DFPCM disperse structure.

According to the general pattern, the volume of water vapor increases with an increase in the content of the flame-retardant filler and a decrease in the generalized parameter; this however depends on the DFPCM structure type. From the above, it can be concluded that the higher the content of



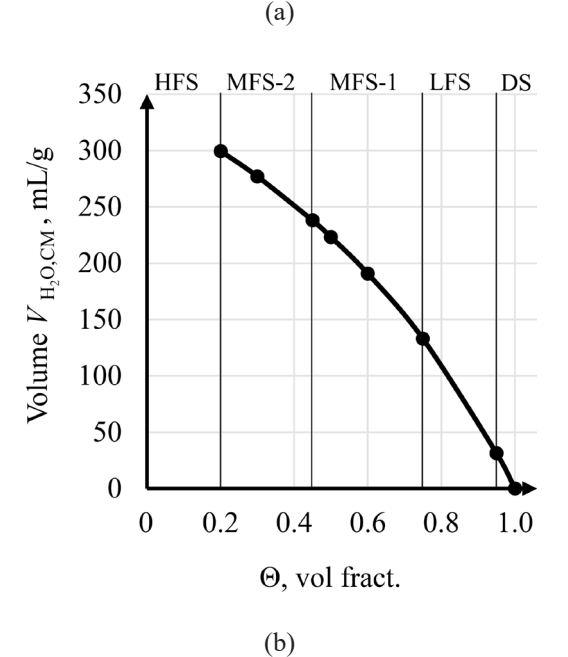
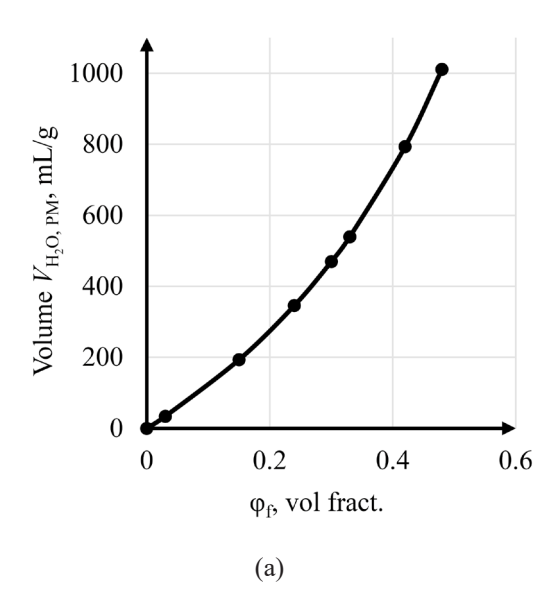


Fig. 4. Dependence of the volume of water vapor released during the decomposition of brucite in DFPCM:
(a) on the content of the flame-retardant filler,
(b) on the generalized parameter Θ.

water-releasing flame retardant during the decomposition reaction, the higher water content in the polymer composite material during burning.

Since the burning of DFPCM is due to the exothermic depolymerization of EVA, it is of interest to determine the volume of water vapor per 1 g of PM needed to inhibit the burning process.

Figure 5 shows the dependencies of the volume of water vapor emitted during brucite decomposition per 1 g of PM ($V_{\rm H_2O,PM}$, mL/g) on the flame-retardant filler content and generalized parameter Θ , which determines the DFPCM disperse structure type.



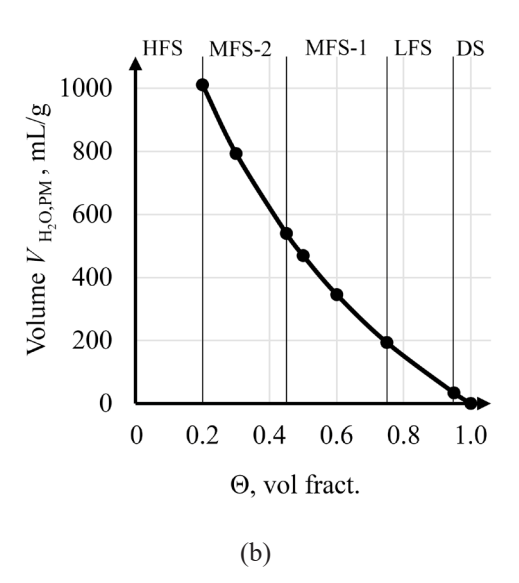


Fig. 5. Dependence of the volume of water vapor released during the decomposition of brucite per 1 g of polymer matrix:

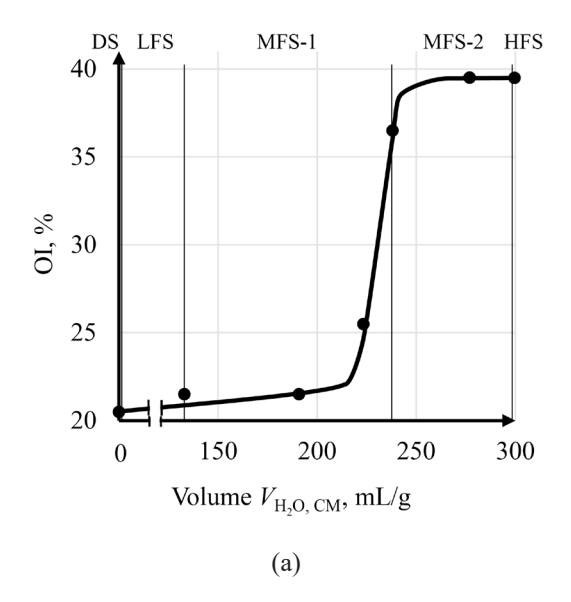
(a) on the content of the flame-retardant filler,

(b) on the generalized parameter Θ .

As can be seen from the obtained data, in order to obtain DFPCM with high OI (~40%) and the category V-0, the water vapor content per 1 g of PM should be at least 600 mL/g.

On the basis of the dependencies, which were obtained for the first time, it became possible to relate the OI of DFPCM with the volume of water vapor emitted during the decomposition of the EP 10R flame-retardant filler and the type of disperse structure (Fig. 6).

For the structure types of DS, LFS, and MFS-1 up to $\Theta \geq 0.60$ vol fract., the OI for EBA-based DFPCM is practically not increased (from 20.5 to 22%). A sharp increase in the OI (~2.0 times) occurs when more than 220 mL/g of water vapor is released in the area of change in the generalized parameter Θ from 0.60 to



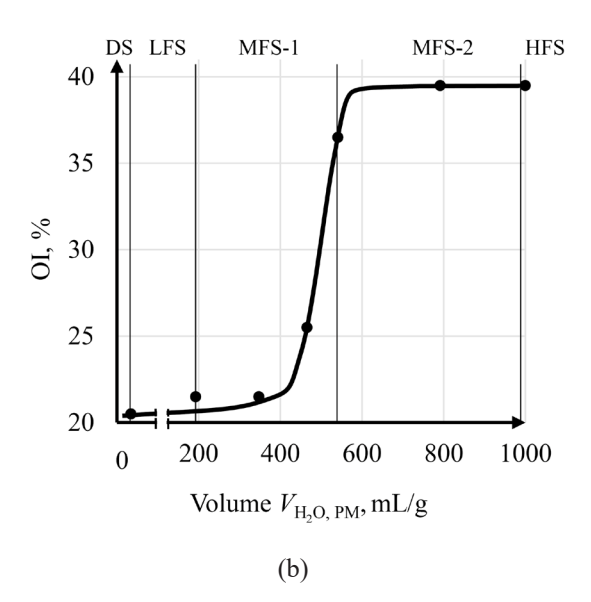


Fig. 6. Dependence of the oxygenation index for DFPCM on the volume of water vapor released during the decomposition of EcoPiren® brucite: (a) by 1 g of PCM, (b) by 1 g of the polymer matrix.

0.40 vol fract., which corresponds to the transition of the MFS-1 structure to MFS-2 and HFS. The maximum OI value of 40% for the EVA-based DFPCM is reached at $\Theta \approx 0.40$ vol fract. and a water vapor emission of 250 mL/g and $V_{\rm H_2O,PM} = 600$ mL/g. Further, as the volume of emitted water vapor increases [more than 250 (600) mL/g], the OI value for DFPCM with MFS-2 and HFS structures remains almost constant.

Thus, the optimum amount of water vapor to create a DFPCM with high OI value and resistance to burning is $V_{\rm H_2O,CM} \approx 250$ mL/g and $V_{\rm H_2O,PM} \approx 600$ mL/g, flame-retardant filler content of 0.36 vol fract., structure types are MFS-2 and HFS ($\Theta \leq 0.40$ vol fract.).

For the recommended OI value of $\approx 32\%$ ([18] and Footnote 3), the cable insulation of DFPCM based on EVA + EP 10R can have an MFS-1 structure with $\Theta \approx 0.47$ vol fract. and a water vapor amount of $V_{\rm H,O,CM} \approx 230$ mL/g and $V_{\rm H,O,PM} = 512$ mL/g.

Table 5 summarizes the OI and burning resistance as well as the characteristics of DFPCM based on EVA and EP 10R magnesium hydroxide ($d_{\rm av}=25~\mu m$ and $\phi_{\rm max}=0.60$ vol fract.) with different types of disperse structure.

The obtained results and new disperse structure model representations form a basis for designing the structure type, compositions of DFPCM with maximum value of OI and high burning resistance at known values of $\phi_{\rm max}$, coke residue, and amount of water vapor ($V_{\rm H_2O}$) emitted from 1 g of dispersed flameretardant filler.

It was shown in [19] that extruded and cast DFPCM are well processed into products if the condition $\Theta \approx 0.50\text{--}0.60$ vol fract. and the disperse structure of MFS-1 type (up to yield strength) is fulfilled.

Thus, in order to create high-tech and burning-resistant extrusion and injection-molded DFPCM, it is necessary to create an MFS-1 structure with $\approx 0.50-0.60$ vol fract. and a flame-retardant filler content of at least 0.36 vol fract.

The main problem of increasing the generalized parameter Θ to 0.50–0.60 vol fract. at a constant value of ϕ_f (not less than 0.36 vol fract.) is related to the creation of a new dispersed flame-retardant filler with a given fractional composition, in which the packing parameter ϕ max should reach the value of 0.70–0.75 vol fract. (increasing from 0.60 to 0.75 vol fract.). However, we do not consider these issues in the present work.

The following is an algorithm for the design of DFPCM formulations using a flame-retardant filler based on EVA (OI = 20.5%) and magnesium hydroxide (EP) with a high OI value and resistance to burning.

Based on the research carried out and the fundamental dependencies established, a general algorithm for the design of compositions and a given type of DFPCM structure with flame-retardant fillers with high OI and resistance to burning can be proposed:

- 1. To select of PM with a determination of OI, burning resistance according to GOST, and TGA test.
- 2. To choose a flame-retardant filler, study it by differential thermal analysis and TGA and determine the main characteristics: the temperature of the decomposition start ($T_{\rm start}$), the temperature of the loss of 10% of the mass ($T_{\rm 10}$), the temperature of the decomposition end ($T_{\rm end}$), the temperature

Demonstrate	Types of DFPCM dispersed structure based on EVA + EP 10R								
Parameters	DF	LFS	MFS-1			MFS-2			HFS
Θ , vol fract.	0.95	0.75	0.60	0.50	0.47	0.45	0.40	0.30	0.20
$\phi_{f^{\flat}}$ vol fract.	0.03	0.15	0.24	0.30	0.32	0.33	0.36	0.42	0.48
$\phi_{\mathfrak{p}}$ wt fract.	0.07	0.31	0.45	0.52	0.55	0.56	0.59	0.65	0.70
$V_{\rm H_2O,CM}$, mL/g	31.3	132.9	190.8	223.3	230.0	238.0	251.8	277.0	299.9
$V_{ m H_2O,PM}$, mL/g	33.7	192.6	346.9	465.2	512.2	540.9	614.1	791.4	999.7
OI, %	21.5	21.5	21.5	25.5	32	36.5	39.5	40.0	40.0
Category of resistance to burning	_	_	V-2	V-2	V-2	V-1	V-0	V-0	V-0

range of decomposition (ΔT), coke residue, and the volume of water vapor released from 1 g of flame-retardant filler ($V_{\rm H,O}$).

- 3. To determine the main characteristics of the dispersed flame-retardant filler: average particle diameter (d_{av}) , particle shape ratio (k_e) , specific surface area of particles (S_s) , particle size distribution, density, and porosity.
- 4. To experimentally determine the packing parameter (k_p) and the maximum dispersed filler content ϕ_{max} according to the known methods for flame-retardant filler [17, 18].
- 5. To calculate the value of the generalized parameter Θ for DFPCM at a known value of ϕ_{max} for a flame-retardant filler with its various contents, provided $\phi_f \leq \phi_{max}$, according to Eq. (2):

$$\Theta = (\varphi_{\text{max}} - f^{3} \varphi_{f}) / \varphi_{\text{max}} , \qquad (2)$$

where Θ is the share of PM to form a layer between the dispersed particles in the DFPCM; φ_{max} is the maximum content of the dispersed filler; φ_f is the content of the dispersed filler; $f^3 = (1+2\delta/d)$ is the ratio of the boundary layer thickness (δ) to the diameter (d) of the dispersed particles. For large, macro, and microparticles, the coefficient $f^3 \approx 1$.

- 6. To classify DFPCM according to the structural principle and determine the type of disperse structure of DFPCM (DS, LFS, MFS-1, MFS-2, and HFS) according to the values of the generalized parameter Θ at different contents of ϕ_r .
- 7. To calculate the flame-retardant filler content $(\phi_{vol\ f^2}$ vol fract.) for each type of DFPCM disperse structure by Eq. (3):

$$\varphi_{\text{vol f}} = (1 - \Theta) \cdot \varphi_{\text{max}} \,. \tag{3}$$

8. To calculate the flame-retardant filler content in mass units (ϕ_{wtf} , wt fract.) and determinate the compositions for each type of DFPCM disperse structure by Eq. (4):

$$\phi_{\text{wtf}} = \frac{\phi_{\text{volf}}}{\phi_{\text{volf}} \left(1 - \frac{\rho_{\text{p}}}{\rho_{\text{f}}}\right) + \frac{\rho_{\text{p}}}{\rho_{\text{f}}}} \text{ wt fract. }, \tag{4}$$

where $\rho_{_f}$ and $\rho_{_p}$ are the densities of the flame-retardant filler and PM.

9. To calculate the volume of released water vapor ($V_{\rm H_2O,CM}$ and $V_{\rm H_2O,PM}$) during the decomposition of the flame-retardant filler in DFPCM with

different structure types and flame-retardant filler content according to Eqs. (5) and (6):

$$V_{\rm H,o,cm} = V_{\rm H,o} \cdot \varphi_{\rm wtf}, \tag{5}$$

$$V_{\rm H,OPM} = V_{\rm H,O}/\varphi_{\rm wtp}, \tag{6}$$

where $\phi_{\text{wt p}}$ is the PM content in mass units.

10. To determine the optimum DFPCM composition and structure with high OI and resistance to burning (V-0) under the conditions:

$$V_{\rm H_2O,CM} \ge 250 \text{ mL/g}, V_{\rm H_2O,PM} \ge 600 \text{ mL/g}.$$

CONCLUSIONS

For the first time, the fundamental dependencies on OI and burning resistance of DFPCM based on EVA with flame-retardant fillers on the case study of EcoPyrene® magnesium hydroxide (brucite) were obtained. This forms the basis for determining the construction, type and parameters of disperse structure with the main characteristics of resistance to burning and OI.

The introduction of magnesium hydroxide (brucite) in the optimal amount in the EVA allows the OI to be increased from 20.5 to 40% (~2 times). The critical water vapor content for maximizing the OI value (up to ~40%) for DFPCM, which is at least $V_{\rm H_2O,CM} \approx 250$ mL/g and $V_{\rm H_2O,PM} \approx 600$ mL/g, was established.

The maximum burning resistance and OI are achieved for DFPCM based on EVA + EP 10R with a generalized parameter $\Theta \leq 0.40$ vol fract. for the MFS-2 structure type and the flame-retardant filler content $\phi_{\rm s}=0.36$ vol fract. (0.59 wt fract.).

Authors' contributions

- **K.A. Brekhova** conducting experiments, processing experimental data;
- **I.D. Simonov-Emel'yanov** the research concept, processing experimental data;
 - **A.A. Pykhtin** correction of the research concept.

The authors declare no conflicts of interest.

REFERENCES

- 1. Kablov V.F., Novopoltseva O.M., Kochetkov V.G., Lapina A.G. The main ways and mechanisms to improve fire- and heat resistance of materials. *Izvestiya Volgogradskogo gosudarstvennogo tekhnicheskogo universiteta (Izvestiya VolgGTU) = Izvestia VSTU*. 2016;(4):46–60 (in Russ.).
- 2. Nacharkina A.V., Zelenina I.V., Valueva M.I., Barbotko S.L. Fire safety of high-temperature carbon fiber reinforced plastics for aviation purposes (review). *Trudy VIAM = Proceedings of VIAM*. 2022;(7):134–150 (in Russ.). https://doi.org/10.18577/2307-6046-2022-0-7-134-150

СПИСОК ЛИТЕРАТУРЫ

- 1. Каблов В.Ф., Новопольцева О.М., Кочетков В.Г., Лапина А.Г. Основные способы и механизмы повышения огнетеплозащитной стойкости материалов. Известия Волгоградского государственного технического университета (Известия ВолгГТУ). Серия: Химия и технология элементорганических мономеров и полимерных материалов. 2016;(4):46–60.
- 2. Начаркина А.В., Зеленина И.В., Валуева М.И., Барботько С.Л. Пожаробезопасность высокотемпературных углепластиков авиационного назначения (обзор). *Труды ВИАМ.* 2022; (113):134–150. https://doi.org/10.18577/2307-6046-2022-0-7-134-150

- 3. Barbotko S.L., Bochenkov M.M., Volnyi O.S., Korobeinichev O.P., Shmakov A.G. Evaluation of the effectiveness of the fire retardants, promising for the creation of new polymer composite materials intended for aviation techniques. *Trudy VIAM = Proceedings of VIAM*. 2021;2(96):20–29 (in Russ.). https://doi.org/10.18577/2307-6046-2021-0-2-20-29
- 4. Garashchenko A.N., Berlin A.A., Kulkov A.A. Methods and means for providing required fire-safety indices of polymer composite structures. *Pozharovzryvobezopasnost = Fire and Explosion Safety*. 2019;28(2):9–30 (in Russ.). https://doi.org/10.18322/PVB.2019.28.02.9-30
- 5. Buravov B.A., Bochkarev E.S., Al'-Khamzavi A., Tuzhikov O.O., Tuzhikov O.I. Modern trends in the development of antipyrene for polymer compositions. Composition, properties, application. *Izvestiya Volgogradskogo gosudarstvennogo tekhnicheskogo universiteta (Izvestiya VolgGTU) = Izvestia VSTU*. 2020;12(247):7–24 (in Russ.). https://doi.org/10.35211/1990-5297-2020-12-247-7-24
- 6. Chizhov M.A., Khairullin R.Z. Toxicity of combustion products of polymeric materials with the introduction of flame retardants into their composition. Vestnik Kazanskogo tekhnologicheskogo universiteta = Bulletin of the Kazan Technological University. 2014;17(9):144–145 (in Russ.).
- 7. Lomakin S.M., Zaikov G.E., Mikitaev A.K., Kochnev A.M., Stoyanov O.V., Shkodich V F., Naumov S.V. Flame retardants for polymers. *Vestnik Kazanskogo tekhnologicheskogo universiteta = Bulletin of the Kazan Technological University*. 2012;15(7):71–86 (in Russ.).
- 8. Agafonova A.I., Koval' E.O., Maier E.A. Low flammability polypropylene compositions. *Izvestiya Tomskogo politekhnicheskogo universiteta = Bulletin of the Tomsk Polytechnic University*. 2011;318(3):136–140 (in Russ.).
- 9. Al'meeva L.R., Tangatarov A.F. Chlorinated paraffins as flame retardants. *Sovremennye tekhnologii obespecheniya grazhdanskoi oborony i likvidatsii posledstvii chrezvychainykh situatsii*. 2015;1–1(6):50–53 (in Russ.).
- 10. Zaripov I.I., Vikhareva. I.N., Builova E.A., Berestova T.V., Mazitova A.K. Additives to reduce the flammability of polymers. *Nanotekhnologii v stroitel'stve = Nanotechnologies in Construction*. 2022;14(2):156–161 (in Russ.). https://doi.org/10.15828/2075-8545-2022-14-2-156-161
- 11. Fomin D.L., Mazina L.A., Deberdeev T.R., Akhmetchin E.S., Ulitin N.V. Fireproof properties of PVC compositions when using some bromine-containing flame retardants. *Vestnik Kazanskogo tekhnologicheskogo universiteta = Bulletin of the Kazan Technological University.* 2012;15(18):104–106 (in Russ.).
- 12. Hornsby P.R., Watson C.L. A study of the mechanism of flame retardance and smoke suppression in polymers filled with magnesium hydroxide. *Polym. Degrad. Stab.* 1990;30(1):73–87. https://doi.org/10.1016/0141-3910(90)90118-Q
- 13. Svatikov A.Yu., Simonov-Emelyanov I.D. The thermal stability of polymer cable compounds with a flame-retarding filler. *Tonk. Khim. Tekhnol.* = *Fine Chem. Technol.* 2018;13(6):35–41 (in Russ.). https://doi.org/10.32362/2410-6593-2018-13-6-35-41
- 14. Simonov-Emelyanov I.D. Classification of dispersion-filled polymer composite materials relative to lattice types and structural principle. *Klei. Germetiki. Tekhnologii = Adhesives. Sealants. Technologies.* 2020;(1):8–13 (in Russ.). https://doi.org/10.31044/1813-7008-2020-0-1-8-13

- 3. Барботько С.Л., Боченков М.М., Вольный О.С., Коробейничев О.П., Шмаков А.Г. Оценка эффективности антипиренов, перспективных для создания новых полимерных композиционных материалов, предназначенных для авиационной техники. *Труды ВИАМ*. 2021;2(96):20–29. https://doi.org/10.18577/2307-6046-2021-0-2-20-29
- 4. Гаращенко А.Н., Берлин А.А., Кульков А.А. Способы и средства обеспечения требуемых показателей пожаробезопасности конструкций из полимерных композитов (обзор). *Пожаровзрывобезопасность*. 2019;28(2):9–30. https://doi.org/10.18322/PVB.2019.28.02.9-30
- 5. Буравов Б.А., Бочкарев Е.С., Аль-Хамзави А., Тужиков О.О., Тужиков О.И. Современные тенденции в разработке антипиренов для полимерных композиций. Состав, свойства, применение. Известия Волгоградского государственного технического университета (Известия ВолгГТУ). 2020;12(247):7–24. https://doi.org/10.35211/1990-5297-2020-12-247-7-24
- 6. Чижов М.А., Хайруллин Р.З. Токсичность продуктов горения полимерных материалов при введении в их состав антипиренов. *Вестинк Казанского технологического университета*. 2014;17(9):144–145.
- 7. Ломакин С.М., Заиков Г.Е., Микитаев А.К., Кочнев А.М., Стоянов О.В., Шкодич В.Ф., Наумов С.В. Замедлители горения для полимеров. Вестник Казанского технологического университета. 2012;15(7):71–86.
- 8. Агафонова А.И., Коваль Е.О., Майер Э.А. Композиции полипропилена пониженной горючести. *Известия Томского политехнического университета*. 2011;318(3):136–140.
- 9. Альмеева Л.Р., Тангатаров А.Ф. Хлорированные парафины как антипирены. Современные технологии обеспечения гражданской обороны и ликвидации последствий чрезвычайных ситуаций. 2015;1–1(6):50–53.
- 10. Зарипов И.И., Вихарева. И.Н., Буйлова Е.А., Берестова Т.В., Мазитова А.К. Добавки для понижения горючести полимеров. *Нанотехнологии в строительстве*. 2022;14(2):156–161. https://doi.org/10.15828/2075-8545-2022-14-2-156-161
- 11. Фомин Д.Л., Мазина Л.А., Дебердеев Т.Р., Ахметчин Э.С., Улитин Н.В. Пожаробезопасные свойства ПВХ-композиций при использовании некоторых бромсодержащих антипиренов. Вестник Казанского технологического университета. 2012;15(18):104—106.
- 12. Hornsby P.R., Watson C.L. A study of the mechanism of flame retardance and smoke suppression in polymers filled with magnesium hydroxide. *Polym. Degrad. Stab.* 1990;30(1):73–87. https://doi.org/10.1016/0141-3910(90)90118-Q
- 13. Сватиков А.Ю., Симонов-Емельянов И.Д. Термическая стабильность полимерных кабельных композиций с наполнителем-антипиреном. *Тонкие химические технологии*. 2018;13(6):35–41. https://doi.org/10.32362/2410-6593-2018-13-6-35-41
- 14. Симонов-Емельянов И.Д. Классификация дисперсно-наполненных полимерных композиционных материалов по типу решеток и структурному принципу. *Клеи. Герметики. Технологии.* 2020;(1):8–13. https://doi.org/10.31044/1813-7008-2020-0-1-8-13
- 15. Константинова Н.И., Симонов-Емельянов И.Д., Шебеко А.Ю, Кривошапкина О.В., Смирнов Н.В. Структура и воспламеняемость полимерных композиционных покрытий для наливных полов. *Пластические массы*. 2019;(3–4):50–54. https://doi.org/10.35164/0554-2901-2019-3-4-50-54

- 15. Konstantinova N.I., Simonov-Emelyanov I.D., Shebeko A.Yu, Krivoshapkina O.V., Smirnov N.V. The structure and inflammability of the polymer composite coatings for bulk floors. *Plasticheskie Massy*. 2019;(3–4):50–54 (in Russ.). https://doi.org/10.35164/0554-2901-2019-3-4-50-54
- 16. Simonov-Emelyanov I.D., Kharlamova K.I., Dergunova E.R. Oil absorption of dispersed fillers and determination of maximum fillers fraction in polymer composite materials. *Klei. Germetiki. Tekhnologii* = *Adhesives. Sealants. Technologies*. 2022;(3):18–24 (in Russ.). https://doi.org/10.31044/1813-7008-2022-0-3-18-24
- 17. Brekhova K.A., Simonov-Emelyanov I.D. FMagnesium hydroxide-based flame-retardant fillers for polymer materials and the effect of particle size on the dehydration process at high temperatures. *Plasticheskie Massy*. 2022;(7–8):44–47 (in Russ.). https://doi.org/10.35164/0554-2901-2022-7-8-44-47
- 18. Filina A.V., Komaristyi A.S. The use of electrical insulating materials in the manufacture of sheaths of cable products and wires. In: *Problems and Prospects of Russia's Development: A Youth Look into the Future: Proceedings of the 2nd All-Russian Scientific Conference*. Kursk: Universitetskaya kniga; 2019. P. 205–208 (in Russ.).
- 19. Krechetov D.D., Kovaleva A.N., Simonov-Emelyanov I.D. Rheological properties of dispersion-filled thermoplastics with different types of structures at various processing temperatures. *Plasticheskie Massy*. 2020;(9–10):19–22 (in Russ.). https://doi.org/10.35164/0554-2901-2020-9-10-19-22

- 16. Симонов-Емельянов И.Д., Харламова К.И., Дергунова Е.Р. Маслоемкость дисперсных порошков и определение максимального содержания наполнителей в полимерных композиционных материалах. Клеи. Герметики. Технологии. 2022;(3):18–24. https://doi.org/10.31044/1813-7008-2022-0-3-18-24
- 17. Брехова К.А., Симонов-Емельянов И.Д. Наполнители-антипирены на основе гидроксида магния для полимерных материалов и влияние размера частиц на процесс дегидратации при высоких температурах. Пластические массы. 2022;(7–8):44–47. https://doi.org/10.35164/0554-2901-2022-7-8-44-47
- 18. Филина А.В., Комаристый А.С. Использование электроизоляционных материалов при изготовлении оболочек кабельных изделий и проводов. В сб.: Проблемы и перспективы развития России: молодежный взгляд в будущее: сборник трудов 2-й Всероссийской научной конференции. Курск: Университетская книга; 2019. С. 205–208.
- 19. Кречетов Д.Д., Ковалева А.Н., Симонов-Емельянов И.Д. Реологические свойства дисперсно-наполненных термопластов с разным типом структур при температурах переработки. *Пластические массы*. 2020;(9–10):19–22. https://doi.org/10.35164/0554-2901-2020-9-10-19-22

About the authors:

Kristina A. Brekhova, Postgraduate Student, Department of Chemistry and Technology of Plastics and Polymer Composites Processing, M.V. Lomonosov Institute of Fine Chemical Technologies, MIREA – Russian Technological University (86, Vernadskogo pr., Moscow, 119571, Russia). E-mail: kr-otaku@mail.ru. https://orcid.org/0000-0002-3340-2490

Igor D. Simonov-Emel'yanov, Dr. Sci. (Eng.), Professor, Head of the Department of Chemistry and Technology of Plastics and Polymer Composites Processing, M.V. Lomonosov Institute of Fine Chemical Technologies, MIREA – Russian Technological University (86, Vernadskogo pr., Moscow, 119571, Russia). E-mail: igor.simonov1412@gmail.com. Scopus Author ID 6603181099, RSCI SPIN-code 7313-3844, https://orcid.org/0000-0002-6611-5746

Alexander A. Pykhtin, Cand. Sci. (Eng.), Associate Professor, Department of Chemistry and Technology of Plastics and Polymer Composites Processing, M.V. Lomonosov Institute of Fine Chemical Technologies, MIREA – Russian Technological University (86, Vernadskogo pr., Moscow, 119571, Russia). E-mail: nanocntpolimer@gmail.com. RSCI SPIN-code 2557-0070, https://orcid.org/0000-0002-1988-2301

Об авторах:

Брехова Кристина Алексеевна, аспирант кафедры химии и технологии переработки пластмасс и полимерных композитов Института тонких химических технологий им. М.В. Ломоносова ФГБОУ ВО «МИРЭА – Российский технологический университет» (119571, Россия, Москва, пр-т Вернадского, д. 86). E-mail: kr-otaku@mail.ru. https://orcid.org/0000-0002-3340-2490

Симонов-Емельянов Игорь Дмитриевич, д.т.н., профессор, заведующий кафедрой химии и технологии переработки пластмасс и полимерных композитов Института тонких химических технологий им. М.В. Ломоносова ФГБОУ ВО «МИРЭА – Российский технологический университет» (119571, Россия, Москва, пр-т Вернадского, д. 86). E-mail: igor.simonov1412@gmail.com. Scopus Author ID 6603181099, SPIN-код РИНЦ 7313-3844, https://orcid.org/0000-0002-6611-5746

Пыхтин Александр Алексеевич, к.т.н., доцент кафедры химии и технологии переработки пластмасс и полимерных композитов Института тонких химических технологий им. М.В. Ломоносова ФГБОУ ВО «МИРЭА – Российский технологический университет» (119571, Россия, Москва, пр-т Вернадского, д. 86). E-mail: nanocntpolimer@gmail.com. SPIN-код РИНЦ 2557-0070, https://orcid.org/0000-0002-1988-2301

The article was submitted: September 21, 2022; approved after reviewing: October 17, 2022; accepted for publication: March 20, 2023.

Translated from Russian into English by N. Isaeva Edited for English language and spelling by Thomas A. Beavitt

SYNTHESIS AND PROCESSING OF POLYMERS AND POLYMERIC COMPOSITES

СИНТЕЗ И ПЕРЕРАБОТКА ПОЛИМЕРОВ И КОМПОЗИТОВ НА ИХ ОСНОВЕ

ISSN 2686-7575 (Online) https://doi.org/10.32362/2410-6593-2023-18-2-123-134 UDC 678



RESEARCH ARTICLE

Biocomposite materials based on polyethylene and amphiphilic polymer-iron metal complex

Ilya Yu. Vasilyev[⊠]

Moscow Polytechnic University, Moscow, 107023 Russia [™]Corresponding author, e-mail: iljanaras@yandex.ru

Abstract

Objectives. To obtain and study the properties including degradability of polymer composite materials (PCM) based on low-density polyethylene (LDPE) obtained by introducing an environmentally friendly additive comprising an oxo-decomposing additive (ODA) based on an amphiphilic polymer-iron metal complex, which accelerates the process of polymer degradation.

Methods. PCMs based on LDPE and ODA were produced by processing in laboratory extruders in the form of strands, granules, and films. Thermodynamic properties were determined by differential scanning calorimetry in the temperature range 20–130°C. In order to assess the performance characteristics (physical and mechanical properties) of the PCM, tensile strength and elongation at break were determined. The biodegradability of PCM was evaluated by Sturm's method, with the biodegradation index being determined by the amount of CO_2 gas released as a result of microorganism activity, as well as composting by placing the PCMs for six months in biohumus. Changes in physical and mechanical properties and water absorption of the films during storage were evaluated. The photochemical degradability of the PCM was determined by exposing it to ultraviolet radiation for 100 h (equivalent to approximately one year of exposure of the films under natural conditions). The appearance of the composite samples following removal from the biohumus was determined using an optical microscope with $\times 50$ magnification in transmitted and reflected light.

Results. Following biodegradation by composting, the physical and mechanical properties of PCMs decrease by an average of 40.6%. This is related to the structural changes that occur in composites during storage in biohumus, i.e., the formation of a looser structure due to the development of large clusters of microorganisms that affect the formation of microcracks. It leads to the stage of fragmentation of the polyethylene matrix and indicates the progress of biological degradation of composites. In this case, the water absorption of the composite samples was 63% after 96 h of exposure. The biodegradability index determined by the Sturm method after 28 days of bubbling had changed by 82%, indicating an intensive biodegradation process. Exposure to ultraviolet radiation for 96 h resulted in the complete destruction of the PCMs, which turned into small "flakes." This method is the most effective for the degradation of LDPE- and ODA-based PCMs.

Conclusions. According to the results of the study of ODA-containing PCMs based on an amphiphilic polymer-iron metal complex, the tested filler-modifier can be recommended for the production of PCMs offering an accelerated degradation period.

Keywords: biodegradable compositions, polyethylene, oxo-decomposing additive, amphiphilic polymer-iron metal complex, filler, photochemical destruction

For citation: Vasilyev I.Yu. Biocomposite materials based on polyethylene and amphiphilic polymer-iron metal complex. Tonk. Khim. Tekhnol. = Fine Chem. Technol. 2023;18(2):123–134 (Russ., Eng.). https://doi.org/10.32362/2410-6593-2023-18-2-123-134

НАУЧНАЯ СТАТЬЯ

Биокомпозиционные материалы на основе полиэтилена и амфифильного полимерного металлокомплекса железа

И.Ю. Васильев[⊠]

Московский политехнический университет, Москва, 107023 Россия [™]Автор для переписки, e-mail: iljanaras@yandex.ru

Аннотация

Цели. Получение и исследование свойств, а также способности к деструкции полимерных композиционных материалов (ПКМ) на основе полиэтилена низкой плотности (ПЭНП), получаемых за счет введения экологически безопасной оксоразлагающейся добавки (ОРД) на основе амфифильного полимерного металлокомплекса железа, ускоряющей процесс разложения полимеров.

Методы. ПКМ на основе ПЭНП и ОРД получали в лабораторных экструдерах в виде стренг, гранул и пленок. Термодинамические свойства определяли дифференциально-сканирующей калориметрией в интервале температур 20– $130\,^{\circ}$ С. Для оценки эксплуатационных свойств (физико-механических характеристик) ПКМ определяли разрушающее напряжение при растяжении и относительное удлинение при разрыве. Способность к биоразложению ПКМ оценивали методом Штурма, определяя индекс биоразложения по количеству выделившегося CO_2 в результате жизнедеятельности микроорганизмов, а также путем компостирования, помещая ПКМ на полгода в биогумус. В процессе хранения определяли изменение физико-механических свойств, а также водопоглощение пленок. Способность ПКМ к фотохимической деструкции

определяли, подвергая образцы ультрафиолетовому излучению в отсутствии других источников света в течение 100 ч (эквивалентно приблизительно году экспозиции пленок в природных условиях). Внешний вид композиционных образцов после изъятия из биогумуса определяли при помощи оптического микроскопа с увеличением ×50 в проходящем и отраженном свете.

Результаты. В процессе биоразложения методом компостирования до полугода физико-механические свойства снижаются, в среднем, на 40.6%, что связано со структурными изменениями, протекающими в композитах в процессе хранения в биогумусе: формированием более рыхлой структуры вследствие образования и продуцирования крупных кластеров микроорганизмов, влияющих на образование микротрещин, что приводит к стадии фрагментации полиэтиленовой матрицы и свидетельствует о протекании процесса биологической деструкции композиционных материалов. При этом водопоглощение композиционных образцов спустя 96 ч экспозиции изменилось на 63%. Индекс биоразлагаемости, определенный методом Штурма по истечении 28 суток барботирования, изменился на 82%, что свидетельствует об интенсивном протекании процесса биоразложения. Воздействие ультрафиолетового излучения в течение 96 ч показало полное разрушение ПКМ до образования мелких «хлопьев». Данный метод является наиболее эффективным для процесса разложения ПКМ на основе ПЭНП и ОРД.

Выводы. Исследование ПКМ, содержащих ОРД на основе амфифильного полимерного металлокомплекса железа, показало, что исследуемый наполнитель-модификатор можно рекомендовать для изготовления ПКМ с ускоренным сроком разложения.

Ключевые слова: биоразлагаемые композиции, полиэтилен, оксо-разлагающаяся добавка, амфифильный полимерный металлокомплекс железа, наполнитель, фотохимическая деструкция

Для цитирования: Васильев И.Ю. Биокомпозиционные материалы на основе полиэтилена и амфифильного полимерного металлокомплекса железа. *Тонкие химические технологии*. 2023;18(2):123–134. https://doi.org/10.32362/2410-6593-2023-18-2-123-134

INTRODUCTION

Global production of synthetic plastics increases every year. Polymer materials are used in many areas of light industry, particularly in the packaging industry [1]. Polymeric films used for food packaging, plastic tableware, and rigid polymeric containers are typically used once and then disposed of [2]. Since this type of polymer waste does not decompose over time, its accumulation in landfills or dumps leads to environmental pollution [3]. One of the most environmentally-friendly approaches eliminating this problem involves development and use of biodegradable polymer materials based on natural materials that do not harm the environment or human health [4].

To date, a new approach to the production of biodegradable polymeric materials has been developed by producing products that retain their physical and mechanical properties during their service life and subsequently undergo physicochemical, chemical, biological and degradation processes under the influence of environmental factors to be easily incorporated into the metabolism of natural biosystems [5–7].

Biodegradable polymers comprise highmolecular-weight compounds that can be degraded in the presence of active biological organisms and under appropriate conditions. In the active medium, biodegradable polymers undergo significant structural changes in molecular weight and mechanical properties, contributing to the formation of a nutrient medium for the growth of microorganisms [8-10]. Under such conditions, processes of hydrolysis and photochemical destruction of biodegradable polymers generally occur. Materials break down into components that are part of the natural cycle: water, carbon dioxide, biomass. Unlike traditional polymers derived from petrochemical feedstocks, biodegradable polymers are capable of biodegradation in a short period of time [11–13].

There are several approaches to the development of biodegradable materials, including the use of natural polymers, particularly polysaccharides. In [14, 15], an application for native starch was identified. In [16], native starch was modified into thermoplastic starch to obtain biodegradable hybrid compositions after mixing with polyethylene [17]. The developed composites characterized by optimal physical and mechanical properties had a high biodegradation index [18–20].

Another direction that is gaining popularity in the creation of degradable polymers involves the introduction of molecules into the polymer structure that contain functional groups conducing to accelerated photo- or oxy-decomposition of the polymer [21]. This method seems to be the simplest and relatively cheapest way to solve some environmental problems. It is particularly important that the additives incorporated into the polymer be safe for use in the products made from such a composition [22]. One of the main criteria for biodegradable polymeric materials is harmlessness of biodegradable materials for the environment and humans, which must be confirmed by international certificates of compliance with international standards adopted in the of composting and biodegradation (EN 13432 European; ASTM D 6400—USA; and Green PLA—Japanese standards) [23].

Since it is also desirable that the additive be used to modify a range of polymers, an amphiphilic polymer with complexing groups capable of forming stable complexes with metal ions, in particular an amphiphilic polymer-metal complex (APM) of iron, was chosen for the modification of polyethylene in this work. Compared to salts of transition metals (Mn, Co, Cu, Ni, Fe), the toxicity of polymer metal complexes is significantly reduced [24]. Amphiphilic polymers have gained a strong position in many areas of industry, science, technology, and medicine thanks to the successful combination of the physicochemical properties of high molecular compounds and electrolytes [25]. The use of polymer metal complexes as degradation activators incorporated into polymer films is of great importance due to

their low toxicity, good compatibility with the hydrophobic matrix of polyolefins, and oxidative activity [26].

MATERIALS AND METHODS

As the objects of the study, we used:

- low-density polyethylene (LDPE) grade 15803-020 produced by *Kazanorgsintez* (Russia), having an average molecular weight of 1.8 · 10⁴ c.u.;
- oxo-decomposing additive (ODA) based on
 LDPE (50 wt %) and APM (50 wt %) (prooxidants in the form of iron carboxylate);
- polymer composite materials (PCM) based on polyethylene and ODA.

PCMs were obtained on a *Mashplast* extruder (Russia) equipped with either a strand or a flat-plate extrusion head at temperatures in the zones of the extruder ranging from 100°C (in the loading zone) to 125°C (in the head zone).

The melting temperature of the composites was determined by the endothermic maximum of the melting peak using the differential scanning calorimetry (DSC) on a DSC 214 calorimeter (PolymaNetzsch- $Ger\"{a}tebaug$ GmbH, Germany) in the temperature range from 20 to 130°C at a scanning speed of 5 deg/min and a sample weight of 10 ± 1 mg.

The physical and mechanical properties of the samples under tension were determined using the RM-50 testing machine (Mashplast, Russia), which is equipped with a computer interface using StretchTest software. The destructive tensile stress (σ_{α}) and elongation at break (ϵ_{α}) of the PCM were measured under normal conditions in accordance with GOST 14236-8111. The limit of the permissible value of the load measurement error did not exceed $\pm 1\%$. The maximum deviations in the diameter of the strand samples and the cross-sectional areas of the film samples were ± 0.2 mm and 2–3%, respectively. The average value was determined from 3–5 measurements. The tests were carried out at a deformation rate of 100 mm/min. Samples of film for testing were obtained using a special cutting device, the shape of the samples conforming to Type 1B (ENISO 527-3).

A composting method was used to assess the biodegradation dynamics of the PCM. The samples were placed in special trays with biohumus at a temperature of $23 \pm 2^{\circ}$ C and a humidity of $70 \pm 10\%$ and kept for one to six months. The degree of biodegradation of polymer compositions was

Тонкие химические технологии = Fine Chemical Technologies. 2023;18(2):123-134

¹ GOST 14236-81. USSR State Standard. Polymer films. Tensile test method. Moscow: Izd. Standartov; 1992.

assessed by changes in physical and mechanical properties: destructive tensile stress and elongation at break in accordance with GOST 54530-2011².

The Sturm method according to GOST 32433-2013³ was also used to determine the biodegradation period. This method consists in measuring the assimilation rate of the test material in an aqueous solution in the presence of bacterial microflora, which is recorded by the rate of carbon dioxide emission from the microorganisms. The exposure time was 28 days. To assess biodegradation, the biodegradation rate criterion was used; this is defined as the first derivative of the biodegradability index of PCM.

A determination of the effect of ultraviolet (UV) radiation on the studied PCM was carried out under the following conditions: the films were placed in a chamber isolated from external light sources. Two PRK-4 quartz lamps were used, providing radiation with a wavelength of $\lambda = 185-315$ nm. Film samples of 100×100 mm were placed at a distance of 30 cm from the UV lamps. 100 h of exposure in such a unit is known to be equivalent to approximately one year of exposure of films under natural conditions.

Optical studies of the appearance of the PCM after composting were carried out using an AxioImagerZ2m microscope (*Carl Zeiss*, Germany) at ×50 magnification in transmitted and reflected light.

RESULTS AND DISCUSSION

LDPE granules were mixed with ODA granules at different concentration ratios, where the share of ODA in film compositions was 1–5% by weight.

The mixed extrudate was produced as strands on a twin-screw extruder at the temperatures shown in the table.

The diameter of the extruder screws is 16 mm. The rotation speed of the screws ranged from 60 to 80 rpm. The strands were cut into granules about 2 mm in size at a knife rotation speed from 80 to 100 rpm. The schematic diagram of a twinscrew extruder is shown in Fig. 1.

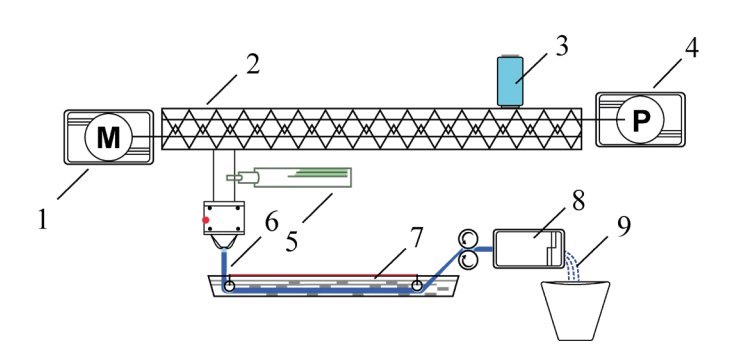


Fig. 1. Scheme of the device for obtaining composite granules: 1 – engine, 2 – twin-screw extruder, 3 – loading hopper, 4 – gearbox synchronized with the engine, 5 – pressure sensor, 6 – strand, 7 – cooling bath, 8 – granulator, and 9 – composite granules.

The pellets obtained on a twin-screw extruder were then fed into a laboratory single-screw extruder with a 12 mm screw diameter and extruded through a 130 mm wide flat die. At the same time, a barrier screw was used, which provided good homogenization of mixtures based on LDPE and ODA during the extrusion process, as well as high quality of the resulting polymer composite

Table. Temperature ranges for composite film fabrication

Composition	Temperature by extruder cylinder zones, °C						
	1 zone	2 zone	3 zone	4 zone	5 zone		
LDPE:ODA	100	110	120	125	125		

Note: LDPE – low-density polyethylene, ODA – oxo-degradable additive.

² GOST 54530-2011. National Standard of the Russian Federation. Resources saving. Packaging. Requirements, criteria and test scheme through composting and biodegradation. Moscow: Standartinform; 2019.

³ GOST 32433-2013. Interstate Standard. Testing of chemicals of environmental hazard. Ready biodegradability — CO₂ in sealed vessels. Moscow: Standartinform; 2019.

films. The rotation frequency of the screw varied from 60 to 80 rpm.

The material exiting the head was transferred to cooled receiving shafts, then stretched using a broaching device and wound into rolls to produce a composite film material. The diagram of a flat-slot single-screw extruder is shown in Fig. 2. At the same time, the laboratory samples were characterized by a uniform matte surface with no local holes or visible defects. The edges of the samples are even and smooth.

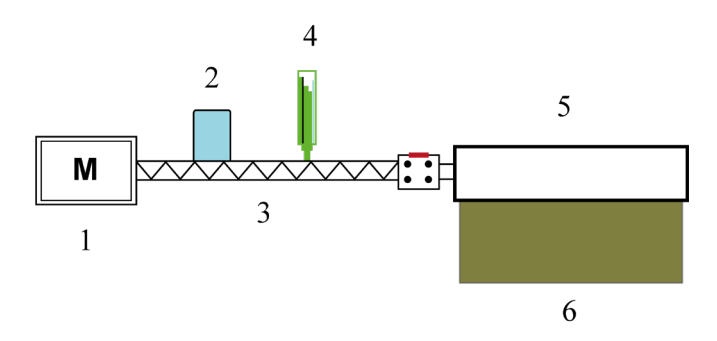


Fig. 2. Scheme of the extrusion device: 1 – engine, 2 – loading hopper, 3 – screw, 4 – pressure sensor, 5 – flat slot head, and 6 – melt of the finished composite.

The thermodynamic affinity of the components used for the manufacture of PCM was determined using DSC (Fig. 3). The temperature interval at which the technological process of obtaining composites was carried out is selected in the DSC diagram. It can be seen that there are two endo peaks in the diagram, one of which has a weak character and corresponds to the melting temperature of ODA (102.3°C), which can be explained by the low concentration in the composition of the composite. The second peak corresponds to the melting point of the starting polyethylene (111.3°C). Considering that the base of the modifier is comprised of synthetic thermoplastic non-polar polyethylene, this filler is characterized by properties inherent to the original polyolefin due to a narrow range of melting temperatures. This results in a more homogeneous composite structure during the extrusion process.

Water absorption is one of the most important properties of biodegradable compositions, as it indirectly characterizes the ability of the PCM to biodegrade. Figure 4 shows the kinetics of water absorption as a function of ODA concentration in the PCM.

As can be seen, LDPE absorbs virtually no water. For composites where ODA is incorporated at 1–3 wt %, water absorption varies slightly up to 1%.

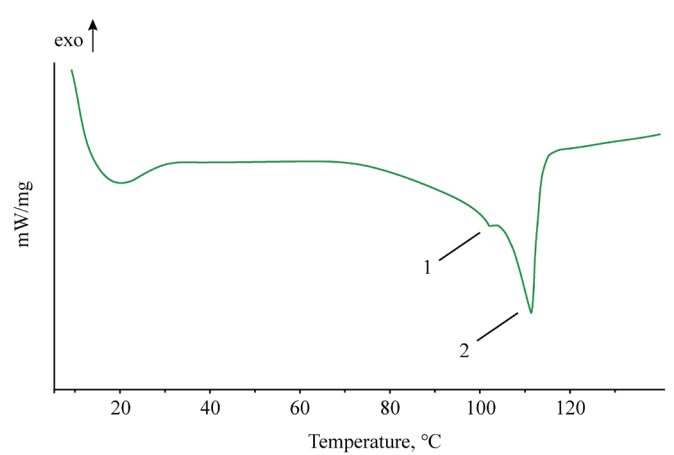


Fig. 3. Differential scanning calorimetry diagram of PCM based on LDPE:ODA = 95:5 wt %.

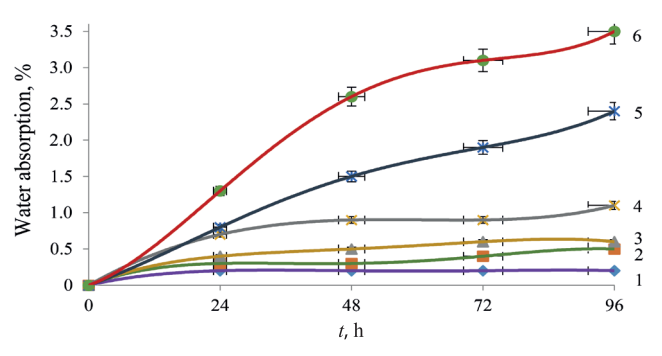


Fig. 4. PCM water absorption kinetics based on LDPE and ODA. 1 – Initial LDPE; ODA content, wt %: 2 – 1; 3 – 2; 4 – 3; 5 – 4; 6 – 5.

A significant change in water absorption was observed for the composite whose ODA mass fraction was 5%. This is probably due to structural changes in the polymer/filler system, where a looser structure is formed in the presence of ODA.

Comprehensive studies of polymer composite film samples to determine biodegradability were carried out using the composting and Sturm method.

The determination of the biodegradation process in biohumus was carried out at a temperature of 23°C and a soil humidity corresponding to $70 \pm 10\%$ of its maximum moisture capacity. The used soil was characterized by the presence of microorganisms. The composting times were one month, three months, and six months, respectively. The PCM samples and the control sample were placed on a substrate, pre-filled with a small amount of soil, and then completely covered with a layer of soil; constant

air access to the sample was provided to avoid suppressing the vital activity of the microorganisms. The degree of biodegradation of the samples during storage in biohumus was assessed by changes in parameters of physical and mechanical properties.

The results of determining the destructive tensile stress and elongation at break before and after biodegradation (one month, three months, and six months in biohumus) are shown in Figs. 5 and 6. These figures show that the tensile elongation break breaking stress and at composites not subjected biodegradation to decrease only slightly and are almost identical the original LDPE, of which is characterized by a more homogeneous composite structure.

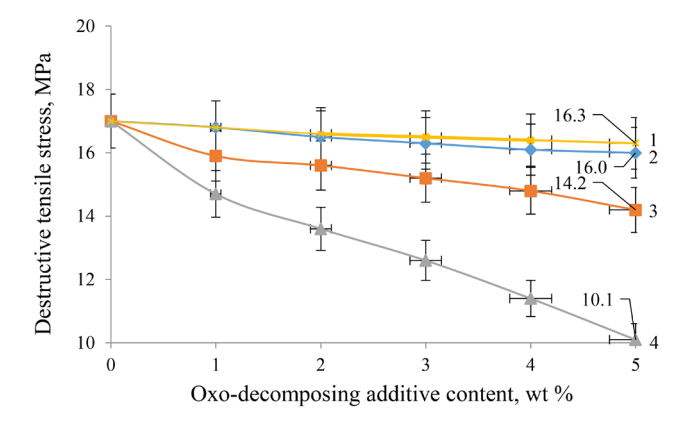


Fig. 5. Determination of tensile destructive stress of PCM based on LDPE and ODA before and after biodegradation: 1 – before biodegradation; 2 – a month of biodegradation; 3 – three months of biodegradation;

4 - six months of biodegradation.

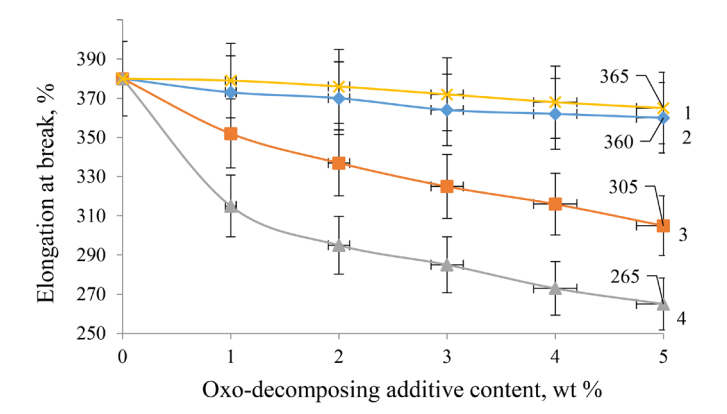


Fig. 6. Elongation at break of PCM based on LDPE and ODA before and after biodegradation: 1 – before biodegradation; 2 – a month of biodegradation;

3 – three months of biodegradation;

4 - six months of biodegradation.

After one month of biodegradation, the values of the destructive tensile stress decrease slightly, most likely due to the formation of microorganism colonies (Fig. 7a). During this period, no structural changes occur in the studied PCM. As the biodegradation period was extended to three months, a 16.5% decrease in mechanical properties was observed. The growth of microbial colonies resulted in a looser structure accompanied by the initial formation of microcracks (Fig. 7b), which characterize the biodegradation of the polyethylene matrix. After six months, the deformation properties had decreased by 25.0% due to active microbial colony growth, while the mechanical properties decreased by 40.6% (Fig. 7c). In addition, not only traces of microorganisms were observed on the composite films studied, but also clusters infected with microcolonies of bacteria. Thus, one group of microorganisms creates a substrate for another, which characterized by more intensive destruction composites, contributing to the formation of more microcracks. This indicates the initial stage of fragmentation of the polyethylene matrix and the progression of the biological degradation of composite materials.

The biodegradation index was determined by the Sturm method, which is based on estimating the activity of bacteria by carbon dioxide CO₂ emission. The more CO, is released, the higher the rate of biodegradation. During the research, a control flask with biohumus without a laboratory sample was taken as a standard, which excluded the influence of the nutrient medium of the biohumus itself. The rate of biodegradation was taken as the share of increase in CO, released as a result of the vital activity of microorganisms in the sample flask compared with the reference. Figure 8 shows the dependence of the determination of the PCM biodegradation index on the concentration of ODA in the PCM.

The observed lack of significant changes occurring during the experiment for LDPE is due to the absence of a structural modifier that contributes to the biological degradation of the polymer. On the other hand, the biodegradability index of the original ODA after 28 days of bubbling is 5.9%; this is due to the absence of a synthetic polymer from which the PCM was obtained. The experimental results for all the LDPE and ODA based composites studied are characterized by almost identical values after one week of bubbling. This is due to the period of initial multiplication of microorganisms, as in the case of biohumus, which were previously in an inactive form. In the period from 7 to 28 days, as the concentration ratio of ODA in composites increases, the biodegradation

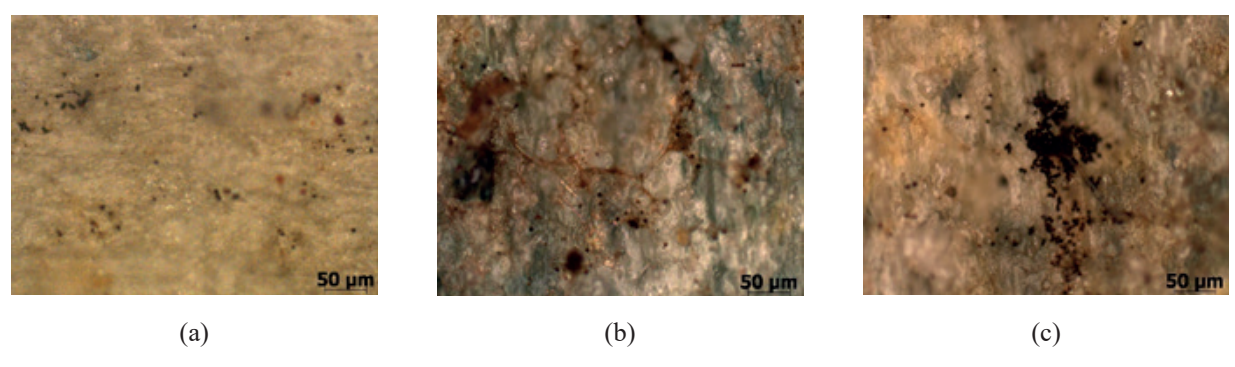


Fig. 7. Photomicrographs of PCM film samples based on LDPE:ODA = 95.5 wt % after removal from biohumus with an increase of $\times 50$: (a) 1 month; (b) 3 months; (c) 6 months.

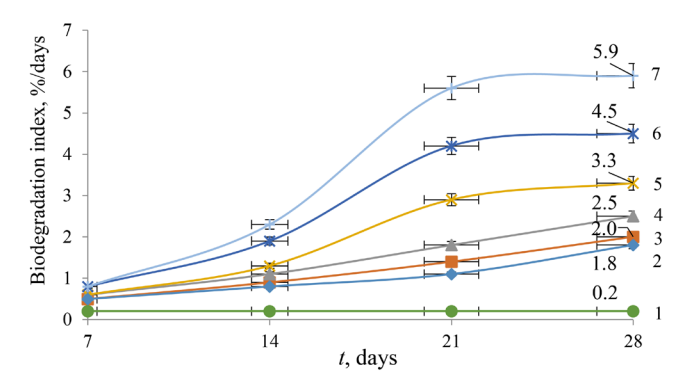


Fig. 8. Dependence of the biodegradation index of PCMs based on LDPE and ODA on ODA content. 1 - Initial LDPE; ODA content, wt %: 2 - 1; 3 - 2; 4 - 3; 5 - 4; 6 - 5; 7 - initial ODA.

index increases, presumably as a result of the active growth of microbial colonies due to the progress of the biodegradation process.

An accelerated test of the effect of UV radiation on the PCM under investigation was carried out. Irradiation of the original LDPE based film for 30 h did not result in any significant change in the properties of the sample: the external characteristics of the film remained the same, while the mechanical properties hardly changed following irradiation. For PCM based on LDPE and ODA with 5% modifier, the decrease in mechanical properties after 30 h of irradiation was 15–30% of the initial value, while no change in appearance was observed (Fig. 9a). The first changes in the appearance of the PCM based on LDPE and ODA at 5 wt % were observed after 60 h of UV exposure. At the same time, the reduction in mechanical properties was 30–55% of the initial value (Fig. 9b). Following 96 h of exposure, the sample was completely destroyed (Fig. 9b).

Thus, the described method turns out to be the most effective for the accelerated process of photochemical destruction of the developed PCMs based on LDPE and ODA based on APM iron.

CONCLUSIONS

Studies were conducted aimed at creating PCMs based on LDPE and ODA from APM iron, having an ODA content in the PCM of 1–5 wt %. Laboratory samples of PCM based on mixtures of LDPE and ODA were obtained by flat-gel extrusion at different concentration ratios.

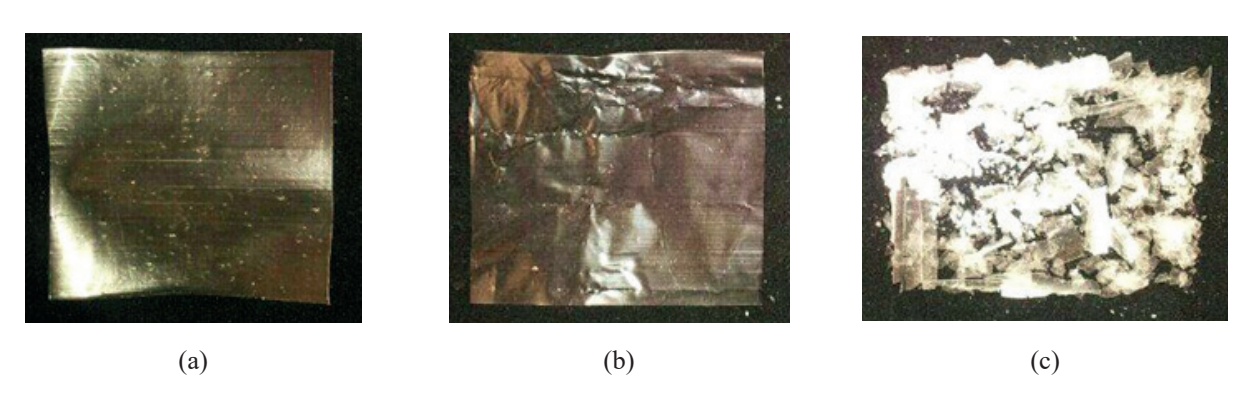


Fig. 9. Appearance of PCM based on LDPE:ODA = 95:5 wt % under UV radiation during: (a) 30 h; (b) 60 h; (c) 96 h.

The physicomechanical properties both before and after the biodegradation process were investigated. Prior to the biodegradation process, optimal physical and mechanical properties of PCM characterized by the thermodynamic compatibility of the components were observed to be practically at the level of LDPE. Following the biodegradation process, a 40.6% decrease in mechanical properties and a 25% decrease in deformation properties due to a change in the structure of the material were observed for a period of up to six months: the formation of a looser structure was accompanied by the formation of colonies of microorganisms with their subsequent reproduction, which in turn influenced the formation of microcracks indicating the initial stage of fragmentation of the polyethylene matrix.

The water absorption of the PCM was determined. It follows from the results of the experiment that the introduction of ODA up to 5 wt % increases the water absorption of the filled compositions by 63%.

The biodegradation of PCM was determined using the Sturm method. The biodegradation process was found to be dependent on the amount of modifier introduced. After 28 days of bubbling, the

biodegradation index changed by 82%, indicating that the biodegradation process is progressing.

An accelerated testing process for the resistance of PCM to UV radiation was carried out. Structural changes in the LDPE- and ODA- based PCM were observed to occur at a concentration of 5 wt % ODA start after 60 h of irradiation; these involved a change in the appearance of the sample as well as a decrease in its mechanical properties to 55%. The complete destruction of the sample after 96 h was associated with the formation of small "flakes."

Based on the obtained data, the use of APM-based ODA of iron as a polyolefin modifier to create biodegradable packaging materials can be recommended.

Acknowledgments

This work was supported by the Moscow Polytechnic University within the framework of the Vladimir Fortov grant.

The author declares no conflicts of interest.

REFERENCES

- 1. Litvyak V.V. Prospects of manufacture of modern packaging materials with application of biodelessed polymer compositions. *Zhurnal Belorusskogo gosudarstvennogo universiteta. Ekologiya = Journal of the Belarusian State University. Ecology.* 2019;(2):84–94 (in Russ.). URL: https://journals.bsu.by/index.php/ecology/article/view/2711/2295 (Accessed March 30, 2023).
- 2. Kalia S. *Biodegradable Green Composites*. John Wiley & Sons; 2016. 368 p. ISBN 978-1-11891109-9
- 3. Skoczinski P., Chinthapalli R., Carus M., Baltus W., de Guzman D., Käb H., Raschka A., Ravenstijn J. *Bio-based Building Blocks and Polymers Global Capacities, Production and Trends 2019 2024*. Hürth, Germany; 2020. 379 p. URL: https://renewable-carbon.eu/publications/product/bio-based-building-blocks-and-polymers-global-capacities-production-and-trends-2019-2024/ (Accessed March 30, 2023).

СПИСОК ЛИТЕРАТУРЫ

- 1. Литвяк В.В. Перспективы производства современных упаковочных материалов с применением биоразлагаемых полимерных композиций. Журнал Белорусского государственного университета. Экология. 2019;(2):84–94. URL: https://journals.bsu.by/index.php/ecology/article/view/2711/2295 (Дата обращения 30.03.2023).
- 2. Kalia S. *Biodegradable Green Composites*. John Wiley & Sons; 2016. 368 p. ISBN 978-1-11891109-9
- 3. Skoczinski P., Chinthapalli R., Carus M., Baltus W., de Guzman D., Käb H., Raschka A., Ravenstijn J. *Bio-based Building Blocks and Polymers Global Capacities, Production and Trends 2019 2024*. Hürth, Germany; 2020. 379 p. URL: https://renewable-carbon.eu/publications/product/bio-based-building-blocks-and-polymers-global-capacities-production-and-trends-2019-2024/ (Дата обращения 30.03.2023).

- 4. Nishat N., Malik A. Synthesis, spectral characterization thermal stability, antimicrobial studies and biodegradation of starch—thiourea based biodegradable polymeric ligand and its coordination complexes with [Mn(II), Co(II), Ni(II), Cu(II), and Zn(II)] metals. *J. Saudi Chem. Soc.* 2016;20(Suppl. 1):S7–S15. https://doi.org/10.1016/j.jscs.2012.07.017
- 5. Sudhakar Y.N., Selvakumar M. Lithium perchlorate doped plasticized chitosan and starch blend as biodegradable polymer electrolyte for supercapacitors. *Electrochimica Acta*. 2012;78:398–405. https://doi.org/10.1016/j.electacta.2012.06.032
- 6. Mendes J.F., Paschoalin R.T., Carmona V.B., Sena Neto A.R., Marques A.C.P., Marconcini J.M., Mattoso L.H.C., Medeiros E.S., Oliveira J.E. Biodegradable polymer blends based on corn starch and thermoplastic chitosan processed by extrusion. *Carbohydr. Polym.* 2016;137:452–458. https://doi.org/10.1016/j.carbpol.2015.10.093
- 7. Nguyen D.M., Do T.V.V., Grillet A.-C., Thuc H.H., Thuc C.N.H. Biodegradability of polymer film based on low density polyethylene and cassava starch. *Int. Biodeterior. Biodegradation.* 2016;115:257–265. https://doi.org/10.1016/j.ibiod.2016.09.004
- 8. Tang X., Alavi S. Recent advances in starch, polyvinyl alcohol based polymer blends, nanocomposites and their biodegradability. *Carbohydr. Polym.* 2011;85(1):7–16. https://doi.org/10.1016/j.carbpol.2011.01.030
- 9. Singh R., Sharma R., Shaqib M., Sarkar A., Dutt Chauhan K. Biodegradable polymers as packaging materials. In: *Biopolymers and their Industrial Applications. From Plant, Animal, and Marine Sources, to Functional Products.* 2021. Chapter 10. P. 245–259. https://doi.org/10.1016/B978-0-12-819240-5.00010-9
- 10. Ojogbo E., Ogunsona E.O., Mekonnen T.H. Chemical and physical modifications of starch for renewable polymeric materials. *Materials Today Sustainability*. 2020;7–8:100028. https://doi.org/10.1016/j.mtsust.2019.100028
- 11. Tudorachi N., Cascaval C.N., Rusu M., Pruteanu M. Testing of polyvinyl alcohol and starch mixtures as biodegradable polymeric materials. *Polym. Test.* 2000;19(7):785–799. https://doi.org/10.1016/S0142-9418(99)00049-5
- 12. Fonseca-García A., Jiménez-Regalado E., Aguirre-Loredo R.Y. Preparation of a novel biodegradable packaging film based on corn starch-chitosan and poloxamers. *Carbohydr. Polym.* 2021;251:117009. https://doi.org/10.1016/j.carbpol.2020.117009
- 13. Mittal A., Garg S., Bajpai S. Fabrication and characteristics of poly (vinyl alcohol)-starch-cellulosic material based biodegradable composite film for packaging application. *Materials Today: Proceedings.* 2020;21(3):1577–1582. https://doi.org/10.1016/j.matpr.2019.11.210
- 14. Vasilyev I.Yu., Ananyev V.V., Kolpakova V.V., Sardzhveladze A.S. Development of technology for producing biodegradable hybrid composites based on polyethylene, starch, and monoglycerides. *Tonk. Khim. Tekhnol.* = *Fine Chem. Technol.* 2020;15(6):44–55 (in Russ.). https://doi.org/10.32362/2410-6593-2020-15-6-44-55
- 15. Papakhin AA, Kolpakova V.V., Borodina Z.M., Sardzhveladze A.S., Vasilyev I.Yu. Modified porous starch in development of biodegradable composite polymer materials. *Tekhnika i tekhnologiya pishchevykh proizvodstv = Food Processing: Techniques and Technology.* 2020;50(3):549–558 (in Russ.). https://doi.org/10.21603/2074-9414-2020-3-549-558

- 4. Nishat N., Malik A. Synthesis, spectral characterization thermal stability, antimicrobial studies and biodegradation of starch—thiourea based biodegradable polymeric ligand and its coordination complexes with [Mn(II), Co(II), Ni(II), Cu(II), and Zn(II)] metals. *J. Saudi Chem. Soc.* 2016;20(Suppl. 1):S7–S15. https://doi.org/10.1016/j.jscs.2012.07.017
- 5. Sudhakar Y.N., Selvakumar M. Lithium perchlorate doped plasticized chitosan and starch blend as biodegradable polymer electrolyte for supercapacitors. *Electrochimica Acta*. 2012;78:398–405. https://doi.org/10.1016/j.electacta.2012.06.032
- 6. Mendes J.F., Paschoalin R.T., Carmona V.B., Sena Neto A.R., Marques A.C.P., Marconcini J.M., Mattoso L.H.C., Medeiros E.S., Oliveira J.E. Biodegradable polymer blends based on corn starch and thermoplastic chitosan processed by extrusion. *Carbohydr. Polym.* 2016;137:452–458. https://doi.org/10.1016/j.carbpol.2015.10.093
- 7. Nguyen D.M., Do T.V.V., Grillet A.-C., Thuc H.H., Thuc C.N.H. Biodegradability of polymer film based on low density polyethylene and cassava starch. *Int. Biodeterior. Biodegradation.* 2016;115:257–265. https://doi.org/10.1016/j.ibiod.2016.09.004
- 8. Tang X., Alavi S. Recent advances in starch, polyvinyl alcohol based polymer blends, nanocomposites and their biodegradability. *Carbohydr. Polym.* 2011;85(1):7–16. https://doi.org/10.1016/j.carbpol.2011.01.030
- 9. Singh R., Sharma R., Shaqib M., Sarkar A., Dutt Chauhan K. Biodegradable polymers as packaging materials. In: *Biopolymers and their Industrial Applications. From Plant, Animal, and Marine Sources, to Functional Products.* 2021. Chapter 10. P. 245–259. https://doi.org/10.1016/B978-0-12-819240-5.00010-9
- 10. Ojogbo E., Ogunsona E.O., Mekonnen T.H. Chemical and physical modifications of starch for renewable polymeric materials. *Materials Today Sustainability*. 2020;7–8:100028. https://doi.org/10.1016/j.mtsust.2019.100028
- 11. Tudorachi N., Cascaval C.N., Rusu M., Pruteanu M. Testing of polyvinyl alcohol and starch mixtures as biodegradable polymeric materials. *Polym. Test.* 2000;19(7):785–799. https://doi.org/10.1016/S0142-9418(99)00049-5
- 12. Fonseca-García A., Jiménez-Regalado E., Aguirre-Loredo R.Y. Preparation of a novel biodegradable packaging film based on corn starch-chitosan and poloxamers. *Carbohydr. Polym.* 2021;251:117009. https://doi.org/10.1016/j.carbpol.2020.117009
- 13. Mittal A., Garg S., Bajpai S. Fabrication and characteristics of poly (vinyl alcohol)-starch-cellulosic material based biodegradable composite film for packaging application. *Materials Today: Proceedings*. 2020;21(3):1577–1582. https://doi.org/10.1016/j.matpr.2019.11.210
- 14. Васильев И.Ю., Ананьев В.В., Колпакова В.В., Сарджвеладзе А.С. Разработка технологии получения биоразлагаемых композиций на основе полиэтилена, крахмала и моноглицеридов. *Тонкие химические технологии*. 2020;15(6):44–55. https://doi.org/10.32362/2410-6593-2020-15-6-44-55
- 15. Папахин А.А., Колпакова В.В., Бородина З.М., Сарджвеладзе А.С., Васильев И.Ю. Применение модифицированного пористого крахмала для создания биоразлагаемых композиционных полимерных материалов. *Техника и технология пищевых производств*. 2020;50(3):549–558. http://doi.org/10.21603/2074-9414-2020-3-549-558

- 16. Vasilyev I.Yu., Ananyev V.V., Chernov M.E. Biodegradable packaging materials based on low density polyethylene, starch and monoglycerides. *Tonk. Khim. Tekhnol.* = *Fine Chem. Technol.* 2022;17(3):231–241 (Russ., Eng.). https://doi.org/10.32362/2410-6593-2022-17-3-231-241
- 17. Vasiliev I.Yu., Ananyev V.V., Kolpakova V.V., Sardzhveladze A.S. Biodegradable materials based on low-density polyethylene, starch and monoglycerides. *Vse Materialy. Entsiklopedicheskii Spravochnik = All Materials. Encyclopedic Reference Manual.* 2021;(11):20–26 (in Russ.). https://doi.org/10.31044/1994-6260-2021-0-11-20-26
- 18. Vasilyev I., Ananiev V., Sultanova Yu., Kolpakova V. Effect of the biodegradable compounds composition with monoglycerides on mechanical properties. In: *Materials Science Forum.* 2021;1031:7–16. https://doi.org/10.4028/www.scientific.net/MSF.1031.7
- 19. Vasil'ev I.Y., Anan'ev V.V., Sultanova Y.M., Kolpakova V.V. The influence of the composition of polyethylene, starch, and monoglyceride biodegradable compositions on their physicomechanical properties and structure. *Polym. Sci. Ser. D.* 2022;15(1):122–127. https://doi.org/10.1134/S1995421222010257
- 20. Lukin N.D., Kolpakova V.V., Usachev I.S., Sardzhvelazhdze A.S., Solomin D.A., Vasil'ev I.Yu. Modification of polymer compositions with thermoplastic starch for bio-dependable packaging products. In: Biotekhnologiya: sostoyanie i perspektivy razvitiya: Materialy mezhdunarodnogo kongressa (Biotechnology: State of the Art and Perspectives: Proceedings of the International Congress). Moscow: RED GROUP; 2019. P. 102–104 (in Russ.).
- 21. Tabasum S., Younas M., Zaeem M.A., Majeed I., Majeed M., Noreen A., Iqbal N.M., Zia K.M. A review on blending of corn starch with natural and synthetic polymers, and inorganic nanoparticles with mathematical modeling. *Int. J. Biol. Macromol.* 2019;122:969–996. https://doi.org/10.1016/j.ijbiomac.2018.10.092
- 22. Ren H., Ouyang G., Iyer S.S., Yang Y.-T. Mechanism and process window study for die-to-wafer (D₂W) hybrid bonding. *ECS J. Solid State Sci. Technol.* 2021;10(6):064008. https://doi.org/10.1149/2162-8777/ac0a52
- 23. Tokareva N.E. Evaluation of the rate of decomposition of polyethylene with D₂W additive. In: *Innovatsionnye faktory razvitiya transporta*. Teoriya i praktika. Materialy mezhdunarodnoi nauchno-prakticheskoi konferentsii (Innovative Factors of Transport Development. Theory and Practice. Materials of the International Scientific and Practical Conference). Novosibirsk: STU; 2018. P. 79–81 (in Russ.).
- 24. Obydenova A.A., Myalenko D.M. Study of physical, mechanical and organoleptic characteristics of biodegradable polymer packaging based on polyethylene modified with oxo-additive D₂W. In: Sbornik tezisov X Mezhdunarodnoi nauchnoi konferentsii studentov, aspirantov i molodykh uchenykh (Food Innovation and Biotechnology. Collection of Abstracts of the 10th International Scientific Conference of Students, Graduate Students and Young Scientists). V. 1. Kemerovo: KemSU; 2022. P. 298–300 (in Russ.).
- 25. Ershova O.V., Bodyan L.A., Ponomarev A.P., Bakhaeva A.N. The effect of chemical destruction on the change in physical and mechanical properties of polymer films with D_2W additive. Sovrementy problemy nauki i obrazovaniya = Modern Problems of Science and Education. 2015;1(1):1981 (in Russ.).
- 26. Lukanina Yu.K., Khvatov A.V., Koroleva A.V., Popov A.A., Kolesnikova N.N. *Okso-razlagayushchaya dobavka k poliolefinam (Oxo-decomposing additive for polyolefins*): RF Pat. 2540273 C1. Publ. 10.02.2015 (in Russ.).

- 16. Васильев И.Ю., Ананьев В.В., Чернов М.Е. Биоразлагаемые упаковочные материалы на основе полиэтилена низкой плотности, крахмала и моноглицеридов. *Тонкие химические технологии*. 2022;17(3):231–241. https://doi.org/10.32362/2410-6593-2022-17-3-231-241
- 17. Васильев И.Ю., Ананьев В.В., Колпакова В.В, Сарджвеладзе А.С. Биоразлагаемые материалы на основе ПЭНП, крахмала и моноглицеридов. *Все материалы. Энциклопедический справочник.* 2021;(11):20–26. https://doi.org/10.31044/1994-6260-2021-0-11-20-26
- 18. Vasilyev I., Ananiev V., Sultanova Yu., Kolpakova V. Effect of the biodegradable compounds composition with monoglycerides on mechanical properties. In: *Materials Science Forum*. 2021;1031:7–16. https://doi.org/10.4028/www.scientific.net/MSF.1031.7
- 19. Vasil'ev I.Y., Anan'ev V.V., Sultanova Y.M., Kolpakova V.V. The influence of the composition of polyethylene, starch, and monoglyceride biodegradable compositions on their physicomechanical properties and structure. *Polym. Sci. Ser. D.* 2022;15(1):122–127. https://doi.org/10.1134/S1995421222010257
- 20. Лукин Н.Д., Колпакова В.В., Усачев И.С., Сарджвелаждзе А.С., Соломин Д.А., Васильев И.Ю. Модификация полимерных композиций с термопластичным крахмалом для биоразлагаемой упаковочной пленки. В сб.: Биотехнология: состояние и перспективы развития: Материалы международного конгресса. М.: ООО «РЭД ГРУПП»; 2019. С. 102–104.
- 21. Tabasum S., Younas M., Zaeem M.A., Majeed I., Majeed M., Noreen A., Iqbal N.M., Zia K.M. A review on blending of corn starch with natural and synthetic polymers, and inorganic nanoparticles with mathematical modeling. *Int. J. Biol. Macromol.* 2019;122:969–996. https://doi.org/10.1016/j.ijbiomac.2018.10.092
- 22. Ren H., Ouyang G., Iyer S.S., Yang Y.-T. Mechanism and process window study for die-to-wafer (D2W) hybrid bonding. *ECS J. Solid State Sci. Technol.* 2021;10(6):064008. https://doi.org/10.1149/2162-8777/ac0a52
- 23. Токарева Н.Е. Оценка скорости разложения полиэтилена с добавкой D2W. В сб.: Инновационные факторы развития транспорта. Теория и практика. Материалы международной научно-практической конференции. Новосибирск: СГУПС; 2018. С. 79–81.
- 24. Обыденова А.А., Мяленко Д.М. Исследование физико-механических и органолептических характеристики биоразлагаемой полимерной упаковки на основе полиэтилена, модифицированного оксо-добавкой D2W. В сб.: Пищевые инновации и биотехнологии. Сборник тезисов X Международной научной конференции студентов, аспирантов и молодых ученых. Т. 1. Кемерово: КемГУ; 2022. С. 298–300.
- 25. Ершова О.В., Бодьян Л.А., Пономарев А.П., Бахаева А.Н. Влияние химической деструкции на изменение физико-механических свойств упаковочных полимерных пленок с добавкой D2W. Современные проблемы науки и образования. 2015;1(1):1981.
- 26. Луканина Ю.К., Хватов А.В., Королева А.В., Попов А.А., Колесникова Н.Н. *Оксо-разлагающая добавка к полиолефинам*: Пат. 2540273 С1 РФ. Заявка № 2013155023/04; заявл. 12.12.2013; опубл. 10.02.2015.

Biocomposite materials based on polyethylene ...

About the author:

Ilya Yu. Vasilyev, Researcher, Lecturer, Department of Innovative Materials for the Print Media Industry, Polygraphic Institute, Moscow Polytechnic University (38, Bolshaya Semenovskaya ul., Moscow, 107023, Russia). E-mail: iljanaras@yandex.ru. Scopus Author ID 57195569317, ResearcherID ABW-6525-2022, RSCI SPIN-code 2038-4156, https://orcid.org/0000-0001-8488-5907

Об авторе:

Васильев Илья Юрьевич, научный сотрудник, преподаватель кафедры «Инновационные материалы принтмедиаиндустрии» Полиграфического института ФГАОУ «Московский политехнический университет» (107023, Россия, Москва, ул. Большая Семеновская, 38). E-mail: iljanaras@yandex.ru. Scopus Author ID 57195569317, ResearcherID ABW-6525-2022, SPIN-код РИНЦ 2038-4156, https://orcid.org/0000-0001-8488-5907

The article was submitted: October 11, 2022; approved after reviewing: February 14, 2023; accepted for publication: March 24, 2023.

Translated from Russian into English by N. Isaeva Edited for English language and spelling by Thomas A. Beavitt

ANALYTICAL METHODS IN CHEMISTRY AND CHEMICAL TECHNOLOGY

АНАЛИТИЧЕСКИЕ МЕТОДЫ В ХИМИИ И ХИМИЧЕСКОЙ ТЕХНОЛОГИИ

ISSN 2686-7575 (Online)

https://doi.org/10.32362/2410-6593-2023-18-2-135-167

UDC 543.5



REVIEW ARTICLE

Analysis of nanoparticles and nanomaterials using X-ray photoelectron spectroscopy

Anatoly A. Ischenko $^{1,\boxtimes}$, Mikhail A. Lazov $^{1,\boxtimes}$, Elena V. Mironova 1 , Alexey Yu. Putin 1 , Andrey M. Ionov 2 , Pavel A. Storozhenko 3

Abstract

Objectives. The main aim of this review is to summarize the existing knowledge on the use of X-ray photoelectron spectroscopy (XPS) for the characterization of nanoparticles and nanomaterials. **Results.** XPS or electron spectroscopy for chemical analysis can provide information on the qualitative and quantitative composition, valence states of the elements of the samples under study, the chemical composition of the surface and interfaces that determine the properties of nanoparticles and nanostructured materials. The review describes the role of several different methods for the characterization of nanomaterials, highlights their advantages and limitations, and the possibilities of an effective combination. The main characteristics of XPS are described. Various examples of its use for the analysis of nanoparticles and nanomaterials are given in conjunction with additional methods to obtain complementary information about the object under study.

Conclusions. XPS provides depth information comparable to the size of nanoparticles (up to 10 nm depth from the surface) and does not cause significant damage to the samples. Two disadvantages of XPS analysis are sample preparation requiring a dry solid form without contaminations and data interpretation. XPS provides information not only on the chemical

¹MIREA – Russian Technological University (M.V. Lomonosov Institute of Fine Chemical Technologies), Moscow, 119571 Russia

²Institute of Solid State Physics, Russian Academy of Sciences, Chernogolovka, Moscow oblast, 142432 Russia

³GNIIKHTEOS, Moscow, 105118 Russia

[™]Corresponding author, e-mail: aischenko@yasenevo.ru, lazovm@gmail.com

identity, but also on the dielectric properties of nanomaterials, recording their charging/discharging behavior. Chemical information from the surface of nanoparticles analyzed by XPS can be used to estimate the thickness of nanoparticle coatings. XPS has a high selectivity, since the resolution of the method makes it possible to distinguish a characteristic set of lines in the photoelectron spectrum at kinetic energies determined by the photon energy and the corresponding binding energies in elements. The intensity of the lines depends on the concentration of the respective element. Obtaining a sufficiently complete picture of the properties of nanomaterials requires the use of a group of complementary instrumental methods of analysis.

Keywords: X-ray photoelectron spectroscopy, nanoparticles, nanomaterials, valence states of elements, surface, interfaces, diffraction methods, spectral methods

For citation: Ischenko A.A., Lazov M.A., Mironova E.V., Putin A.Yu., Ionov A.M., Storozhenko P.A. Analysis of nanoparticles and nanomaterials using X-ray photoelectron spectroscopy. *Tonk. Khim. Tekhnol.* = Fine Chem. Technol. 2023;18(2):135–167 (Russ., Eng.). https://doi.org/10.32362/2410-6593-2023-18-2-135-167

ОБЗОРНАЯ СТАТЬЯ

Анализ наночастиц и наноматериалов методом рентгеновской фотоэлектронной спектроскопии

А.А. Ищенко $^{1,\boxtimes}$, М.А. Лазов $^{1,\boxtimes}$, Е.В. Миронова 1 , А.Ю. Путин 1 , А.М. Ионов 2 , П.А. Стороженко 3

¹МИРЭА – Российский технологический университет (Институт тонких химических технологий им. М.В. Ломоносова), Москва, 119571 Россия

²Институт физики твердого тела Российской академии наук, Черноголовка, Московская область, 142432 Россия

³Государственный научный центр Российской Федерации АО "ГНИИХТЭОС", Москва, 105118 Россия

[™]Автор для переписки, e-mail: aischenko@yasenevo.ru, lazovm@gmail.com

Аннотация

Цели. Основная цель данного обзора – обобщить существующие знания об использовании метода рентгеновской фотоэлектронной спектроскопии (РФЭС) для характеризации наночастиц и наноматериалов.

Результаты. Метод РФЭС или электронной спектроскопии для химического анализа может предоставить информацию о качественном и количественном составе, валентных состояниях элементов исследуемых образцов, химическом составе поверхности и границ раздела, которые определяют свойства наночастиц и наноструктурных материалов. В обзоре описана роль нескольких различных методов для характеристики наноразмерных материалов, подчеркнуты их преимущетва, ограничения и возможности эффективной комбинации. Описаны основные характеристики РФЭС. Приведены различные примеры ее использования для анализа наночастиц и наноматериалов в совокупности с дополнительными методами для получения комплементарной информации об изучаемом объекте.

Выводы. РФЭС предоставляет информацию о глубине, сравнимой с размером наночастиц (до 10 нм глубины от поверхности), и не вызывает значительного повреждения образцов. Двумя недостатками анализа РФЭС являются подготовка образцов (требуется сухая твердая форма без загрязнения) и интерпретация данных. РФЭС предоставляет информацию не только о химической идентичности, но и о диэлектрических свойствах наноматериалов, регистрируя их поведение при зарядке/разрядке. Химическая информация с поверхности наночастиц, проанализированная с помощью РФЭС, может использоваться для оценки толщины покрытий наночастиц. РФЭС обладает высокой селективностью, поскольку разрешающая способность метода позволяет различить характерный набор линий в фотоэлектронном спектре при кинетических энергиях, определяемых энергией фотонов и соответствующими энергиями связи в элементах. Интенсивность линий зависит от концентрации соответствующего элемента. Получение достаточно полной картины свойств наноматериалов требует использования группы взаимодополняющих инструментальных методов анализа.

Ключевые слова: рентгеновская фотоэлектронная спектроскопия, наночастицы, наноматериалы, валентные состояния элементов, поверхность, границы раздела, дифракционные методы, спектральные методы

Для ципирования: Ищенко А.А., Лазов М.А., Миронова Е.В., Путин А.Ю., Ионов А.М., Стороженко П.А. Анализ наночастиц и наноматериалов методом рентгеновской фотоэлектронной спектроскопии. *Тонкие химические технологии.* 2023;18(2):135–167. https://doi.org/10.32362/2410-6593-2023-18-2-135-167

INTRODUCTION

As a rapidly growing class of materials, nanostructures are of great interest for many applications. Several methods are used to characterize the size, crystal structure, elemental composition, and many other physicochemical, chemical, and physical properties of nanoparticles. The different strengths and weaknesses of each method make it difficult to choose the most appropriate one, and a combined approach to characterization is often required. In addition, it is necessary that researchers from different fields overcome the reproducibility problems of and reliable characterization of nanomaterials after their synthesis and further processing (e.g. annealing steps).

Determination of the structure, qualitative and quantitative chemical composition of nanomaterials consisting of nanoparticles (quantum dots) or nanofilms (two-dimensional structures), and the relationship of these characteristics with spectral properties is one of the central problems in the study of nano-objects.

The method of X-ray photoelectron spectroscopy (XPS) or electron spectroscopy for chemical analysis, as shown in the proposed review, can provide information on the qualitative and quantitative composition, valence states of the elements of the samples under study, the chemical composition of the surface and interfaces that determine the properties of nanostructured materials.

The number of studies using XPS has increased more than 15-fold over the past 30 years. In the last year alone, XPS has been mentioned in more than 9000 published articles.

XPS is not usually considered as a method with horizontal (lateral) nano-resolution. However, the electrons detected by this method travel distances measured in nanometers and can be used to obtain sufficient information about the structure of nanometer-sized samples on the surface and in the near-surface layer. Although the possibility of obtaining information at the nanometer scale from samples with a flat surface seems more obvious, XPS data can be used to determine the composition of nanoparticles. It is also possible

to obtain information about coatings and layers in nanoparticles under conditions where other surface investigation methods cannot be applied.

The main purpose of the review is to summarize the existing knowledge on the use of the XPS method for the characterization of nanoparticles and nanomaterials.

NANOMATERIALS

Nanomaterials are materials that have linear dimensions in one or more directions from a few nm to 100 nm (Fig. 1). Restrictions on the size of nanostructures make it possible to divide them into zero-, one-, two-, and three-dimensional [1–3].

Nanomaterials occupy an intermediate position between atoms and bulk crystalline and amorphous solids. In this regard, the unique properties of nanoparticles are determined by surface (high ratio of the fraction of surface atoms to volume) and quantum-size effects, especially when the particle sizes are comparable with the correlation radii of physical phenomena (the mean free path of electrons, phonons, the size of the magnetic domain or exciton, etc.). The electronic properties of the material depend on these factors, from which many physical and physicochemical characteristics follow, for example, the presence of unique optical, electrical, magnetic, mechanical, catalytic properties, as well as the possibility of surface functionalization [2, 3].

Features of the electronic properties, which manifest themselves as the particle size approaches nanometers, are described in monograph [3] and a number of review articles (see, for example, [4–7]). Quantum size effects of semiconductor nanoparticles are described in textbooks [8–10]. The size effects are also considered in articles [11, 12], the description of the influence of the size of nano-objects on their various properties is given in [13].

In addition to size, in some cases, the shape (magnetic nanocrystals) also has a great influence on the properties of particles [2]. Catalytic activity and selectivity, electrical and optical properties, and melting temperature are also highly shape dependent [14].

Metals that do not exhibit or weakly exhibit catalytic activity in the ordinary state may turn out to be active catalysts in the nanoscale state. The increase in activity is explained by charge transfer from the substrate and is more pronounced for particles with the smallest size [15–19] and those consisting of transition metal oxides [20–24]. Zeolites are often used as a matrix for stabilizing metal nanoparticles, since the particle size can be limited by the channel width [25–31].

In [32], copper oxides (Cu₂O, CuO) were deposited on the surface of SiO₂ and ZrO₂ substrates. It was shown that the values of the binding energy and the modified Auger parameter [33] for copper oxide strongly depend on the degree of dispersion of the deposited phase and the type of substrate.

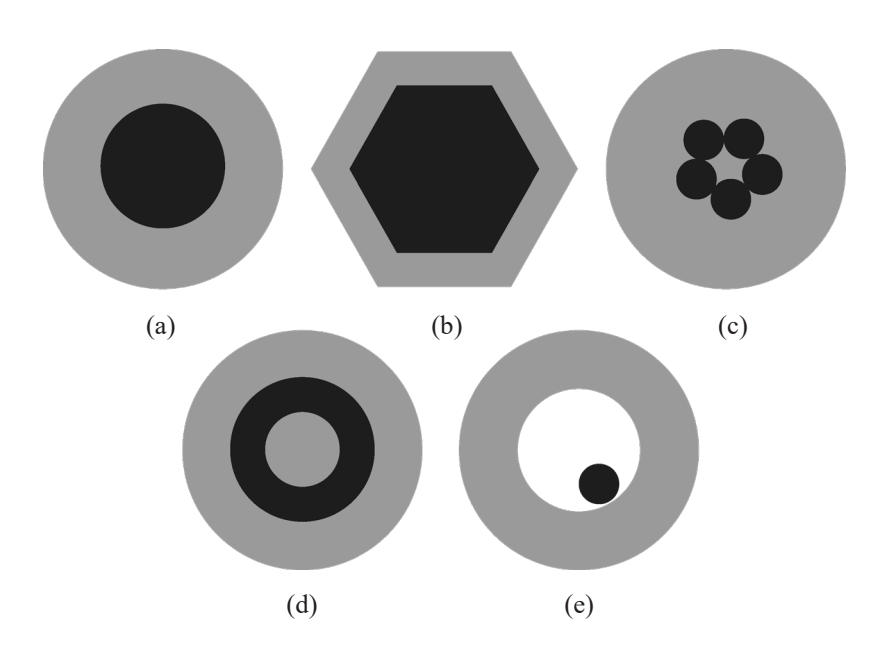


Fig. 1. Nanoparticles with a core–shell structure of various shapes: (a) spherical concentric, (b) hexagonal (hexahedral), (c) nanoparticles containing several cores covered with one shell, (d) multilayer concentric spherical nanoparticles (*nanomatryoshka*), (e) particles with a removable layer [2].

Thus, from the Wagner plots [33], it is possible to determine not only the chemical state of the metal in the deposited layer, but also the particle size distribution [34] (Fig. 2).

One of the modern methods for obtaining nanostructures in the form of thin oxide films under ultrahigh vacuum conditions followed by in situ analysis is the reduction of the surface of higher metal oxides by bombardment with inert gas ions (He $^+$, Ne $^+$, Ar $^+$) or the oxidation of the metal surface with O $_2^+$ ions. This technique was used to modify and study pressed powdered higher oxides of molybdenum and tungsten [35], tungsten oxide [36], the surface of metallic vanadium [37], niobium oxide [38], and tantalum oxide [39, 40].

A review article [2] is devoted to core–shell nanoparticles, according to which these nanoparticles are used in biomedical and pharmaceutical applications, catalysis, electronics, and are used to achieve a high quantum yield and create photonic crystals (Fig. 3). Applications are also described in [41–43]. Supramolecular systems in general, including nanoparticles, nanomaterials, and structures based on them, are described in [44].

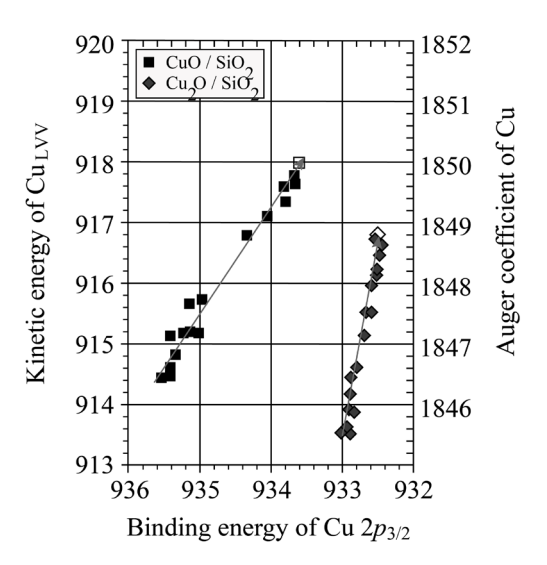


Fig. 2. Wagner plots describing the change in binding energies, kinetic energies, and modified Auger parameters for Cu $2p_{3/2}$ and Cu L_1VV copper lines. The arrow shows the increase in particle size; empty squares correspond to bulk oxides [34].

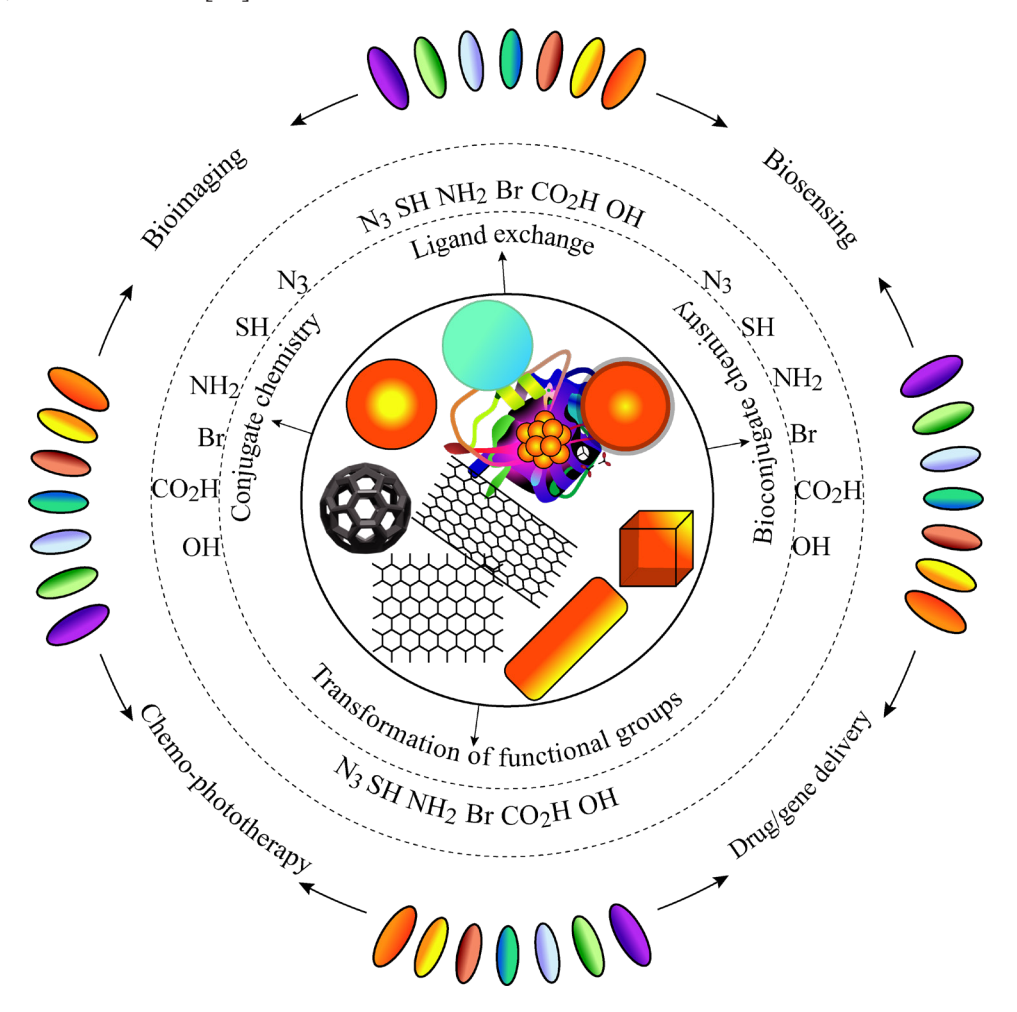


Fig. 3. Fields of application of core–shell nanoparticles [2].

Study of nanomaterial properties

Work [45] is devoted to the commercialization of nanobiotechnologies. Many of the physical and chemical parameters needed to understand the properties of objects are often unpublished and most likely not defined at all. Bureau International des Poids et Mesures, Consultative Committee for Amount of Substance: Metrology in Chemistry and Biology, and Technical Committee of the International Organization for Standardization (TC ISO 229) determined the requirements for nanomaterials in relation to the environment, health and safety, toxicology, and also approved a list of necessary physicochemical properties and parameters of nanomaterials (16 in total) related to the chemical and physical state of the surface [46].

Review [47] is devoted to the methods of studying nanoparticles and nanomaterials. Review [48] summarizes research tools and methods for studying the surface of solids and surface layers developed over the past 50 years. Publication [49] describes the determination of nanomaterials in the environment by various methods.

The papers [11, 48, 50] describe the necessary requirements for the correct analysis of nanoparticles:

- 1) in situ analysis or immediately after synthesis;
- 2) understanding the interactions (and time dependence) of particles placed in a working environment (biological, solutions, catalysis, etc.);
 - 3) the need for analysis by several methods;
- 4) development of new methods of analysis, or increasing the resolution and sensitivity of already used methods to obtain more accurate information about the structure of nanomaterials.

Since nanomaterials, like colloidal systems, are qualitatively different from the bulk substance, it can be assumed that methods previously developed for colloidal systems can be used to analyze nanomaterials. However, despite the similarity of these objects, colloidal phenomena can lead to the degradation of nanomaterials [51].

Ultra-microscopy using visible light determine the limiting particle size of the order of 200 nm (taking into account the boundaries of the visible range of 400-700 nm), and using ultraviolet—up to 100 nm. When light scattering used, the limiting determinable size of nanoparticles is 2-5 nm, which is an adequate approach for nanoparticle sols. The limitation of this method is the need to measure dilute a significant difference between and the refractive index of the dispersed phase (nanoparticles) and the dispersion medium [52]. Other methods based on the scattering of light

by particles are nephelometry and turbidimetry, suitable for estimating particle sizes in dilute sols. determine the particle size distribution, ultracentrifugation construction and the of sedimentation curves are used. To determine the surface potential of charged particles (ζ potential), of electrophoretic measurements braking electro-osmosis are carried out [52].

The method of X-ray diffraction with a particle size of less than 5 nm becomes severely limited in terms of analytical information, there is no surface sensitivity, and a sufficiently large amount of substance and time are required for analysis. Electron microscopy, X-ray diffraction, and electron diffraction are more versatile and have a resolution sufficient for studying nanomaterials [3].

The Mössbauer spectroscopy method provides information on the short-range order of the structure of matter and magnetic properties at different temperatures and external magnetic fields [52].

Transmission electron microscopy (TEM), atomic force microscopy (AFM), Brunauer–Emmett–Teller (BET) specific surface area measurements provide information on size and size distribution, particle shape, and surface properties. TEM can also determine the crystallinity of a sample. AFM determines the height distribution, location, and size of particles. If this information is lacking, the BET method is used, provided that the particles have a narrow size distribution, are spherical in shape and are not porous. An estimate of the external size (hydrodynamic diameter) of a particle of regular shape can be determined by the method of dynamic light scattering [3, 52].

Scanning electron microscopy (SEM) is used to determine the structure and size distribution of particles, but is inefficient for measuring samples consisting of complex nanoparticles (for example, with a core-shell structure), since it provides information only about the size distribution for the whole particle. Under the action of an electron beam, the surface structure changes. SEM gives inadequate results when determining the particle size less than 20 nm. The method of electron diffraction on a selected region has limitations associated with measuring the signal from a large number of crystalline particles (to determine crystallinity) and a sufficiently large fraction of amorphous nanoparticles in a crystalline matrix for their detection [52].

Electrophoretic light scattering (laser Doppler electrophoresis) is used to determine the charge on the particle surface.

Infrared spectroscopy and paramagnetic resonance spectroscopy determine the presence of adsorbed light molecules and functional groups

on the surface of particles and the degree of substitution of surface atoms. When measuring absorption and luminescence spectra in the optical region, one can determine the surface roughness, film thickness, and particle size due to the difference in the properties of nanomaterials from bulk materials [3, 52].

Thermal analysis (thermogravimetry), differential thermal analysis and differential scanning calorimetry allow you to study phase transitions in a substance, including glass transition and crystallization into various polymorphic phases. Using these methods, the characteristics (temperature, energy) of the above processes and the phase composition of the resulting nanoparticles are determined. When carrying out isothermal calorimetric titration, it is possible to determine the ability of sorption of proteins and biologically active substances [52].

are There also other methods vibrational and superconducting quantum interference device magnetometry (superconducting interferometer is supersensitive a magnetometer used to measure very weak magnetic fields), energy dispersive and X-ray absorption spectroscopy, electron energy loss spectroscopy, X-ray spectroscopy of absorption near the edge and with high resolution (fine structure) [3, 52]. Works [53-56] are devoted to modern methods of studying nanoparticles and nanomaterials, up to the determination of the structural dynamics of individual molecules in the femtosecond range.

XPS is one of the most reliable methods for determining the electronic structure and stoichiometry of solids. General information about measurements of samples by this method is given, for example, in [57]. Some deviations of the results may occur due to adsorbates present on the surface of the studied particles [58].

General conclusions about the analysis of nanoparticles

Some of the main unresolved issues in the field of nanoparticle research are the following [52, 59]:

- 1) the instability of nanomaterials and nanoparticles, which significantly increases the requirements for the influence of the analysis tool, external conditions, measurement conditions and time on the materials under study;
- 2) a significant proportion of atoms or molecules and the possible influence of surface impurities, elemental enrichment or depletion and contamination;
- 3) the need to use complementary methods to increase the significance (correctness) of the information received;

- 4) change the physical properties of in nanomaterials. for example, the mean free path of electrons or the etching rate of surface atoms by ions, associated with size and environment:
- 5) increased requirements for sample preparation for analysis.

XPS OF NANO-OBJECTS

With the development of nanotechnologies, the role of XPS as a surface analysis method has increased significantly. A feature of this method is the possibility of qualitative and quantitative chemical analysis of the surface layers of a substance—multiphase and multicomponent thin films, particles, and powders on the surface. It is possible to analyze the fine structure of the spectra and determine the charge and chemical states of the detected elements. Determination of the qualitative and quantitative composition is acceptable in depth (profiling) and on the surface (mapping).

The lateral resolution of electron spectrometers is usually a few micrometers and exceeds the size of typical nanoparticles by at least three orders of magnitude, so the area of information collection is determined by the shallow depth of analysis based on the mean free path of photoelectrons. The analytical depth is 4-10 nm for polymers, and 0.5-2.5 nm for metals and oxides. Another advantage is that XPS is a nondestructive analysis method, which allows signal accumulation from low-intensity components. The exception is polymeric and photosensitive samples, for which slight photodissociation and radiolysis are possible. The lower limit of the determined concentrations is ~0.1 at. %, which corresponds to 1–10 ng of a substance or 0.01–0.05 of a monolayer.

General provisions

XPS measurements are usually carried out under ultrahigh vacuum conditions to prevent adsorption of molecules and contamination of the surface during the measurement process. Recently, near-atmospheric pressure systems (near-ambient pressure XPS) have also been developed and used, both with synchrotron sources and conventional X-ray tubes [60, 61].

Under conditions of ultrahigh vacuum, it is possible to analyze impurities and surface defects, and at elevated pressure, it is possible to study reactions on the surface, in particular, catalysis. Many photoelectron spectrometers are combined

with *in situ* sample preparation tools such as molecular beam epitaxy, pulsed laser deposition, chemical vapor deposition, magnetron sputtering, and ion bombardment. The XPS method in relation to the study of classical objects, for example, the surface of solids, is described in detail in a number of textbooks and monographs [62–67].

Structure of the device

The main components of a modern electron XPS spectrometer (Fig. 4) are a radiation source, a device for mounting and introducing a sample, an energy analyzer, and an electron detector located in an ultrahigh vacuum chamber [68–71].

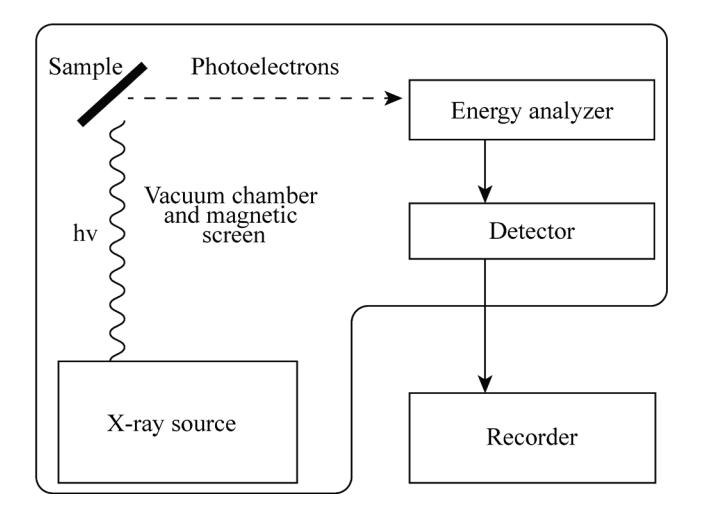


Fig. 4. Block diagram of an X-ray photoelectron spectrometer.

The radiation sources in the XPS method, as a rule, are X-ray tubes with a metal anode, which give soft characteristic X-ray radiation with an energy of the order of several keV, which makes it possible to carry out a qualitative and quantitative elemental analysis of the sample surface, determine the chemical state (oxidation state) of elements, and also investigate the electronic the structure of valence states near the Fermi level (with a rather low resolution of the SPS method is determined primarily by the bandwidth of the exciting radiation. The resolution can be increased using monochromators, which also leads to some side effects [75–79].

XPS is a method of integral analysis due to the rather large diameter of the X-ray beam. Local analysis is possible when the spectrometer is equipped with sharp-focus X-ray tubes with a beam diameter of $100-500~\mu m$.

As a detector in XPS, a secondary electron multiplier is used, which is a proportional electron counter and amplifies the signal by a factor of 10⁶–10⁷. Industrial spectrometers use channel electron multipliers or large area detectors or vidicon detectors [69, 70, 72].

To ensure a sufficient mean free path of electrons without energy dissipation and loss of analytical information, as well as to maintain surface cleanliness, ultrahigh vacuum with a pressure of 10^{-6} – 10^{-8} Pa is maintained in the spectrometer during measurements, supported by various types of pumps. The requirement for surface cleanliness imposes a limitation on the materials used in the spectrometer device.

There are a number of methods developed from classical XPS. These are valence band XPS (using gas-discharge sources), energy loss spectroscopy (on such features of the electronic structure of the sample as surface and bulk plasmons, shake-up satellites, asymmetric core lines, and splitting), multiplet photoelectron diffraction. Modification of the spectrometer design led to the appearance of photoelectron spectroscopy with angular resolution and the introduction of synchrotron and ultraviolet radiation sources [62, 68, 70, 72].

Method basics

Spectra measurement. When analyzing a sample, the survey spectrum is first measured over a wide range of binding energies. The survey spectrum consists of photoelectron and Auger lines, satellites from an X-ray source and shaking and contains a background of inelastically scattered electrons. Following that, the boundaries of photoelectron lines are determined and the spectra of individual lines are measured [70, 71] (Fig. 5).

Mathematical processing of the spectra is described in detail in the sources [80–82]. There are also some additional data tables that allow one to manually or programmatically subtract the spectrum features (X-ray satellites) associated with the non-monochromaticity of the source [75, 83].

Determining the chemical state of atoms on the surface is possible by changing the binding energy of the line with a change in the environment of the atom (chemical shift). There are a large number of works on theoretical calculations of the chemical shift and absolute binding energy, however, in practice, insufficiently accurate knowledge of the numerical parameters required for calculations leads to the need to refer the obtained experimental data to the data measured for standard samples. The rules for determining

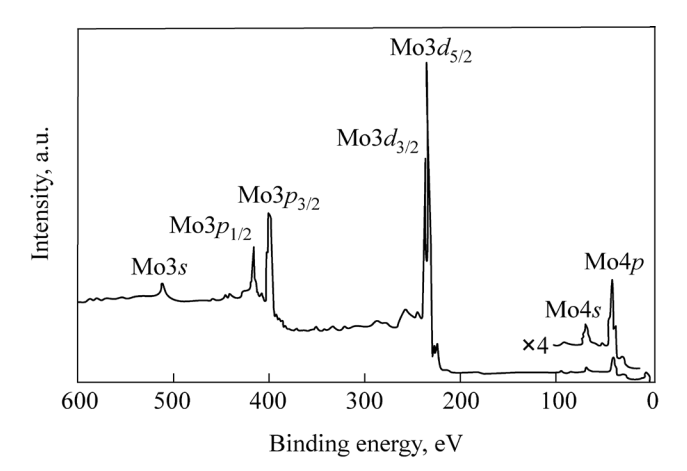


Fig. 5. X-ray photoelectron spectrum of molybdenum upon excitation by Mg K α radiation, recorded at an analyzer transmission energy of 100 eV [70, 71].

the chemical shift indicate that the chemical shift of the element line depends on the oxidation state of the element in the compound under study, which is equivalent to the electron density distribution between the atom and adiacent atoms, or the charge on the atom [70, 83]. Under conditions of electrostatic charging, which occurs when measuring poorly conducting or dielectric samples, the spectra are completely shifted to the region of high binding energies. In some cases, this effect can be minimized by irradiating the sample surface with a compensating low-energy electron beam. In other cases, for the qualitative determination of elements or chemical states. either assignment to lines with a reference binding energy (for example, Ag 3d, Au 4f, or C 1s) is used, which may not be true with differential charging, or the determination of the qualitative composition and forms of the substance by the usual or modified Auger parameters [83].

Quantitative analysis in XPS

Classical quantitative analysis via photoelectron spectra is based on the fact that line intensities are directly proportional to element concentrations and elemental sensitivity factors [68–70]. Most of the parameters of the photoemission process significantly depend on the material, their ratio is close to a constant value, so the fraction of atoms of a given type C_x in the sample can be determined by Eq. (1):

$$C_{x} = \frac{I_{x} / S_{x}}{\sum_{i} I_{i} / S_{i}},\tag{1}$$

where I_x is the line intensity, S_x is the elemental sensitivity factor. A set of elemental sensitivity factors is required for each X-ray source with a different angle between the source and the energy analyzer. The sensitivity factors for a homogeneous sample are determined as the product of the photoionization cross section of the atomic shell σ_i and the mean free path for photoelectrons of a given line λ_i [83].

A table of theoretically calculated photoionization cross sections for atomic orbitals (from lithium to uranium) was given in the reference book1. The National Institute of Standards and Metrology (NIST) maintains six databases applicable to XPS and Auger spectroscopy. These are databases on the binding energies of photoelectronic lines in XPS, on the elastic scattering cross sections of electrons, on the mean free paths of electrons in a substance, on the effective electron (in)elastic mean free paths in a substance, on modeling electronic spectra for surface analysis, and on backscattering correction Auger-spectroscopy.Critical factors for [84–87] are devoted to the evaluation of these data.

When determining atomic concentrations, the following assumptions are usually made:

- 1) in the area of analysis, the sample is homogeneous or polycrystalline (up to the information depth of measurement over the entire analyzed area);
 - 2) reflection and refraction of X-rays is negligible;
- 3) reflection and inelastic scattering of photoelectrons is small;
- 4) the probability of photoionization of core levels does not depend on the environment of atoms (low matrix effect);
- 5) the area of the X-ray beam exceeds the area of the sample.

Changes in the elemental sensitivity factors of transition metals in different compounds can be taken into account using the experimental values measured for different standard samples [83].

When the composition of the sample is inhomogeneous, calculations by Eq. (1) lead to errors. These deviations can be eliminated by taking into account additional factors affecting the peak intensities [70–73]:

- 1) measurement of elemental and complex, close in composition, standard samples under the same conditions as a sample of unknown composition;
- 2) introduction of corrections for the depth of exit and the atomic density changed in comparison with the standard (matrix correction);

¹ https://xpslibrary.com/%CF%83-sf-asf-and-rsf/. Accessed April 01, 2023.

3) modeling the spectra obtained for the assumed concentration gradients, if they are well known, and performing a multicomponent fitting, taking into account the resulting background of inelastically scattered electrons.

Ultraviolet photoelectron spectroscopy (UPS)

According to the principle of operation, UPS is similar to XPS [73, 75, 83, 88]. As radiation sources, gas-discharge lamps are used, which, depending on the pressure of the inert gas, emit lines of He I (21.2 eV) and He II (40.8 eV) or Ne I (16.9 eV) and Ne II (26.8 eV) with a very small linewidth (less than 0.02 eV). In lamps, a capillary discharge with a cold cathode occurs [88].

UPS is not a method for quantitative surface analysis, since it does not give a quantitative estimate of the atomic concentrations of elements on the surface. The lines in the region of the valence band have a large width (3–5 eV), and the intensity depends on the bonds formed by the element and differs for a number of compounds. Therefore, the shape of the valence band spectra differs for isomers and allotropic modifications, which is used to distinguish between surface compounds, for example, amorphous carbon, graphite, and highly oriented porous carbon [88].

This method makes it possible to record the spectra of states of valence electrons near the Fermi level and quasi-core levels with a low binding energy with a high energy resolution and intensity. UPS in the variant with angular resolution was intensively used in studies of the binding energy of adsorbates with the surface, and when measuring the photoelectron spectra of a smooth surface of single-crystal samples at different polar and azimuthal angles, it is possible to construct a band structure [88].

XPS with synchrotron excitation

The use of synchrotron radiation sources for excitation of photoemission offers advantages over X-ray tubes commonly used in laboratory instruments. Synchrotron **XPS** measurements can be more efficient due to the characteristics of synchrotron radiation compared to X-rays, especially with respect to nanomaterials The most important advantages high intensity and brightness, the possibility of tuning the radiation energy, high energy resolution, and low linewidth after the monochromator (depends on the radiation energy, is less than 0.1 eV for energies of the order of keV).

The concept of brightness includes illumination and angular divergence of the beam. Due to the fact that synchrotron sources have a brightness 10^9 times higher than laboratory sources and a small beam size, they are able to provide higher lateral resolution and signal-to-noise ratio. This can be especially significant when measuring spatially separated nanoparticles at low surface coverage [89].

The high energy resolution of modern electron analyzers, ultraviolet and synchrotron radiation, high angular resolution (fractions of a degree), and ultralow temperatures have made it possible to make significant progress in experimental studies of the electronic structure of the valence bands of solids. As a result of such experiments, experimental Brillouin zones, Fermi surfaces, and zone dispersion maps are obtained, which previously could only be obtained from quantum chemical calculations.

The width of the photoelectron peaks is determined by the convolution of three components: the natural linewidth, the resolution of the electronic analyzer of the spectrometer, and the width of the exciting radiation. The natural width of the lines depends on the atomic orbital from which the photoemission occurs and is usually in the range of 0.13–0.70 eV (for Ag $3d_{5/2}$ it is 0.33 eV). In instruments with synchrotron sources and X-ray tubes, approximately the same electron analyzers are used, and the difference in resolution is due to the width of the X-ray line. The linewidth of synchrotron radiation is a function of the radiation energy and monochromatization and is much lower than that of X-ray tubes. This makes it possible to track small (smaller) chemical shifts [90].

Currently, there are new methods of XPS with synchrotron radiation or free electron lasers at high pressure. One of the promising and fairly new areas is the study of heterogeneous processes solid-liquid interface, which includes the preparation of thin liquid films and XPS measurements at high (atmospheric) pressure (Fig. 6) [91-93]. Chemical shift measurements can provide high chemical selectivity for both molecules on the surface and the substrate. In XPS experiments with X-ray quanta with an energy of ~1 keV, it is possible to create pressures in the range of several Torr and even higher due to the generation of photoelectrons with a high kinetic energy and a long mean free path [91].

In [93], the interface between metallic nickel and an aqueous solution of KOH was studied using synchrotron radiation sources, differential pumping systems between the sample and an electron analyzer.

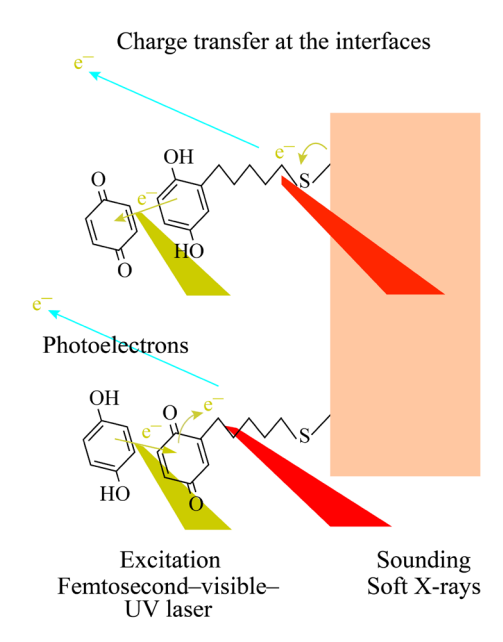


Fig. 6. Investigation of heterogeneous processes at the solid–liquid interface using XPS [91].

Excitation was carried out by radiation converted into a standing wave, which was achieved by using a multilayer Si/Mo mirror as a substrate and increased the depth resolution [93]. Previously, the same team of researchers carried out work to determine the surface layer of α-hematite (Fe₂O₂) adjoining a solution containing high concentrations of NaOH and CsOH [91]. The measurements were carried out at elevated pressure, using a multilayer substrate that provides the formation of a standing wave (ambient pressure XPS (AP XPS); standing wave ambient pressure photoelectron spectroscopy). Using XPS with angular resolution, it was determined that when moving away from the surface of hematite as a solid, there is a mixed hydrated layer with adsorbed NaOH, then a layer of NaOH and CsOH adsorbate, and then a layer of hydrocarbon contamination. Thus, the experimental data are consistent with the theoretical models. As another example of the use of the AP XPS method, one can cite the work [94], nanoparticles consisting where core-shell strontium/calcium fluoride in ethylene glycol were studied.

Freezing is used to measure biological samples or thin liquid films on a surface in addition to measurements at elevated pressure. The study of electrocatalysts for fuel cells using XPS is described in review [95]. From the simulation of water adsorption on the Pt (111) surface, it followed that a thin ice film is bound to the metal surface by metal—oxygen and metal—hydroxyl bonds. Also in the review, the structure of iodine adsorbate on the

surface of a gold single crystal was studied with a change in the voltage between the surface and the solution, which is of interest from the point of view of the oxidation/reduction potential of the iodide—ion/iodine pair associated with oxidative desorption and reductive deposition on the surface. Similar results were obtained for Pt (111) and Pt (111) surfaces with 0.5 Ru, Ru (0001) monolayers.

In the same work, a linear correlation was found between the adsorbate chemical shift and the adsorption energy of ultrathin metal films and molecules. Further, for real fuel cells consisting of platinum on a carbon carrier, the relationship between the oxidation state and the chemical shift and the spin-orbit splitting, which are different for oxide and metallic platinum, was determined. For catalyst particles consisting of an alloy of various metals (Pt/Ni, Pt/Ru, Pt/Ru/Ni), the dependence of the binding energy of platinum lines and the rate of methanol oxidation were determined. Other metals were present in the particles in the oxidized form (Ni(OH)₂ and Ru/RuO₂/RuO₃) and acted as oxygen donors in this process [95].

It was shown in [96] that the binding energy of the surface of an oxide nanoparticle in solution is related to the surface potential. This result was obtained by measuring a microjet containing silicon oxide nanoparticles. On the surface of oxides, due to interaction with hydroxyl groups in aqueous solutions, a charge is formed, which depends on the composition of the oxide, pH of the solution, its composition, concentration of components, particle size, and the electric field determines many physical and chemical properties of the particles.

The acidity and basicity of the surface groups can be determined from the change in the binding energy of the element. In [97], the polymers were sorted by increasing Lewis basicity with increasing sodium sorbed on the surface of the film. In [98], a linear relationship was found between the difference between the binding energies of the Sb $3d_{5/2}$ and Cl 2p lines and the basicity for rapidly frozen solutions of SbCl₅ with various Lewis bases in dichloroethane. The form of the linear relationship between the chemical shift of the O 1s line in metal oxides Mg, Al, Si, the Fermi level potential, and the isoelectric point was determined. When the list of oxides was extended with oxides of zinc, copper, nickel, titanium, and iron, a linear dependence of the difference in binding energies (the sum of chemical shifts) of metal and oxygen lines on the potential of the isoelectric point and the potential of the Fermi level was found [97, 98].

Another measurement option implemented at elevated pressure with synchrotron radiation is the measurement of the spectrum of a gas jet

without electrical contact with the substrate and the spectrometer holder. In [99], the flow of an aerosol of nanoparticles passing through rather narrow guides (nozzles) was measured. The short mean free path of electrons in Si nanoparticles coated with SiO_2 and the sufficiently large particle size ($d=14\pm2$ nm) made it possible to neglect the elastic scattering of photoelectrons, the shift in binding energies due to quantum size effects (manifested at d<4 nm), and charging.

Layered structures

determine the concentration profile of elements in depth, etching of the sample surface with an ion beam, for example, with Ar+, O2+ ions [100, 101]), ion sputtering with C_{60} clusters with a low destructive power for organic materials [102–104], profiling by a beam of ionized water clusters [105] followed by measurement by nondestructive methods of surface analysis, methods of surface ion probing (Rutherford backscattering spectroscopy, secondary ion mass spectrometry, glow discharge atomic emission spectroscopy) [106], X-ray microanalysis with an electron probe combined with calculations by the Monte Carlo [107]. In order to determine the depth profile of elements, XPS is used in XPS versions with resolution in terms of the analysis angle [108] and analysis of the shape of peaks and background [109–114].

To determine the qualitative composition in a surface layer with a thickness of more than 5–10 nm, the most applicable method is ion sputtering. This procedure has its drawbacks, such as preferential sputtering of atoms of one kind, atomic mixing and radiation-stimulated diffusion, which limits the final depth resolution. In some cases, elements are reduced to lower oxidation states.

Information depth

The depth of penetration of X-rays into the sample is much greater than the emission depth of photoelectrons. The intensity of the photoelectron beam from depth d decreases exponentially with increasing depth, according to Eq. (2) [86, 115]:

$$I = I_{\infty} \exp\left(-\frac{d}{\lambda \cos \theta}\right),\tag{2}$$

where λ is the electron mean free path, I_{∞} is the photoemission intensity of an infinitely thick layer, and θ is the photoemission angle relative to the surface normal.

According to this equation (when integrated over the ratio d/λ), more than 95% of the photoemission comes from a surface layer with a thickness of $3\lambda\cos\theta$. The corresponding thickness is called the depth of analysis (Fig. 7).

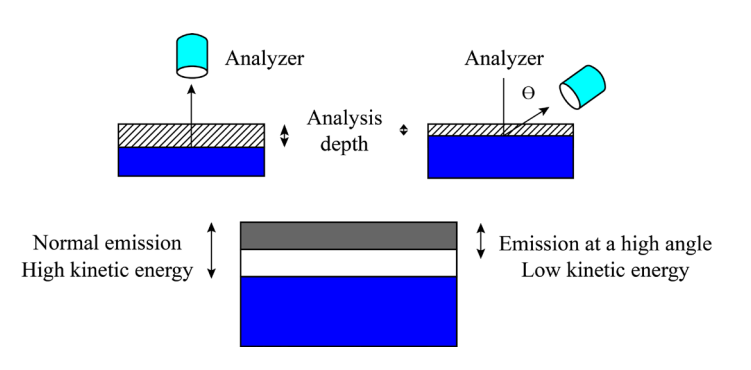


Fig. 7. Dependence of the analysis depth (information depth) on the detection angle and kinetic energy of photoelectrons [86].

To estimate the contribution of elastic and inelastic scattering of electrons in a material, two concepts are introduced into the intensity of photoelectron lines: inelastic the mean path (λ) and the effective attenuation length [83]. The first term assumes that photoelectrons can lose energy only due to inelastic collisions, while the second term also takes into account elastic interactions, so this parameter depends on the detection angle.

Information depth is the maximum depth in the normal direction to the surface from which useful information can be obtained. It is usually given as the thickness from which a given percentage of the signal (95% or 99%) comes out and can be determined from the depth distribution function of the element, or, in general, from the mean free path of the photoelectron in the selected sample [83].

Multilayered structures

Measurements of signal intensities and determination of theoretical thicknesses for flat surfaces covered with several flat layers are described in [115]. As an example, equations are given for the intensities of two consecutive layers and a substrate [116]: outer layer (3), second layer (4), and substrate (5):

$$I_{S_1} = I_{\infty}(i) \left[1 - \exp\left(-\frac{d_i}{-\lambda_{S_1}(i)\cos\theta}\right) \right], \tag{3}$$

$$\begin{split} I_{\mathrm{S}_2} &= I_{\infty}(j) \times \\ &\times \left[1 - \exp \left(-\frac{d_2}{-\lambda_{\mathrm{S}_2}(j) \cos \theta} \right) \right] \exp \left(-\frac{d_1}{-\lambda_{\mathrm{S}_1}(j) \cos \theta} \right), \end{split} \tag{4}$$

$$I_{\rm B}(k) = I_{\infty}(k) \exp\left(-\frac{d_1}{\lambda_{\rm S_1}(k)\cos\theta}\right) \exp\left(-\frac{d_2}{\lambda_{\rm S_2}(k)\cos\theta}\right), \quad (5)$$

In the above Eqs. (3)–(5), $I_{\rm B}$, $I_{\rm S1}$, $I_{\rm S2}$ are the intensities of photoelectrons from the substrate, upper and lower layers, respectively, $d_{\rm 1}$ and $d_{\rm 2}$ are the thicknesses of the outer and second layers, $\lambda_{\rm S1}$ and $\lambda_{\rm S2}(i,\ j,\ k)$ are the average the mean free path of electrons with the energies corresponding to lines i,j,k,θ is the angle of the analyzer with respect to the normal of the sample surface.

However, usually the exact values of the signal intensities from the bulk materials that make up the layers are not known. Then, for the case of a two-layer sample, the equations for the photoemission intensity of a thin film on a substrate can be written as:

$$I_{S_1}(i) = I_{\infty}(i) \left[1 - \exp\left(-\frac{d_1}{\lambda_{S_1}(i)\cos\theta}\right) \right],\tag{6}$$

$$I_{\rm B}(k) = I_{\infty}(k) \exp\left(-\frac{d_1}{\lambda_{\rm S_1}(k)\cos\theta}\right). \tag{7}$$

The layer thickness d_1 is found by Eq. (8):

$$d_i = \lambda_{S_i}(i) \ln \left(\frac{I_{\infty}(k)I_{S_i}(i)}{I_{\infty}(i)I_{S_i}(k)} - 1 \right). \tag{8}$$

If it is difficult to theoretically predict the exact value of the signal intensity from a bulk material, then the ratio of such photoemission intensities of two different substances is found by sequentially measuring the intensity of signals from two pure materials in the same installation. The above Eq. (8) also does not take into account differences in the mean free paths, which is true for elements with a compound film with similar binding energies (and photoelectron kinetic energies), for example, a metal with an oxide film.

One of the first proposed for the analysis of thin multilayer films was the Hill equation [117]. It was used to determine the thickness of the oxide film on the silicon surface. The film thickness can be calculated by Eq. (9):

$$d_1 = \lambda_{SiO_2} \cos(\theta) \ln \left(1 + \frac{\left(I_{SiO_2} / R_{SiO_2} \right)}{I_{Si}} \right). \tag{9}$$

In the presence of a large number of layers, the corresponding multipliers are introduced, as shown in the previous equations. For example, for an oxide film on a silicon surface, consisting of intermediate oxides and dioxide, Eqs. (10)–(13) were used [118]:

$$d_{\text{SiO}_{2}} = L_{\text{SiO}_{2}} \cos(\theta) \ln \left[1 + \frac{\left(\frac{I_{\text{SiO}_{2}}}{R_{\text{SiO}_{2}}} \right)}{\left(\frac{I_{\text{SiO}_{2}}}{R_{\text{Si}_{2}O_{3}}} + \frac{I_{\text{SiO}}}{R_{\text{Si}_{2}O}} + I_{\text{Si}}} \right)} \right], \quad (10)$$

$$d_{\text{Si}_2\text{O}_3} = L_{\text{Si}_2\text{O}_3} \cos(\theta) \ln \left[1 + \left(\frac{I_{\text{Si}_2\text{O}_3}}{R_{\text{Si}_2\text{O}_3} I_{\text{Si}}} \right) \right], \tag{11}$$

$$d_{\rm SiO} = L_{\rm SiO} \cos(\theta) \ln \left[1 + \left(\frac{I_{\rm SiO}}{R_{\rm SiO} I_{\rm Si}} \right) \right], \tag{12}$$

$$d_{\text{Si}_2\text{O}} = L_{\text{Si}_2\text{O}}\cos(\theta)\ln\left[1 + \left(\frac{I_{\text{Si}_2\text{O}}}{R_{\text{Si}_2\text{O}}I_{\text{Si}}}\right)\right]. \tag{13}$$

In Eqs. (10)–(13), for partial thicknesses of the oxide components $d_{\mathrm{Si_2O_x}}$, the electron decay length is denoted as $L_{\mathrm{Si_2O_x}}$, and R is the ratio of the photoemission intensities of the oxide and oxide forms, $R_0 = 0.9329$ is the ratio for $\mathrm{SiO_2}$ and Si , which can be calculated from the atomic densities, attenuation length and stoichiometry (14):

$$R_{\text{Si,O}_x} = 1 + 0.25 \times (R_0 - 1). \tag{14}$$

Similarly, the concentrations of elements are calculated in structures that are a non-continuous homogeneous layer on the surface or in the depth of the sample, introducing the ratio of the layer area to the analyzed area into the calculations [119].

There is also a method [80–82, 120–122] based on the analysis of the background shape². With a deeper occurrence of the component in the sample, the background signal increases in the region with a higher binding energy, and vice versa. For most metals, alloys, and oxides, the energy distribution of photoelectrons and the observed spectrum, after correction for the spectrometer transmission function, are expressed in terms of the two-parameter universal cross section according to equation (15):

$$F(E) = J(E) - \int_{E}^{\infty} \frac{B(E' - E)}{\left\{C + (E' - E)^{2}\right\}^{2}} J(E') dE', \tag{15}$$

where F(E) is the signal intensity at a point with energy E without electron scattering (primary excitation spectrum), J(E) is the experimentally photoelectron Emeasured spectrum, photoelectron binding energy, E'is also photoelectron binding energy, but used not determine the signal at a particular point, but as a variable for integration; B = 2866 eV and $C = 1643 \text{ eV}^2$. For solids, such as light metals (for example, Al and Si), a simple two-parameter equation does not describe plasmon energy losses, for which a three-parameter Eq. (16) is introduced:

$$F(E) = J(E) - \int_{E}^{\infty} \frac{B(E' - E)}{\left\{C - (E' - E)^{2}\right\}^{2} + D(E' - E)^{2}} J(E') dE'.$$
(16)

For thin layered structures, two-parameter Eq. (15) is written as Eq. (17):

$$F(E) = J(E) - B_1 \int_{E}^{\infty} \frac{(E' - E)}{\{1643 + (E' - E)^2\}^2} J(E') dE'. \quad (17)$$

In this equation, the parameter B_1 is chosen so that the intensity of the background line exactly coincides with the intensity of the experimental spectrum J(E) at a distance of 30 eV from the peak maximum (thus, the background is subtracted in the range up to 30 eV towards higher binding energies beyond the peak position). Then the depth distribution of atoms can be estimated from the parameter B1 and the peak area A_p from Table 1. The attenuation depth L is determined from Eq. (18):

$$L = \frac{B_1}{B_0 - B_1} \lambda \cos \theta. \tag{18}$$

Here $B_0 = 3000 \text{ eV}^2$, λ is the mean free path of photoelectrons, and θ is the photoemission angle with respect to the surface normal. After determining L, the depth distribution of atoms can be estimated from Table 2.

As an example of the use of Eqs. (3)–(5) or (6)–(8), the thickness of thin oxide films on transition metals may be determined [123–125]. The thickness of the oxide–hydroxide film on the surface of an alloy of niobium and zirconium (consisting of water, hydroxide, oxide, and metal layers) was determined in the same way during oxidation under atmospheric conditions with high humidity [126]. If the film consists of several oxide and hydroxide forms or contains water,

Table 1. Rules for estimating the depth distribution from the A_p/B_1 ratio, where B_1 is the adjusted parameter for the background line at a point 30 eV away from the maximum, and A_p is the area of the photoelectron peak

A_{p}/B_{1}	Depth distribution
≈25 eV	Uniform
>30 eV	Mostly on the surface
<20 eV	Predominantly deep in the sample

² http://www.quases.com/. Accessed April 01, 2023.

		-
	L	Depth distribution
	$-6\lambda_{i} < L < 6\lambda_{i}$	Uniform
	$-3\lambda_i < L < 0$	Mostly on the surface
	$0 < L < 3\lambda_i$	Predominantly deep in the sample

Table 2. Depth distribution estimation rules based on the attenuation depth L

the calculation of the thickness of ultrathin films is carried out for all elements that make up the films. In [126], the fine structure of the spectra of the Zr 3d, Nb 3d, and O 1s lines was studied (Figs. 8–10).

Classification of samples in XPS with angular resolution

The thickness profiling of samples is possible not only with a change in the X-ray energy, but also with a change in the photoelectron detection angle. Angle-resolved XPS (AR XPS), based on the dependence of the peak intensity on the detection angle, has been used for more than 35 years as a non-destructive method for analyzing the surface structure. The accuracy, limitations, and problems of the method are presented in [127] from a theoretical point of view, and in [118] from a practical point of view, but only for a system consisting of a thin SiO_2 film on Si .

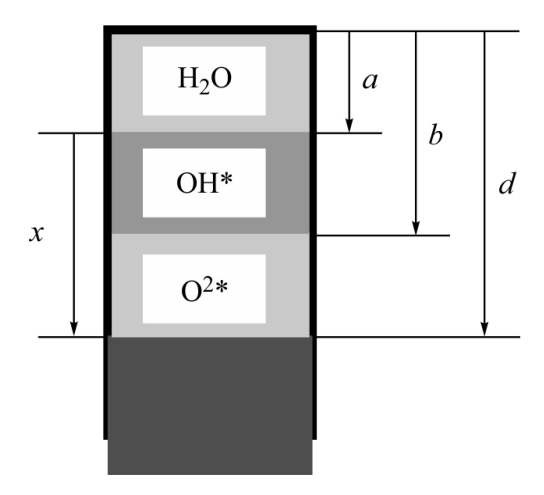
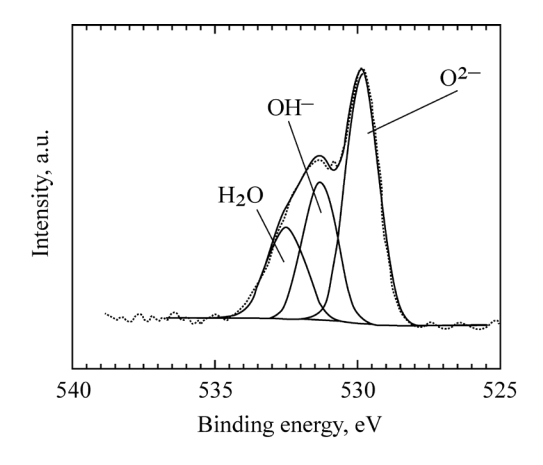
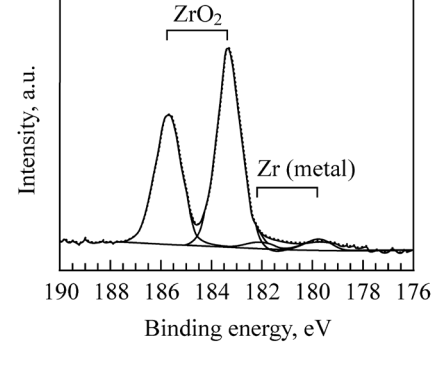


Fig. 8. Layered structure of a thin mixed oxide-hydroxide film on the surface of zirconium and niobium. The letters denote: *a* is the thickness of the water film, *b* is the total thickness of the hydroxide and water films, *d* is the total thickness of the coating layer of water, hydroxide, and oxide films, *x* is the thickness of the film corresponding to the oxidized metal [126].





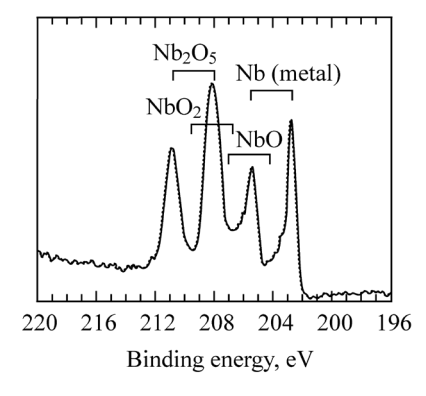


Fig. 9. Fine structure of the spectrum of the O 1s oxygen line with indicated peaks corresponding to oxygen in the composition of water, metal hydroxide, and oxide [126].

Fig. 10. Fine structure of the spectra of zirconium and niobium lines with indicated peaks corresponding to the metal and various oxide forms [126].

Angular-resolved XPS is based on quantitative expression (19) relating the measured photoelectron intensity $I_{\lambda}(\theta)$ to the concentration profile c(z):

$$I_{A}(\theta) = I_{0} \int_{0}^{\infty} CF(z, \theta) f(z) \exp\left(-\frac{z}{\lambda \cos \theta}\right) dz \cong$$

$$\cong I_{0} \int_{0}^{\infty} f(z) \exp\left(-\frac{z}{\lambda \cos \theta}\right) dz.$$
(19)

In this expression, θ is the detection angle with respect to the normal, z is the depth of the layer from which photoemission occurs, $CF(z, \theta)$ is the factor responsible for elastic scattering effects, and f(z) is the concentration profile of the selected element. With this designation, the signal intensity from a standard sample of known composition will be equal to $I_0\lambda\cos\theta$ at f(z) = 1.

According to equation (19), with a sufficient number of measurements, it is possible to obtain f(z) by inverse transformation, but this procedure is extremely sensitive to errors in determining the area (intensity) of the peaks [127]. A serious limitation of the method is the need for very flat sample surfaces (to eliminate shading), which means the absence or special consideration of nanostructures on the surface [60, 127, 128] and measurements in directions that do not coincide with high symmetry directions (axes).

Depending on the complexity of the analysis, samples in XPS with angular resolution are divided into the following groups.

- 1. Simple samples. They usually consist of an element coated with an oxide film. To determine the thicknesses, the Hill equation [117] is used, which is the most accurate and simplest approach for quantifying the thickness of layers in XPS with angular resolution. If there is a significant difference between the energies of electrons from the coating layer and the substrate, the Thickogram method is used to determine the thicknesses [129].
- 2. Fairly simple samples. Multilayer samples for which a step-by-step method of thickness estimation is used [70–72]. Later, a layering method was proposed that estimates the average thickness and amount of substance in each layer. On such constructions it was impossible to determine the depth scale. Therefore, nowadays the focus is more on diffuse profiles, and not on those with clear boundaries, as was customary in the layering method. The relative amounts of one form or another of a substance or element are built on the depth scale [70, 72].

3. Complicated samples. Samples for which the preliminary concentration profile is unknown. For their analysis, the methods and software described in [130, 131] are used.

Concentration profile analysis

The uncertainty in calculating the concentration profile of elements in AR XPS is expressed by the depth resolution Δz . By definition, this is the thickness of the sample layer in which the calculated component concentration changes from 16% to 84% (assuming that the real sample has a sharp boundary). This choice allows us to define Δz as twice the standard deviation 2σ ; when choosing 10% and 90% concentration, $\Delta z = 2.36\sigma$. If the depth profile function has an exponential rather than a Gaussian form, as in the case of electron depth attenuation, $\Delta z (16-84\%) = 1.67\sigma$.

When analyzing the concentration profile by the AR XPS method, proceed as follows. First, the detector signal is corrected for the analyzer transmission function, since the detection efficiency depends on the kinetic energies of the electrons. Further, the cascade of secondary electrons from the high-energy side of the peak is adjusted to a straight line and such a background is subtracted. After that, a model spectrum is generated, taking into account the depth distribution of the components. Finally, the model spectrum is corrected for the experiment, which can be performed using the QUASES-Generate software [130, 131]. This software allows you to build spectra of a wide variety of concentration profiles, including buried and non-immersed layers (Frank-Van der Merwe), islands (Volmer-Weber), islands on the layer surface (Stranski-Krastanov), and exponential profile. The paper [132] gives an example of a program developed for interpreting data obtained from measurements in AR XPS.

Direct formulas and transformations are used to go from theoretical concentration profiles and phase parameters to specific line signal intensities (spectrum modeling), while inverse transformations are required to obtain concentration profiles. Inverse Laplace transforms are sensitive to fluctuations in the input intensity ratios and spectrum noise. Detailed calculations of the concentration profile, formulas, and errors in the calculations are given in [133].

To calculate the profiles of ultrathin films with sharp boundaries, the method of least entropy is successfully used. The uncertainty inherent in AR XPS is reduced as follows: each component is defined as a continuous layer (square profile)

defined by three parameters (depth, thickness, and density), which fits within the limitation of parameters that can be extracted to three per element [134, 135].

The analysis is carried out separately for each component. The composition of the film is determined empirically, only after matching the individual components in depth. The composition is calculated from the ratio of concentrations, without reference to stoichiometric coefficients, which makes it possible to evaluate the changes that occur during sample preparation. The method makes it possible to take into account discrepancies, and with a smaller discrepancy than when using inverse transformations [136]. The above formulas and calculations are limitedly applicable, since real samples can have not only a rough surface, but an inhomogeneous coating planar (two-dimensional) inhomogeneities of the composition.

Conclusions on data processing by the AR XPS method

Based on the results of the conference on AR XPS [136], the following main conclusions were made.

First, for homogeneous films, the relative error in determining the thickness depends on the calibration of the instrument, while for inhomogeneous films, deviations are possible depending on the specifics of the distribution of components. Different thickness ranges require their own calibration by changing the effective mean free path of electrons.

Second, for thin films of unknown composition, it is difficult to switch from a qualitative dimensionless profile to a quantitative depth distribution, and for certain and limited systems, the use of AR XPS and intensity modeling leads to depth distributions that are close to real, without an exact match.

The information obtained by the AR XPS method is limited to three parameters per substance. Determination errors are the sum of limited depth resolution and unknown or variable composition of the sample, and the depth resolution $\Delta z/z$ exceeds 0.8 [136].

Small structures with a size on the order of the attenuation lengths of the radiation of characteristic electrons (or the mean free path) can be well described as smooth homogeneous layers, which mainly depends not on the structure, but on the size of the elements.

Including elastic scattering of electrons in calculations, both for modeling and for calculating experimental data, can increase the amount of structural information due to the use of photoemission angles exceeding 65°.

Further development of precise quantitative determination in AR XPS requires the development of a theory of the angular and energy distribution of photoelectrons and their exit from a solid body, including elastic scattering, which is theoretically well described, inelastic scattering that occurs in the volume of a solid body (bulk excitations), and surface excitations that occur when crossing the solid–vacuum surface [136].

Ion etch profiling

The possibilities of non-destructive layer-by-layer depth analysis in the XPS method are limited by the use of angular resolution and variation of the excitation radiation energies. The concentration profile of the components over the depth of the sample can be determined by the XPS method in the destructive variant with ion etching. A number of processes occur on the surface that change the qualitative and quantitative composition of the sample: atomic mixing in cascades of ion collisions, leading to implantation of recoil atoms, distortions of the crystal lattice during collisions, and the formation of defects (vacancies, substitutions, and agglomerates). Irradiation with ions of inert gases leads to insignificant changes, since it causes distortion of the sample only due to knocking out, displacement of atoms and selective sputtering.

Irradiation with ions of reactive gases, such as oxygen, leads to a significant change in the chemical composition and density of the sample due to the formation of new compounds. When a surface is irradiated with high energy ions, thermally activated diffusion and segregation occur [70–72].

To optimize the ion etching process, the pressure in the analysis chamber and the preparation chamber is kept as low as possible (10⁻⁸ Pa and below) to prevent possible contamination by sputtered atoms after etching. The area of analysis must be smaller than the spray area and be in its center. To improve depth resolution and eliminate the effect of photoemission on the sample, lines with low photoelectron kinetic energy (high binding energy) should be measured. The ion energy should not exceed 1 keV at high ion masses (heavy inert gases or cluster sources), and the ion source should produce a raster (point) beam [71, 72].

For smooth samples, etching with a large deviation from the normal (>60°) can be used; for rough samples—close to normal. The ion beam must contain a minimum amount of impurities and neutral atoms and must fall into the same region from several positions. This is possible when using multiple sources or when rotating the sample. In general, the sample to be etched should have a

smooth surface, an amorphous, non-crystalline structure, consist of a single phase and elements with close sputtering yields, have good thermal and electrical conductivity, and have low counter diffusion and Gibbs segregation [137]. Atoms removed from the surface can then be analyzed by secondary ion mass spectrometry.

Features of the XPS spectra of complex objects

The size, shape and location of nanoparticles affect the experimental data obtained from XPS, causing a change in the binding energies of the peaks and Auger parameter values, the absolute and relative intensities of the peaks of various elements excited by X-rays at different energies or at different angles to the sample [50, 59].

In particular, for nanoparticles of noble metals of group VIII on SiO₂ and Al₂O₃ substrates, a positive shift in binding energies was shown compared to bulk metal samples [138].

The formation of a photo-hole as a result of photoemission affects all surrounding electrons and leads to a change in the binding energy and kinetic energy of the electron [139, 140]. The initial state contribution reflects changes in the charge density on the atom due to the chemical and geometric environment. The final state contribution arises from differences in the screening of core holes that appear during photoemission. Photoemission can lead to several types of end states. The shielding efficiency of core holes depends on a certain element (intraatomic shielding), on the environment (atom coordination number), and on the interaction with the substrate (interatomic shielding).

In the case of nanoparticles, strong electronic interaction with the substrate can make a significant contribution to interatomic screening [141]. The binding energy shift for nanoparticles on a substrate can also be contributed, to a lesser extent, by the effects of the initial state. This is charge transfer between particles and the substrate and hybridization of electronic states in them.

According to the Koopmans theorem, for a molecule with a filled shell, the binding energy of an electron in the state (orbital) i is equal to the orbital energy of this state with the opposite sign. This theorem makes it possible to identify the calculated energies of orbitals with ionization potentials, but it does not take into account electronic relaxation.

Intramolecular relaxation consists in the rearrangement of the remaining surrounding electrons relative to the photo-hole, leads to a decrease in energy and occurs when the molecules

of a substance are hemisorbed on the surface, and their energy levels are shifted compared to a free gas or liquid. This leads to a change in the binding of the electron to the core (the effect of the initial state) and relaxation or polarization screening (the effect of the final state).

The authors of [142] indicate the following mechanisms for changing chemical shifts due to the effects of the initial state:

- 1) interatomic charge transfers during the interaction of a metal with an oxide (deposited layer or clusters with a substrate), which was observed during the oxidation of transition metals on oxides, with the appearance of chemical shifts of more than 1.5 eV;
- 2) the appearance of an electric field from the effective charges of the substrate or metal layer (charging on non-conductive substrates) and the influence of the electric field of the charge of the interface;
- 3) chemical shifts of the core levels of surface atoms, which include a contribution from atoms with a reduced coordination number and are caused by the rehybridization of valence levels—intraatomic charge transfer. Usually, these are small negative shifts up to -0.3 eV.

The effects of the final state, as indicated above, affect the screening of core holes after photoemission and depend on the environment of the atom. In the case of dominance of the final state effects, the shift of the binding energy is inversely proportional to the cluster size. Figure 11 shows the dependence of the binding energy on the cluster size [142].

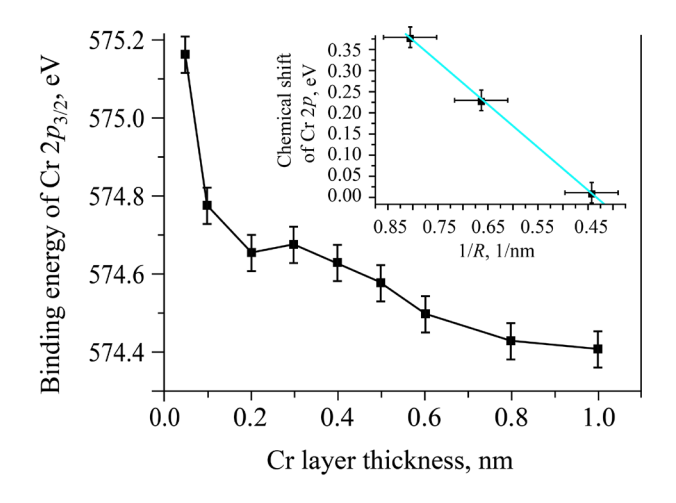


Fig. 11. Binding energy of the Cr $2p_{3/2}$ core level as a function of the thickness of the Cr layer on the SrTiO₃ (100) substrate. The inset shows the dependence of the chemical shift on the reciprocal radius of Cr clusters on the same substrate [142].

The initial and final state contributions can be distinguished by using the Auger parameter. The concept of the Auger parameter is based on the following assumptions:

- 1) for the same element in the same compound and sample, there is a fixed difference between the energies of two lines (Auger and photoelectron);
- 2) corrections for the charge shift of lines when measuring individual lines are insignificant, since they are not used in estimating the Auger parameter;
- 3) work function corrections also do not affect the value of the Auger parameter, and the vacuum energy level can be correlated with the Fermi level.

Measurement of the Auger parameter can be one of the few possible ways to identify the element and its form in the sample in the presence of a static charge on semiconductor materials and dielectrics, since it is difficult to determine the vacuum energy level in them. The Auger parameter α (20) is introduced as the difference between the kinetic energies of the two main Auger and photoelectron peaks measured on the same spectrum. The coincidence of one of the involved levels of the Auger transition with the level of photoelectron emission is not mandatory:

$$\alpha = E_{kin}(C'C''C''') - E_{kin}(C). \tag{20}$$

In Eq. (20), α is the Auger parameter, C', C'', C''' are the levels between which the Auger transition occurs, C is the level from which photoemission occurs, $E_{\rm kin}$ is the kinetic energy of the photoelectron.

Since, in the case of choosing different levels, the value of the Auger parameter could be negative, the term modified Auger parameter, α' , (Eq. (21)) was introduced, corresponding to the sum of the Auger parameter α and the photon energy hv, or the binding energy $E_{\rm b}$ and the kinetic energy $E_{\rm kin}$ of the Auger electron:

$$\alpha' = \alpha + hv = E_{kin}(C'C''C'') + E_b(C).$$
 (21)

A detailed description of the theory with examples of how the Auger parameter changes with the chemical state of matter is given in review [139]. The paper [140] gives examples of studying samples of various compositions: alloys,

modified silicon surfaces, oxides, mixed oxides, thin films, glass, metal clusters, oxide systems on substrates, interfaces between metal and organic matter, free molecules, and liquid solutions.

Calculation of signal intensities from spherical particles

For the first time, the significance of the was realized in surface structure the heterogeneous catalysts. which characterized as a powder consisting of core-shell nanoparticles. One of the reviews considering the quantitative analysis of rough surfaces [143] gives the historical development of quantitative analysis and includes formulas for correcting volumetric sensitivity factors, formulas for various layers on the surface, including continuous, carbon contamination and spherical particles, as well as formulas describing shape distortion. peak in the presence of covering layers.

For core-shell nanoparticles, several models have been developed that are applicable to powder samples. Most of these models make the following assumptions [144]:

- 1) for powders, an approximation of a simple sphere or even a hemisphere is given, introducing a simplification that the signal intensity from randomly located particles in the powder is equivalent to the signal intensity from a single particle;
- 2) elastic scattering of photoelectrons in a solid is neglected;
- 3) the relative mean free paths for a given photoelectron line are the same in the core and shell.

The simple sphere approximation implies that the angular distribution of photoelectrons in powders is isotropic. The other two assumptions were made in [144] and were consistent with experiments for functionalized gold nanoparticles. Divergences in the dependence of the intensity of photoemission of the particle core as a function of radius were observed only for particle sizes less than the mean free path, when the XPS method no longer becomes surface-sensitive, but volume-sensitive (Fig. 12).

Thus, the authors of the paper argue that the model of a single sphere for a powder sample is valid without any special refinements due to the random distribution of particles over the substrate and the absence of layer periodicity [144].

Attempts to quantify the photoemission intensity of spherical particles and flat shells on them were made in a number of works, for example, in one of the early detailed studies [145].

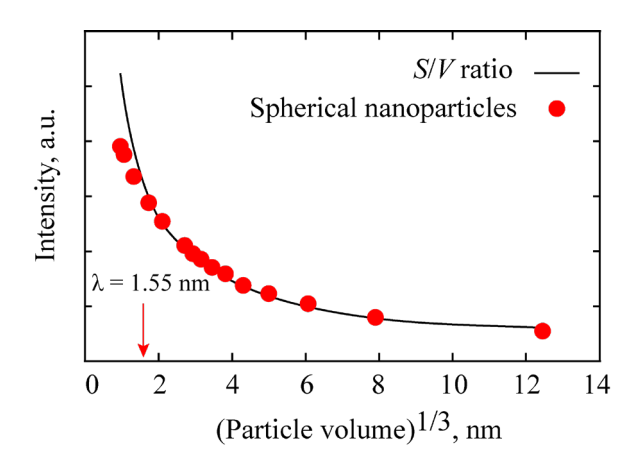


Fig. 12. Dependence of the Au $4f_{7/2}$ line intensity as a function of the particle radius. (The solid line shows the volume-to-surface ratio S/V = 3/R for a sphere. The vertical arrow indicates the mean free path of the photoelectrons in this line.)

The application of the theory described above for finding the thickness of thin films to spherical layers covering particles leads to an overestimation of the shell thickness [116, 146]. An approach to solve this problem introduces the effective layer thickness, deff, which denotes the film thickness determined by the electron analyzer. For planar thin layers, this thickness is constant in all regions of the sample; for spherical particles, it varies.

For uncoated spherical clusters, the photoemission intensity can be calculated from Eq. (22) [115]:

$$S = \pi \lambda^{3} \left\{ x^{2} + \frac{\left[(2x+1) \exp(-2x) - 1 \right]}{2} \right\}, \tag{22}$$

where λ is the mean free path, $x = r/\lambda$, and r is the cluster radius.

Further, the intensity of the signal from the shell can be calculated as the difference between the intensities of the signals from a spherical particle with the same diameter and a core made of the shell material. Equation (23) includes the attenuation of the core signal on a uniform shell layer, but the real thickness is different. Thus, the intensity can be approximately calculated as:

$$S(\text{core}) = \exp\left(-\frac{d}{\lambda_{S}}\right)\pi\lambda_{C} \times \left\{x^{2} + \frac{\left[(2x+1)\exp(-2x) - 1\right]}{2}\right\}.$$
(23)

In Eq. (23), the average shell thickness and mean free paths of the corresponding photoelectrons in the core (λ_C) and shell (λ_S) are introduced, respectively.

Extended Eq. (23) in the form (24) includes additional factors [147]:

$$S(\text{core}) = \left\{ \frac{\left[k(x)d + \lambda\right]}{d + \lambda} \right\} \exp\left(-\frac{d}{\lambda}\right) \pi \lambda^{3} \times \left\{ x^{2} + \frac{\left[(2x+1)\exp(-2x) - 1\right]}{2} \right\}.$$
(24)

Numerical determination of the photoemission intensity of layers is given in [116] for spherical and cylindrical Si₃N₄ particles coated with a layer of hydrocarbon contamination. Particle hemispheres were divided into 9 segments of 10°, in each of which deff was determined from the average angle; photoemission intensities of the segments were multiplied by geometric correction factors proportional to the projection of the segment area and summed up (Fig. 13).

Based on the results of [115], the coefficients for spherical and cylindrical objects were obtained geometric equations from considerations. The and calculations were tested on two series of experiments with oxidized Si₃N₄ particles and aluminum foil. The possibility of such calculations using confirmed the XPS MultiOuant software, the library of which includes all the necessary parameters. It is shown that the use of the flat layered structure model leads to an overe stimation of the layer thicknesses.

For hemispherical particles on a substrate, the photoemission intensity was also calculated using Eq. (25) given in [148]:

$$\frac{I_{\text{ads,normal}}}{I_{\text{ads,normal},\infty}} = \pi n R^2 - 2\pi n \lambda_{\text{ads}}^2 \times \left[1 - \left(1 + \frac{R}{\lambda_{\text{ads}}}\right) \exp\left(-\frac{R}{\lambda_{\text{ads}}}\right)\right].$$
(25)

Here n is the density of particles, R is the radius, λ_{ads} is the mean free path of photoelectrons in the surface layer.

The intensity of the signal from the substrate, respectively, was calculated by Eq. (26):

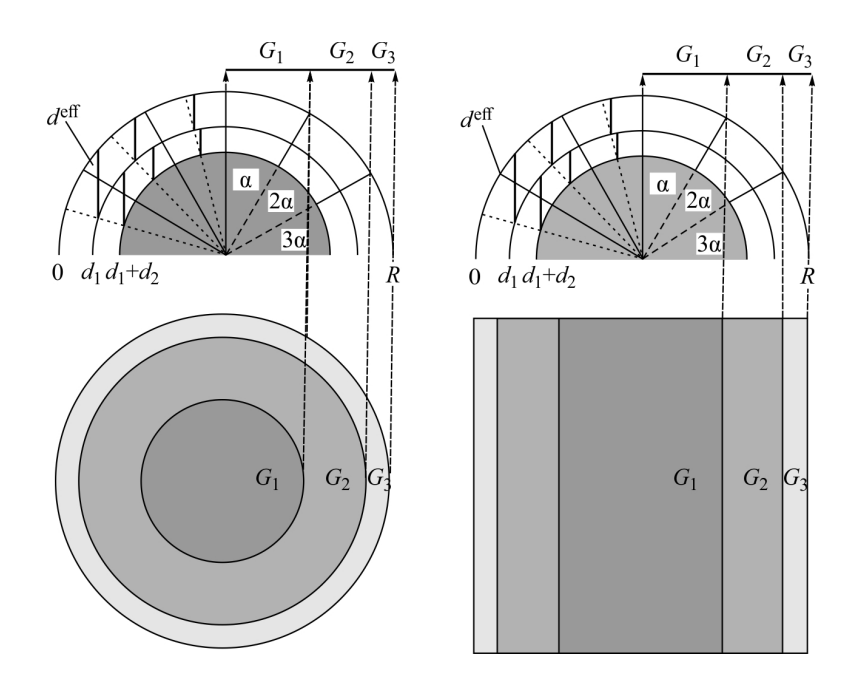


Fig. 13. Axial sections and top view of a sphere and a cylinder with two layers of coatings, made to sum the signal from the material of the core and two coating layers. Sectional sections are identical, but the shapes and ratios of the projected areas differ [115].

$$\frac{I_{\text{sub,normal}}}{I_{\text{sub,normal},\infty}} = 1 - \pi n R^2 - 2\pi n \lambda_{\text{sub}}^2 \times \left[1 - \left(1 + \frac{R}{\lambda_{\text{sub}}}\right) \exp\left(-\frac{R}{\lambda_{\text{sub}}}\right)\right].$$
(26)

Both of Eqs. (25, 26) are valid only for normal detection, and for the ratio of the photoemission intensities of the same layers measured at an angle θ , the same equation looks as follows (27):

$$\frac{I_{\text{sub},\theta}}{I_{\text{sub},\theta,0}} = 1 - f(\theta, R/\lambda) \left(1 - \frac{I_{\text{sub,normal}}}{I_{\text{sub,normal},0}}\right). \tag{27}$$

The coefficient f is found from the graph according to the desired angle to the normal and the ratio R/λ . The same correction factor can be calculated by Eq. (28):

$$f(\theta, R/\lambda) = A \exp\left(-\left(\frac{R}{\lambda}\right)/R'\right) + B,$$
 (28)

where A and R' are correction parameters, B is the asymptotic value [149].

Another theoretical approach for calculating the photoemission intensities of spherical particles of the core–shell structure was proposed in [150, 151]). This model assumes that the particles have spherical symmetry and the core is in the center, the core radius is r, and the shell thickness is d. Then the signal intensity from the particle core $I(\lambda_{AL}, d, r)$ will be equal to (29):

$$I(\lambda_{AL}, d, r) = nS(\lambda_{AL}, r) \times \exp\left(-\frac{d}{\lambda_{AL}}\right) h\left(\frac{d}{\lambda_{AL}}, \frac{r}{\lambda_{AL}}\right) F_{1}\left(\frac{r}{\lambda_{AL}}\right), \tag{29}$$

and the explanation of the functions included in (29) can be represented by Eqs. (30)–(33):

$$S(\lambda_{\rm AL}, r) = \frac{I_0 \lambda_{\rm AL} \pi r^2}{n},\tag{30}$$

(28)
$$h(\delta, \rho) = \frac{k(\rho)\delta + 1}{\delta + 1},$$

$$k(\rho) = \frac{\beta_1 \rho^2 + \beta_2 \rho + 1}{\beta_1 \rho^2 + \beta_2 \rho + 1},$$
(32)

$$F_{1}(\rho) = 1 + \frac{(2\rho + 1)\exp(-2\rho) - 1}{2\rho^{2}}.$$
(33) $C_{SiO_{2}} = \frac{I_{S}}{I_{S} + \mu I_{C}},$

In this model, λ_{AL} is the effective attenuation length. If the angle from the normal does not exceed 60° and the elastic scattering effects are small, the mean free path λ can be used. The atomic sensitivity factors are given by the equation for $S(\lambda_{AL}, r)$, where n is the atomic density, I_0 is the signal intensity from the bulk material with a clean surface, which is proportional to the atomic sensitivity factor at a given photon energy. Further, $h(\delta, \rho)$ and $k(\rho)$ are empirically obtained functions with three given constants: $\beta_1 = 0.00288984$, $\beta_2 = 0.05135594$, $\beta_3 = 0.45982462$.

If the theoretical intensity of the photoemission of the core can be expressed as $I_{\rm c}(\lambda_{\rm AL_c}$, d, r), where $\lambda_{\rm AL_c}$ is the average attenuation length of the photoelectrons corresponding to the elements of the core, then the theoretical intensity of the photoemission of the shell (34) can be described as:

$$I_{S} = I(\lambda_{AL_{c}}, d = 0, r + d) - I(\lambda_{AL_{c}}, d, r), \tag{34}$$

where λ_{AL_s} is the average attenuation length of photoelectrons from the shell. The first term corresponds to the intensity of the signal from a spherical particle of radius (r + d) consisting of the shell material, the second corresponds to the intensity of the signal from a particle of radius r, of the same composition. The theoretical ratio of the intensities of photoelectron lines (35) of the shell and core will be equal, respectively [152, 153]:

$$\frac{I_{\rm S}}{I_{\rm C}} = \frac{I(\lambda_{\rm AL_{\rm S}}, d=0, r+d)}{I(\lambda_{\rm AL_{\rm C}}, d, r)}.$$
(35)

The above equations were used to calculate the shell thickness in bimetallic nanoparticles with a core consisting of gold, platinum, and rhodium, and a shell made of iron oxide [89]. This method was used to determine the growth of oxide shells on spherical silicon particles (with an initial radius of 5 nm) under normal conditions [154, 155].

The relative concentrations of oxide forms of silicon in the oxide shell can be found from Eq. (36) [150]:

where μ is the ratio of atomic densities in silicon (4.96·10²² cm⁻³) and silicon dioxide (2.27·10²² cm⁻³).

Software

To simulate Auger electron and X-ray photoelectron spectra and improve the accuracy of determinations in the routine analysis of samples of complex composition, the SESSA software was developed [156]. The program contains the necessary physical parameters and gives an estimate of the intensities of peaks and electronic spectra, energy and angular distributions of photoelectrons, taking into account elastic and inelastic scattering for multilayer thin films. Theoretically, the processes of formation of signal intensities on complex samples are described in a number of works, for example, [157]. Examples of use are given in [158].

In the SESSA software, the calculation of electron energy losses occurs in the infinite medium approximation, and the decrease in the peak intensity in XPS arises due to losses due to surface excitation and internal excitations (due to the appearance of a static hole in the process of photoemission) [159]. A one-step model that takes into account both of these phenomena and is based on the semi-classical dielectric response is introduced into the **QUEELS-XPS** model software, which performs a quantitative analysis of the intensity of the background by electrons with energy loss.

The Tougaard algorithm underlying the QUASES program is based on the assumption that the elastic scattering of electrons can be neglected estimate the depth distribution background shape on the low-energy of the peaks [84]. Verification of this assumption using the SESSA software on two types of samples of different Cu/Au configuration and similar Si/SiO₂ structure is given in [86] (Fig. 14).

In [160], the QUASES-Tougaard software was used to analyze gold nanoclusters on the surface of polystyrene. Spherical gold nanoclusters were deposited on polystyrene substrates and survey spectra were studied. The sample was presented in the form of spheres with a diameter of 2R with surface coverage f_1 . For quantitative calculations, the spheres were conditionally divided into 9 coaxial cylinders of equal area and different heights (Fig. 15).

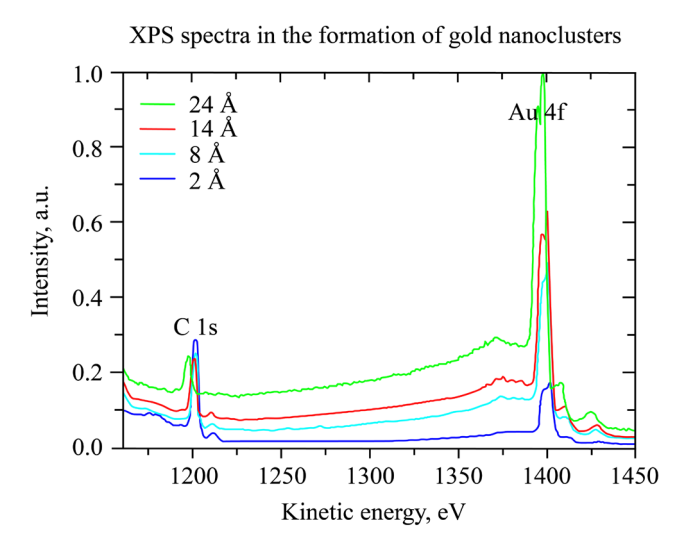


Fig. 14. X-ray photoelectron spectra obtained from samples with different effective thicknesses of the gold layer (from 0.2 to 2.4 nm). As the thickness of the gold layer increases, the photoelectron peaks C 1s and Au 4f shift, and the intensity of the peaks and the background of inelastically scattered electrons increases [160].

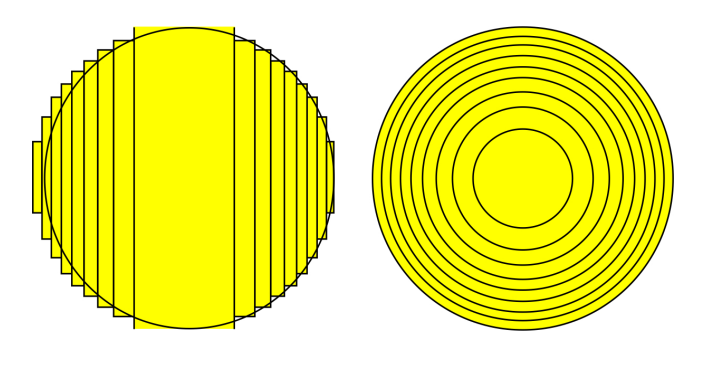


Fig. 15. Separation of spheres of radius 2*R* into 9 coaxial cylindrical shells with equal area and different heights in vertical and lateral projections was performed to calculate the total signal intensity [160].

In [86], the program generated spectra for samples containing gold and copper in the form of various compounds and alloys, as well as for silicon and silicon dioxide, with different distributions over the depth and area of the sample. In [161], the surface was coated by deposition of vanadium oxide and cerium oxide on aluminum oxide substrates, and cerium oxide and cadmium sulfide on titanium oxide substrates. The experimental spectra obtained were in good agreement with those generated in the program.

Overcoming the challenges of nanoparticle analysis

The main parameters studied in characterization of nanoparticles are the size and shape, qualitative and quantitative composition, the size distribution function of nanoparticles, the degree of aggregation, surface charge and surface area, and the chemical composition of the surface of particles of the core-shell type [3, 51, 162, 163]. The average size, size distribution and organic ligands present on the surface of the particles can influence the properties and possible applications of the nanoparticles. In addition, the structure of nanoparticles and their chemical composition should be investigated both at the first stage after the synthesis of nanoparticles and for a sufficiently long time after synthesis due to the influence of the aging effect of nanoparticles [3, 51].

The results of methods for measuring the physicochemical of parameters nano-objects significantly affect the prediction of the use of materials for these commercial purposes. At present, the scientific community is faced with t he task of further improving the accuracy and resolution of many methods for the analysis of nanoparticles and nanomaterials [49, 51, 162–165]. However, there are significant problems in the analysis of nanomaterials due to the lack of suitable standard materials for calibrating analytical instruments, difficulties associated with sample preparation for analysis and interpretation of data in situ and operando, especially in largescale production, as well as their in complex matrices [49, 164].

Obtaining a sufficiently complete picture of the properties of nanomaterials requires the use of a group of complementary instrumental methods of analysis [3, 44, 63-67]. Of particular interest are ultrafast spectral and diffraction methods, which make it possible to understand the connection between the elements of the structure-dynamicsfunction triad. Significant success in their application to the study of nano-objects is associated with the development of synchrotron radiation technologies and free electron lasers, which provide X-ray sources of high brightness and high temporal resolution [53–56]. As applied to nano-objects, the use of ultrashort X-ray pulse makes it diffraction possible study heterogeneous processes at the solid-liquid surface interface, which includes the preparation of thin liquid films and XPS measurements at high (atmospheric) pressure [60, 61, 91, 94, 165], structural dynamics in extreme conditions, which makes it possible to provide information about the behavior of nanoobjects in states far from equilibrium.

CONCLUSIONS

The review depicted a number of methods for the synthesis and preparation of nanomaterials with a wide range of their applications. With the expansion of the production of nanoparticles, more reliable rapid methods of analysis will be required. Currently, the analysis is focused not only on the characterization of the core of nanoparticles, but also on surface ligands that affect their physical properties. Due to the difficulties with reproducibility and reliability in determining the physicochemical parameters nanomaterials, a combined approach is required to find their required properties. Some issues in the field of nanomaterials research remain unresolved. This review describes the role of a number of methods for characterizing nanomaterials, highlights their advantages and limitations, as well as the possibilities of effective combination, presents both general and modern operando methods that are used to monitor the formation kinetics and properties of nanoparticles.

XPS is the most widely used analytical method for chemical surface analysis and is also used to characterize nanoparticles and nanomaterials. Its physical principle is based on the photoelectric effect. XPS is a powerful quantitative method useful for elucidating the electronic structure, elemental composition, and oxidation states of elements in a material. It can also analyze ligand exchange interactions, nanoparticle surfaces, and core—shell structures.

Compared to microscopy methods such as TEM and TEM/EELS (electron energy loss spectroscopy in a transmission electron microscope), which use transverse spatial resolution to identify elements in the transmission direction, XPS examines the composition of a material by analyzing the spectrum of ejected electrons. As an added benefit, XPS provides depth information similar to the size of nanoparticles (up to 10 nm deep from the surface) and does not cause significant damage to samples. Two disadvantages of XPS are the need for careful sample preparation (requires a dry solid form without contamination) and data interpretation.

XPS is a reliable and useful tool for the quantitative study of proteins as well as peptides adsorbed at interfaces. The method can also characterize the molecular interface. Chemical information from the surface of nanoparticles analyzed by XPS can be used to estimate the thickness of nanoparticle coatings. XPS also provides information about their dielectric properties by recording the behavior of nanomaterials during charging/discharging.

The advantage of the high sensitivity of XPS should be emphasized, since each element has a certain characteristic set of peaks in the photoelectron spectrum at kinetic energies determined by the photon energy and the corresponding binding energies, and the intensity of the peaks depends on the concentration of the corresponding element.

Originally existing as a method for carrying out measurements and research under conditions of ultrahigh vacuum, XPS has also been developed in application to processes and objects that occur and exist at higher pressures comparable to atmospheric pressure. Therefore, the range of possible measurement samples has expanded to include solutions (for example, solutions of nanoparticles), thin liquid films, and biological objects. The changes affected the design of the device and also affected the radiation sources. It became possible to use synchrotron and ultraviolet sources, access to the measurement of new spectra, for example, the spectra of the valence band, and the determination of the corresponding characteristics of matter. One of the main problems solved by the XPS method is the measurement of the composition and structure of layered samples and samples of a complex, inhomogeneous structure (spherical particles) and the determination of the concentration profile of elements in them. Another problem associated with quantitative analysis is the technique for subtracting non-linear background, especially under complex spectra of samples containing several different overlapping lines. To solve these problems, special software has been created, the principle of which is to approximate the model spectrum for the proposed structure of the sample to the experimental spectrum.

However, despite difficulties all the and problems associated with the analysis nanomaterials, XPS successfully makes it possible to determine the charge states of elements, the composition and structure of the surface of various samples (and the list of possible samples and methods for their analysis is constantly expanding) by performing in situ and operando analysis. In combination with methods that make it possible to study the physical structure and structure of samples, the XPS method is able to provide sufficient information for the processes of obtaining and using nano-objects.

Acknowledgments

The work was supported by the Russian Foundation for Basic Research grant No. 20-02-00146 A.

Authors' contributions

- **A.A.** Ischenko writing the main part of the review, editing the text, combining materials from different authors, and assembling a full text.
- **M.A.** Lazov writing the main part of the review, text design and preparation for publication.
- **E.V. Mironova** consultations and text additions on analytical research methods of various objects, editing and formatting the text.
- **A.Yu. Putin** consultations and text additions on the technology of obtaining nanomaterials and their physical properties.
- **A.M.** Ionov consultations and text additions on the topic of nanomaterials research by the XPS and on the basics and advanced theory of the XPS method.
- **P.A. Storozhenko** consultations and text additions on the topic of studying the properties of nanomaterials by various physical and physicochemical methods.

The authors declare no conflicts of interest.

REFERENCES

- 1. Eliseev A.A., Lukashin A.V. *Funktsional'nye nanomaterialy* (Tretyakov Yu.D. (Ed.). Functional Nanomaterials). Moscow: FIZMATLIT; 2010. 456 c. (in Russ.). ISBN 978-5-9221-1120-1
- 2. Chaudhuri R.G., Paria S. Core/Shell Nanoparticles: Classes, Properties, Synthesis Mechanisms, Characterization, and Applications. *Chem. Rev.* 2012;112(4):2373–2433. https://doi.org/10.1021/cr100449n
- 3. Ischenko A.A., Fetisov G.V., Aslanov L.A. *Nanosilicon:* properties, synthesis, applications, methods of analysis and control. London: CRC, Taylor & Francis; 2015. 727 p.
- [Original Russian Text: Ischenko A.A., Fetisov G.V., Aslanov L.A. Nanokremnii: svoistva, poluchenie, primenenie, metody issledovaniya i kontrolya (Nanosilicon: properties, synthesis, applications, methods of analysis and control). Moscow: FIZMATLIT; 2013. 614 p. (in Russ.). ISBN 978-5-9221-1369-4]
- 4. Borisenko V.E. Nanoelectronics a basis of information systems for the 21st century. *Sorosovskii Obrazovatel'nyi Zhurnal = Soros Educational Journal*. 1997;(5):100–104 (in Russ.). URL: http://www.pereplet.ru/nauka/Soros/pdf/9705_100.pdf
- 5. Osetrov A.Yu., Vigdorovich V.I. Modern nano technologies. State, problems, and perspectives. Vestnik Tambovskogo universiteta. Seriya Estestvennye i tekhnicheskie nauki = Tambov University Reports. Series: Natural and Technical Sciences. 2013;18(5):2371–2374 (in Russ.).
- 6. Demikhovskii V.Ya. Quantum wells, wires and dots. Sorosovskii Obrazovatel'nyi Zhurnal = Soros Educational Journal. 1997;(5):80–86 (in Russ.). URL: http://window.edu.ru/resource/993/20993/files/9705 080.pdf
- 7. ShikA. Ya. Guantum wires. Sorosovskii Obrazovatel'nyi Zhurnal = Soros Educational Journal. 1997;(5):87–92 (in Russ.). URL: http://pereplet.ru/nauka/Soros/pdf/9705_087.pdf
- 8. Peter Ju., Kardona Yu.M. *Osnovy fiziki poluprovodnikov* (Fundamentals of semiconductor physics: transl. from Engl). Moscow: FIZMATLIT; 2002. 560 p. (in Russ.). ISBN 5-9221-0268-0
- 9. Peter Y., Cardona Yu.M. Fundamentals of semiconductors: Physics and materials properties (Graduate texts in physics). 4th ed. Berlin-Heidelberg: Springer-Verlag; 2010. 775 p. ISBN 978-364-200-709-5
- 10. Hamaguchi C. *Basic semiconductors physics*. 2nd ed. Berlin Heidelberg: Springer-Verlag; 2010. 570 p. ISBN 978-3-642-03302-5
- 11. Baer D.R., Amonette J.E., Engelhard M.H., Gaspar D.J., Karakoti A.S., Kuchibhatla S., Nachimuthu P., Nurmi J.T., Qiang Y., Sarathy V., Seal S., Sharma A., Tratnyek P.G., Wang C.-M. Characterization challenges for nanomaterials. *Surf. Interface Anal.* 2008;40(3–4):529–537. https://doi.org/10.1002/sia.2726
- 12. Koole R., Groeneveld E., Vanmaekelbergh D., Meijerink A., de Mello Donegá C. Size Effects on Semiconductor Nanoparticles. In: de Mello Donegá C. (Eds.) *Nanoparticles*. Berlin, Heidelberg: Springer; 2014. 299 p. https://doi.org/10.1007/978-3-662-44823-6 2
- 13. Sun C.Q. Relaxation of the Chemical Bond. Skin Chemisorption Size Matter ZTP Mechanics H2O Myths. Singapore: Springer Science & Business Media; 2014. 807 p. https://doi.org/10.1007/978-981-4585-21-7

- 14. Attia Y., Samer M. Metal clusters: New era of hydrogen production. *Renew. Sust. Energ. Rev.* 2017;79:878–892. https://doi.org/10.1016/j.rser.2017.05.113
- 15. Jin R., Li G., Sharma S., Li Y., Du X. Toward Active-Site Tailoring in Heterogeneous Catalysis by Atomically Precise Metal Nanoclusters with Crystallographic Structures. *Chem. Rev.* 2021;121(2):567–648. https://doi.org/10.1021/acs.chemrev.0c00495
- 16. Liu L., Corma A. Metal catalysts for heterogeneous catalysis: from single atoms to nanoclusters and nanoparticles. *Chem. Rev.* 2018;118(10):4981–5079. https://doi.org/10.1021/acs.chemrev.7b00776
- 17. Cuenya B.R. Synthesis and catalytic properties of metal nanoparticles: Size, shape, support, composition, and oxidation state effects. *Thin Solid Films*. 2010;518(12):3127–3150. https://doi.org/10.1016/j.tsf.2010.01.018
- 18. Wang H., Wang L., Lin D., Feng X., Niu Y., Zhang B., Xiao F.S. Strong metal–support interactions on gold nanoparticle catalysts achieved through Le Chatelier's principle. *Nat. Catal.* 2021;4(5):418–424. https://doi.org/10.1038/s41929-021-00611-3
- 19. Chen M.S., Goodman D.W. Structure-activity relationships in supported Au catalysts. *Catal. Today*. 2006;111(1-2):22-33. https://doi.org/10.1016/j.cattod.2005.10.007
- 20. Cheng N., Zhang L., Doyle-Davis K., Sun X. Single-Atom Catalysts: From Design to Application. *Electrochem. Energ. Rev.* 2019;2(4):539–573. https://doi.org/10.1007/s41918-019-00050-6
- 21. Rong H., Ji S., Zhang J., Wang D., Li Y. Synthetic strategies of supported atomic clusters for heterogeneous catalysis. *Nat. Commun.* 2020;11:5884(14 p.). https://doi.org/10.1038/s41467-020-19571-6
- 22. Zhang Y., Yang J., Ge R., Zhang J., Cairney J.M., Li Y., Zhu M., Li S., Li W. The effect of coordination environment on the activity and selectivity of single-atom catalysts. *Coord. Chem. Rev.* 2022;461:214493(48 p.). https://doi.org/10.1016/j.ccr.2022.214493
- 23. Sankar M., He Q., Engel R.V., Sainna M.A., Logsdail A.J., Roldan A., Willock D.J., Agarwal N., Kiely C.J., Hutchings G.J. Role of the support in gold-containing nanoparticles as heterogeneous catalysts. *Chem. Rev.* 2020;120(8):3890–3938. https://doi.org/10.1021/acs.chemrev.9b00662
- 24. Jiang Zh., Zhang W., Jin L., Yang X., Xu F., Zhu J., Huang W. Direct XPS Evidence for Charge Transfer from a Reduced Rutile TiO₂(110) Surface to Au Clusters. *J. Phys. Chem. C.* 2007;111(33): 12434–12439. https://doi.org/10.1021/jp073446b
- 25. Haruta M. Size- and support-dependency in the catalysis of gold. *Catal. Today*. 1997;36(1):153–166. https://doi.org/10.1016/S0920-5861(96)00208-8
- 26. Kung M.C., Lee J.H., Chu-Kang A., Kung H.H. Selective reduction of NO $_x$ by propene over Au/ γ -Al $_2$ O $_3$ catalysts. *Stud. Surf. Sci. Catal.* A. 1996;101:701–707. https://doi.org/10.1016/s0167-2991(96)80281-3
- 27. Ueda A., Oshima T., Haruta M. Reduction of nitrogen monoxide with propene in the presence of oxygen and moisture over gold supported on metal oxides. *Appl. Catal. B.* 1997;12(2–3):81–93. https://doi.org/10.1016/s0926-3373(96)00069-0
- 28. Sanchez R.M.T., Ueda A., Tanaka K., Haruta M. Selective oxidation of CO in hydrogen over gold supported on manganese oxide. *J. Catal.* 1997;168(1):125–127. https://doi.org/10.1006/jcat.1997.1636

- 29. Smolentseva E.V., Bogdanchikova N.E., Simakov A.V., Pestryakov A.N., Tuzovskaya I.V., Avalos M., Farias M., Diaz A. Influence of modifyning agent on physical and chemical properties and catalytic properties of gold zeolite catalysts. *Izvestiya Tomskogo politekhnicheskogo universiteta = Bulletin of the Tomsk Polytechnic University.* 2005;308(4):93–98 (in Russ.).
- 30. Shubhashish S., Karasik S.J., Posada L.F., Amin A.S., Achola L.A., Nisly N., Willis W.S., Suib S.L. Syntheses of gold supported on metal oxides and their application in organic transformations. *Microporous Mesoporous Mater*: 2022;336:111888(p.). https://doi.org/10.1016/j. micromeso.2022.111888
- 31. Lin J.N., Chen J.H., Hsiao C.Y., Kang Y.-M., Wan B. Gold supported on surface acidity modified Y-type and iron/Y-type zeolite for CO-oxidation. *Appl. Catal. B.* 2002;36(1):19–29. https://doi.org/10.1016/s0926-3373(01)00276-4
- 32. Espinos J.P., Morales J., Barranco A., Caballero A., Holgado J.P., Gonzalez-Elipe A. Interface Effects for Cu, CuO, and Cu₂O Deposited on SiO₂ and ZrO₂. XPS Determination of the Valence State of Copper in Cu/SiO₂ and Cu/ZrO₂ Catalysts. *J. Phys. Chem.* B. 2002;106(27):6921–6929. https://doi.org/10.1021/jp014618m
- 33. Mazalova V.N., Kravtsova A.N., Soldatov A.V. Nanoklastery. Rentgenospektral'nye issledovaniya i komp'yuternoe modelirovanie (Nanoclusters. X-ray spectral studies and computer modeling). Moscow: FIZMATLIT; 2013. 184 p. (in Russ.).
- 34. Sacher E. Asymmetries in Transition Metal XPS Spectra: Metal Nanoparticle Structure, and Interaction with the Graphene-Structured Substrate Surface. *Langmuir*. 2010;26(6):3807–3814. https://doi.org/10.1021/la902678x
- 35. Alov N.V., Kutsko D.M., Bordo K.V. Ion-beam reduction of the surface of higher oxides of molybdenum and tungsten. *J. Surf. Investig.* 2008;(2):184–188. https://doi.org/10.1134/S1027451008020043
- [Original Russian Text: Alov N.V., Kutsko D.M., Bordo K.V. Ion-beam reduction of the surface of higher oxides of molybdenum and tungsten. *Poverkhnost'. Rentgenovskie, sinkhrotronnye i neitronnye issledovaniya = Journal of Surface Investigation. X-Ray, Synchrotron and Neutron Techniques.* 2008;(3):17–22 (in Russ.).]
- 36. Alov N.V., Kutsko D.M. Surface composition modification of tungsten higher oxide upon He⁺ ion bombardment. *J. Surf. Investing.* 2008;6(2):225–228. https://doi.org/10.1134/S1027451012030032
- [Original Russian Text: Alov N.V., Kutsko D.M. Surface composition modification of tungsten higher oxide upon He⁺ ion bombardment. Poverkhnost'. Rentgenovskie, sinkhrotronnye i neitronnye issledovaniya = Journal of Surface Investigation. X-Ray, Synchrotron and Neutron Techniques. 2012;(3):38–41 (in Russ.).]
- 37. Alov N., Kutsko D., Spirovova I., Bastl Z. XPS study of vanadium surface oxidation by oxygen ion bombardment. *Surf. Sci.* 2006;600(8):1628–1631. https://doi.org/10.1016/j.susc.2005.12.052
- 38. Alov N.V., Kutsko D.M. Ion Beam Reduction of the Surface of Higher Niobium Oxide. *J. Surf. Investing*. 2010;4(2):232–235. https://doi.org/10.1134/S1027451010020096

[Original Russian Text: Alov N.V., Kutsko D.M. Ion Beam Reduction of the Surface of Higher Niobium Oxide. *Poverkhnost'. Rentgenovskie, sinkhrotronnye i neitronnye issledovaniya = Journal of Surface Investigation. X-Ray, Synchrotron and Neutron Techniques.* 2010;(3):66–70 (in Russ.).]

- 39. Khanuja M., Sharma H., Mehta B.R., Shivaprasad S.M. XPS depth-profile of suboxide distribution at the native oxide/Ta interface. *J. Electron. Spectrosc. Relat. Phenom.* 2009;169(1):41–45. https://doi.org/10.1016/j.elspec.2008.10.004
- 40. Alov N.V., Kutsko D.M. Ion Beam Reduction of the Surface of Tantalum Higher Oxide. *J. Surf. Investing*. 2011;5(2):259–262. https://doi.org/10.1134/S1027451011030037
- [Original Russian Text: Alov N.V., Kutsko D.M. Ion Beam Reduction of the Surface of Tantalum Higher Oxide. *Poverkhnost'. Rentgenovskie, sinkhrotronnye i neitronnye issledovaniya = Journal of Surface Investigation. X-Ray, Synchrotron and Neutron Techniques.* 2011;(3):59–62 (in Russ.).]
- 41. Pradeep T., Anshup. Noble metal nanoparticles for water purification: A critical review. *Thin Solid Films*. 2009;517(24):6441–6478. https://doi.org/10.1016/j.tsf.2009.03.195
- 42. Kuzmicheva G.M. Nanosized phases with titanium(IV) oxides. Preparation. Characterisation. Properties. *Fine Chem. Technol.* 2015;10(6):5–36 (in Russ.).
- 43. Siciliano P. Preparation, characterisation and applications of thin films for gas sensors prepared by cheap chemical method. *Sens. Actuat. B: Chem.* 2000;70(1–3):153–164. https://doi.org/10.1016/s0925-4005(00)00585-2
- 44. Antipin I.S., *et al.* Functional supramolecular systems: design and applications. *Russ. Chem. Rev.* 2021;90(8):895–1107. https://doi.org/10.1070/RCR5011
- 45. Ding P., Chen L., Wei C., Zhou W., Li C., Wang J., Wang M., Guo X., Stuart M.A.C., Wang J. Efficient Synthesis of Stable Polyelectrolyte Complex Nanoparticles by Electrostatic Assembly Directed Polymerization. *Macromol. Rapid Comm.* 2021;42(4):2000635(1–9). https://doi.org/10.1002/marc.202000635
- 46. Stuart M.A.C. Supramolecular perspectives in colloid science. *Colloid Polym, Sci.* 2008;286(8–9):855–864. https://doi.org/10.1007/s00396-008-1861-7
- 47. Mourdikoudis S., Pallares R.M., Thanh N.T.K. Characterization techniques for nanoparticles: comparison and complementarity upon studying nanoparticle properties. *Nanoscale*. 2018;10(27):12871–12934. https://doi.org/10.1039/C8NR02278J
- 48. Grainger D.W., Castner D.G. Nanobiomaterials and nanoanalysis: opportunities for improving the science to benefit biomedical technologies. *Adv. Mater.* 2008;20(5):867–877. https://doi.org/10.1002/adma.200701760
- 49. Montaño M.D., Ranville J., Lowry G.V., Blue J., Hiremath N., Koenig S., Tuccillo M.E., Gardner S.P. Detection and Characterization of Engineered Nanomaterials in the Environment: Current State-of-the-Art and Future Directions. Washington, DC: U.S. Environmental Protection Agency Office of Research and Development. 2020.186 p. URL: https://clu-in.org/download/techfocus/nano/Nano-Gardner-600-r-14-244.pdf
- 50. Baer D.R., Engelhard M.H. XPS analysis of nanostructured materials and biological surfaces. *J. Electron Spectrosc.* 2010;178–179:415–432. https://doi.org/10.1016/j.elspec.2009.09.003
- 51. Koroleva M.Yu., Yurtov E.V. Ostwald ripening in macro- and nanoemulsions. *Uspekhi khimii = Russ. Chem. Rev.* 2021;90(3):293–323 https://doi.org/10.1070/RCR4962
- 52. Neoh K.G., Li M., Kang E.-T. Characterization of Nanomaterials/Nanoparticles. In: Kishen A. (Ed.). *Nanotechnology on Endodontics: Current and Potential Clinical Applications*. Switzerland: Springer International Publishing; 2015. P. 23–44. https://doi.org/10.1007/978-3-319-13575-5 3

- 53. Ischenko A.A., Weber P.M., Miller R.J.D. Transient structures and chemical reaction dynamics. *Russ. Chem. Rev.* 2017;86(12):1173–1253. https://doi.org/10.1070/RCR4754
- 54. Ischenko A.A., Fetisov G.V. *Structural dynamics*: in 2 v. Moscow: FIZMATLIT; 2021. V. 1. 486 p. ISBN 978-5-9221-1936-9. V. 2. 467 p. ISBN 978-5-9221-1937-5 (in Russ.).
- 55. Nguyen M.T., Nefedov V.I., Chekalkin N.S., Kozlovsky I.V., Malafeev A.V., Mirolyubova N.A., Nazarenko M.A. On the integration of the methods of forming and research of images of objects against the background of noises and interference. *Russ. Technol. J.* 2020;8(2):33–42 (in Russ.). https://doi.org/10.32362/2500-316X-2020-8-2-33-42]
- 56. Aseyev S.A., Ischenko A.A., Kompanets V.O., Kochikov I.V., Malinovskii A.L., Mironov B.N., Poydashev D.G., Chekalin S.V., Ryabov E.A. Study of the Processes Induced by Femtosecond Laser Radiation in Thin Films and Molecular-Cluster Beams Using Ultrafast Electron Diffraction. *Crystallogr. Rep.* 2021;66(6):1031–1037. https://doi.org/10.1134/S106377452106002X
- 57. Baer D.R. Guide to making XPS measurements on nanoparticles. *J. Vac. Sci. Technol. A.* 2020;38(3):031201. https://doi.org/10.1116/1.5141419
- 58. Krishna D.N.G., Philip J. Review on surface-characterization applications of X-ray photoelectron spectroscopy (XPS): Recent developments and challenges. *Appl. Surface Sci. Adv.* 2022;12:100332(30 p). https://doi.org/10.1016/j.apsadv.2022.100332
- 59. Baer D.R., Gaspar D.J., Nachimuthu P., Techane S., Castner D. Application of surface chemical analysis tools for characterization of nanoparticles. *Anal. Bioanal. Chem.* 2010;396(3):983–1002. https://doi.org/10.1007/s00216-009-3360-1
- 60. Saveleva V.A., Savinova E.R. Insights into electrocatalysis from ambient pressure photoelectron spectroscopy. *Curr. Opin. Electrochem.* 2019;17:79–89. https://doi.org/10.1016/j.coelec.2019.03.016
- 61. Arble C., Jia M., Newberg J.T. Lab-based ambient pressure X-ray photoelectron spectroscopy from past to present. *Surf. Sci. Rep.* 2018;7(2):37–57. https://doi.org/10.1016/j.sur-frep.2018.02.002
- 62. Vudraf D., Delchar T. Sovremennye metody issledovaniya poverkhnosti (Modern Methods of Surface Research): transl. from Eng. Moscow: Mir; 1989. 564 p. (in Russ.).
- 63. Alov N.V., Lazov M.A., Ischenko A.A. X-ray photoelectron spectroscopy. In: *Analytical Chemistry*: textbook: in 3 v. V. 2. *Instrumental methods of analysis*. *Part 1*. Ischenko A.A. (Ed.). Chapter 3. P. 191–229. Moscow: FIZMATLIT; 2019. 472 p. (in Russ.). ISBN 978-5-9221-1866-8
- 64. Shtykov S.N. Chemical Analysis in Nanoreactors: Main Concepts and Applications. *J. Analyt. Chem.* 2002;57(10):859–868. https://doi.org/10.1023/A:1020410605772
- [Original Russian Text: Shtykov S.N. Chemical Analysis in Nanoreactors: Main Concepts and Applications. *Zhurnal analiticheskoi khimii*. 2002;57(10):1018–1028 (in Russ.).]
- 65. Troyan V.I., Pushkin M.A., Borman V.D., Tronin V.N. Fizicheskie osnovy metodov issledovaniya nanostruktur i poverkhnosti tverdogo tela (Physical foundations of methods for studying nanostructures and solid surface). Borman V.D. (Ed.). Moscow: MEPhI; 2008. 260 p. (in Russ).
- 66. Shtykov S.N. Nanoanalytics: definitions, classification, history and primary advances. In: *Nanoanalytics: Nanoobjects and Nanotechnologies in Analytical Chemistry. Pt. I: Nanoanalytics: Concepts, Elements, and Peculiarities.* Shtykov S.N. (Ed.). Berlin: De Gruyter; 2018. P. 3–52. https://doi.org/10.1515/9783110542011-001

- 67. Shtykov S.N. Nanoanalytics. In: *Analytical Chemistry*: textbook: in 3 v. V. 3. *Instrumental methods of analysis. Part 2*; Ischenko A.A. (Ed.). Chapter 2. P. 96–128. Moscow: FIZMATLIT; 2020. 504 p. (in Russ.). ISBN 978-5-9221-1867-5
- 68. Oswald S. X-ray Photoelectron Spectroscopy in Analysis of Surfaces. In: *Encyclopedia of Analytical Chemistry: Applications, Theory and Instrumentation*. John Wiley & Sons; 2013. P. 1–49. https://doi.org/10.1002/9780470027318.a2517
- 69. Crist B.V. XPS in industry Problems with binding energies in journals and binding energy databases. *J. Electron Spectrosc.* 2019;231:75–87. https://doi.org/10.1016/j.elspec.2018.02.005
- 70. Greczynski G., Hultman L. X-ray photoelectron spectroscopy: Towards reliable binding energy referencing. *Prog. Mater. Sci.* 2020;107:100591(46 p.). https://doi.org/10.1016/j.pmatsci.2019.100591
- 71. Bolli E., Kaciulis S., Mezzi A. ESCA as a Tool for Exploration of Metals' Surface. *Coatings*. 2020;10(12):1182(27 p.). https://doi.org/10.3390/coatings10121182
- 72. Hofmann S. *Auger- and X-ray Photoelectron Spectroscopy in Materials Science*. Berlin Heidelberg: Springer-Verlag; 2013. 527 p. https://doi.org/10.1007/978-3-642-27381-0
- 73. Hűfner S. *Photoelectron Spectroscopy: Principles and Applications*. Berlin Heidelberg: Springer-Verlag; 2003. 661 p.
- 74. Baer D.R., Artyushkova K., Brundle C.R., Castle J., Engelhard M., Gaskell K., Grant J., Haasch R., Linford M.R., Powell C., Shard A., Sherwood P., Smentkowski V. Practical guides for X-ray photoelectron spectroscopy: First steps in planning, conducting, and reporting XPS measurements. *J. Vac. Sci. Technol. A.* 2019;37(3):031401. https://doi.org/10.1116/1.5065501
- 75. Schalm O., Patelli A., Storme P., Crabbé A., Voltolina S., Feyer V., Terryn H. A dataset of high-resolution synchrotron X-ray photoelectron spectra of tarnished silver-copper surfaces before and after reduction with a remote helium plasma at atmospheric pressure. *Elsevier, Data in Brief.* 2021;35:106872. https://doi.org/10.1016/j.dib.2021.106872
- 76. Bagus P., Ilton E., Nelin C. The interpretation of XPS spectra: Insights into materials properties. *Surf. Sci. Rep.* 2013;68(2):273–304. https://doi.org/10.1016/j.surfrep.2013.03.001
- 77. Powell C.J. Improvements in the reliability of X-ray photoelectron spectroscopy for surface analysis. *J. Chem. Educ.* 2004;81(12):1734–1741. https://doi.org/10.1021/ed081p1734
- 78. Powell C.J., Jablonski A. Surface sensitivity of X-ray photoelectron spectroscopy. *Nucl. Instrum. Meth. A.* 2009;601(1–2):54–65. https://doi.org/10.1016/j.nima.2008.12.103
- 79. Shard A.G. Detection limits in XPS for more than 6000 binary systems using Al and Mg Kα X-rays. *Surf. Interface Anal.* 2014;46(3):175–185. https://doi.org/10.1002/sia.5406
- 80. Jo M. Direct, simultaneous determination of XPS background and inelastic differential cross section using Tougaard's algorithm. *Surf. Sci.* 1994;320(1–2):191–200. https://doi.org/10.1016/0039-6028(94)91270-X
- 81. Seah M.P. Background subtraction: I. General behaviour of Tougaard-style backgrounds in AES and XPS. *Surf. Sci.* 1999;420(2–3):285–294. https://doi.org/10.1016/S0039-6028(98)00852-8
- 82. Végh J. The Shirley background revised. *J. Electron Spectrosc.* 2006;151(3):159–164. https://doi.org/10.1016/j.elspec.2005.12.002

- 83. Briggs D., Grant J.T. *Surface analysis by Auger and X-ray photoelectron spectroscopy*. Chichester: IM Publications; 2003. 899 p.
- 84. Powell C.J. New Data Resources and Applications for AES and XPS (Papers from 6th International Symposium on Practical Surface Analysis (PSA-13)). *J. Surf. Anal.* 2014;20(3):155–160. https://doi.org/10.1384/jsa.20.155
- 85. Powell C.J., Jablonski A. Progress in quantitative surface analysis by X-ray photoelectron spectroscopy: current status and perspectives. *J. Electron Spectrosc.* 2010;178–179:331–346. https://doi.org/10.1016/j.elspec.2009.05.004
- 86. Powell C.J., Tougaard S., Werner W.S.M., Smekal W. Sample-morphology effects on X-ray photoelectron peak intensities. *J. Vac. Sci. Technol. A.* 2013;31(2):021402(7 p.). https://doi.org/10.1116/1.4774214
- 87. Powell C.J., Werner W.S.M., Smekal W. Sample-morphology effects on X-ray photoelectron peak intensities. II. Estimation of detection limits for thin-film materials. *J. Vac. Sci. Technol.* A. 2014;32(5):050603(6 p.). https://doi.org/10.1116/1.4891628
- 88. Leckey R. Ultraviolet Photoelectron Spectroscopy of Solids. In: O'Connor D.J., Sexton B.A., Smart R.S.C. (Eds.). Surface Analysis Methods in Materials Science. Springer Series in Surface Sciences. Berlin Heidelberg: Springer; 1993. V. 23. P. 291–300. https://doi.org/10.1007/978-3-662-02767-7_14
- 89. Doh W. H., Papaefthimiou V., Dintzer T., Dupuis V., Zafeiratos S. Synchrotron Radiation X-ray Photoelectron Spectroscopy as a Tool to Resolve the Dimensions of Spherical Core/Shell Nanoparticles. *J. Phys. Chem. C.* 2014;118(46):26621–26628. https://doi.org/10.1021/jp508895u
- 90. Fitch A.N. 2.10 Synchrotron Methods. In: Constable E.C., Parkin G., Que Jr.L. (Eds.). *Comprehensive Coordination Chemistry III*. Elsevier; 2021. P. 160–182. ISBN 9780081026892. https://doi.org/10.1016/B978-0-12-409547-2.14660-8
- 91. Nemšák S., Shavorskiy A., Karslioglu O., Zegkinoglou I., Rattanachata A., Conlon C.S., Keqi A., Greene P.K., Burks E.C., Salmassi F., Gullikson E.M., Yang S.-H., Liu K., Bluhm H., Fadley C.S. Concentration and chemical-state profiles at heterogeneous interfaces with sub-nm accuracy from standing-wave ambient-pressure photoemission. *Nat. Commun.* 2014;5:5441–5447. https://doi.org/10.1038/ncomms6441
- 92. Fetisov G.V. X-ray diffraction methods for structural diagnostics of materials: progress and achievements. *Phys.-Usp.* 2020;63(1)2–32. https://doi.org/10.3367/UFNe.2018.10.038435
- 93. Karslioglu O., Nemsak S., Zegkinoglou I., Shavorskiy A., Hartl M., Salmassi F., Gullikson E.M., Ng M.L., Rameshan Ch., Rude B., Bianculli D., Cordones A.A., Axnanda S., Crumlin E.J., Ross P.N., Schneider C.M., Hussain Z., Liu Z., Fadley C.S., Bluhm H. Aqueous solution/metal interfaces investigated in operando by photoelectron spectroscopy. *Faraday Discuss*. 2015;180:35–53. https://doi.org/10.1039/c5fd00003c
- 94. Kjærvik M., Hermanns A., Dietrich P., Thissen A., Bahr S., Ritter B., Kemnitz E., Unger W.E.S. Detection of suspended nanoparticles with near-ambient pressure X-ray photoelectron spectroscopy. *J. Phys.: Condens. Matter.* 2017;29(47):474002(9 p.). https://doi.org/10.1088/1361-648x/aa8b9d

- 95. Corcoran C.J., Tavassol H., Rigsby M.A., Bagus P., Wieckowski A. Application of XPS to study electrocatalysts for fuel cells. *J. Power Sources*. 2010;195(24):7856–7879. https://doi.org/10.1016/j.jpowsour.2010.06.018
- 96. Brown M. A., Redondo A. B., Sterrer M., Winter B., Pacchioni G., Abbas Z., van Bokhoven J.A. Measure of Surface Potential at the Aqueous–Oxide Nanoparticle Interface by XPS from a Liquid Microjet. *Nano Lett.* 2013;13(11):5403–5407. https://doi.org/10.1021/nl402957y
- 97. Baer D.R., Engelhard M.H., Johnson J.E., Laskin J., Lai J., Mueller K., Munusamy P., Thevuthasan S., Wang H., Washton N. Surface characterization of nanomaterials and nanoparticles: important needs and challenging opportunities. *J. Vac. Sci. Technol. A.* 2013;31(5):050820–050854. https://doi.org/10.1116/1.4818423
- 98. Liu X., Zhang X., Bo V., Li L., Tian H., Nie Y., Sun Y., Xu S., Wang Y, Zheng W., Sun C.Q. Coordination-Resolved Electron Spectrometrics. *Chem. Rev.* 2015;115(14):6746–6810. https://doi.org/10.1021/cr500651m
- 99. Sublemontier O., Nicolas C., Aureau D., Patanen M., Kintz H., Liu X., Gaveau M.-A., Le Garrec J.-L., Robert E., Barreda F.-A., Etcheberry A., Reynaud C., Mitchell J.B., Miron C. X-ray Photoelectron Spectroscopy of Isolated Nanoparticles. *J. Phys. Chem. Lett.* 2014;5(19):3399–3403. https://doi.org/10.1021/jz501532c
- 100. Jiang Z.X., Alkemade P.F.A. The surface transient in Si for SIMS with oblique low-energy O₂⁺ beams. *Surf. Interface Anal.* 1999;27(3):125–131. https://doi.org/10.1002/(SICI)1096-9918(199903)27:3<125::AID-SIA490>3.0.CO;2-8
- 101. Hajati S., Tougaard S. XPS for non-destructive depth profiling and 3D imaging of surface nanostructures. *Anal. Bioanal. Chem.* 2010;396(8):2741–2755. https://doi.org/10.1007/s00216-009-3401-9
- 102. Sostarecz A.G., McQuaw C.M., Wucher A., Winograd N. Depth Profiling of Langmuir-Blodgett Films with a Buckminsterfullerene Probe. *Anal. Chem.* 2004;76(22):6651-6658. https://doi.org/10.1021/ac0492665
- 103. Kozole J., Szakal C., Kurczy M., Winograd N. Model multilayer structures for three-dimensional cell imaging. *Appl. Surf. Sci.* 2006;252(19):6789–6792. https://doi.org/10.1016/j.apsusc.2006.02.209
- 104. Conlan X.A., Gilmore I.S., Henderson A., Lockyer N., Vickerman J. Polyethylene terephthalate (PET) bulk film analysis using C_{60}^+ , Au_3^+ , and Au^+ primary ion beams. *Appl. Surf. Sci.* 2006;252(19):6562–6565. https://doi.org/10.1016/j.apsusc.2006.02.068
- 105. Sakai Y., Iijima Y., Takaishi R., Asakawa D., Hiraoka K. Depth Profiling of Polystyrene Using Charged Water Droplet Impact. *J. Surf. Anal.* 2009;15(3):283–286. https://doi.org/10.1384/jsa.15.283
- 106. Galindo R.E., Gago R., Albella J., Lousa A. Comparative depth-profiling analysis of nanometermetal multilayers by ion-probing techniques. *TrAC Trends Anal. Chem.* 2009;28(4):494–505. https://doi.org/10.1016/j.trac.2009.01.004
- 107. Bakaleinikov L.A., Domracheva Ya.V., Zamoryanskaya M.V., Kolesnikova E.V., Popova T.B., Flegontova E.Yu. Depth profiling of semiconductor structures by X-ray microanalysis using the electron probe energy variation technique. *Semiconductors*. 2009;43(4):544–549. https://doi.org/10.1134/S1063782609040265

- [Original Russian Text: Bakaleinikov L.A., Domracheva Ya.V., Zamoryanskaya M.V., Kolesnikova E.V., Popova T.B., Flegontova E.Yu. Depth profiling of semiconductor structures by X-ray microanalysis using the electron probe energy variation technique. *Fizika i Tekhnika Poluprovodnikov*. 2009;43(4):568–576 (in Russ.).]
- 108. Jablonski A., Powell C.J. Practical expressions for the mean escape depth, the information depth, and the effective attenuation length in Auger-electron spectroscopy and X-ray photoelectron spectroscopy. *J. Vac. Sci. Technol. A.* 2009;27(2):253–261. https://doi.org/10.1116/1.3071947
- 109. Hesse R., Weiß M., Szargan R., Streubel P., Denecke R. Comparative study of the modelling of the spectral background of photoelectron spectra with the Shirley and improved Tougaard methods. *J. Electron. Spectros. Relat. Phenomena.* 2013;186:44–53. https://doi.org/10.1016/j.elspec.2013.01.020
- 110. Tougaard S. Practical guide to the use of backgrounds in quantitative XPS. *J. Vac. Sci. Technol. A.* 2021;39(1):011201(22 p.). https://doi.org/10.1116/6.0000661
- 111. Engelhard M.H., Baer D.R., Herrera-Gomez A., Sherwood P. Introductory guide to backgrounds in XPS spectra and their impact on determining peak intensities. *J. Vac. Sci. Technol. A.* 2020;38(6):063203(24 p.). https://doi.org/10.1116/6.0000359
- 112. Jain V., Biesinger M.C., Linford M.R. The Gaussian-Lorentzian Sum, Product, and Convolution (Voigt) functions in the context of peak fitting X-ray photoelectron spectroscopy (XPS) narrow scans. *Appl. Surf. Sci.* 2018;447:548–553. https://doi.org/10.1016/j.apsusc.2018.03.190
- 113. Hesse R., Weiß M., Szargan R., Streubel P., Denecke R. Improved peak-fit procedure for XPS measurements of inhomogeneous samples—Development of the advanced Tougaard background method. *J. Electron Spectros. Relat. Phenomena.* 2015;205:29–51. https://doi.org/10.1016/j.elspec.2015.06.013
- 114. Zborowski C., Vanleenhove A., Conard T. Comparison and complementarity of QUASES-Tougaard and SESSA software. *Appl. Sur. Sci.* 2022;585:152758(8 p.). https://doi.org/10.1016/j.apsusc.2022.152758
- 115. Briggs D., Seah P. (Eds.). *Practical surface analysis: Auger and X-ray photoelectron spectroscopy*. Chichester: John Wiley & Sons; 1996. V. 1. 674 p.
- 116. Sun C.Q. Size dependence of nanostructures: Impact of bond order deficiency. *Prog. Solid State Ch.* 2007;35(1):1–159. https://doi.org/10.1016/j.progsolidst-chem.2006.03.001
- 117. Hill J., Royce D.G., Fadley C.S., Wagner L.F., Grunthaner F.J. Properties of oxidized silicon as determined by angular-dependent X-ray photoelectron spectroscopy. *Chem. Phys. Lett.* 1976;44(2):225–231. https://doi.org/10.1016/0009-2614(76)80496-4
- 118. Seah M.P. Intercomparison of silicon dioxide thickness measurements made by multiple techniques: The route to accuracy. *J. Vac. Sci. Technol. A.* 2004;22(4):1564–1571. https://doi.org/10.1116/1.1705594
- 119. Tougaard S. Energy loss in XPS: Fundamental processes and applications for quantification, non-destructive depth profiling and 3D imaging. *J. Electron. Spectrosc. Relat. Phenom.* 2010;178–179:128–153. https://doi.org/10.1016/j.elspec.2009.08.005
- 120. Tougaard S. Universality Classes of Inelastic Electron Scattering Cross-sections. *Surf. Interface Anal.* 1997;25(3):137–154. https://doi.org/10.1002/(SICI)1096-9918(199703)25:3<137::AID-SIA230>3.0.CO;2-L

- 121. Tougaard S. Quantification of Nanostructures by Electron Spectroscopy. In: Briggs D., Grant J.T. (Eds.). *Surface Analysis by Auger and X-Ray Photoelectron Spectroscopy*. IM Publications; 2003. P. 295–343.
- 122. Iwai H., Hammond J.S., Tanuma S. Recent status of thin film analyses by XPS. *J. Surf. Anal.* 2009;15(3):264–270. https://doi.org/10.1384/jsa.15.264
- 123. Gunter P.L.J., Dejong A.M., Niemantsverdriet J.W., Rheiter H.J.H. Evaluation of take-off angle-dependent XPS for determining the thickness of passivation layers on aluminum and silicon. *Surf. Interface Anal.* 1992;19(1–12):161–164. https://doi.org/10.1002/sia.740190131
- 124. Cole D.A., Shallenberger J.R., Novak S.W., Moore R.L. SiO₂ thickness determination by X-ray photoelectron spectroscopy, Auger electron spectroscopy, secondary ion mass spectrometry, Rutherford backscattering, transmission electron microscopy, and ellipsometry. *J. Vac. Sci. Technol. B.* 2000;18(1):440–444. https://doi.org/10.1116/1.591208
- 125. Alexander M.R., Thompson G.E., Zhou X., Beamson G., Fairley N. Quantification of oxide film thickness at the surface of aluminum using XPS. *Surf. Interface Anal.* 2002;34(1):485–489. https://doi.org/10.1002/sia.1344
- 126. Olsson C.-O.A., Landolt D. Atmospheric oxidation of a Nb-Zr alloy studied with XPS. *Corros. Sci.* 2004;46(1):213–224. https://doi.org/10.1016/S0010-938X(03)00139-2
- 127. Kappen P., Reihs K., Seidel C., Voetz M., Fuchs H. Overlayer thickness determination by angular dependent X-ray photoelectron spectroscopy (ADXPS) of rough surfaces with a spherical topography. *Surf. Sci.* 2000;465(1–2):40–50. https://doi.org/10.1016/S0039-6028(00)00653-1
- 128. Martin-Concepcion A.I., Yubero F., Espinos J.P., Tougaard S. Surface roughness and island formation effects in ARXPS quantification. *Surf. Interface Anal.* 2004;36(8):788–792. https://doi.org/10.1002/sia.1765
- 129. Cumpson P.J. Thickogram: A method for easy film thickness measurement in XPS. *Surf. Interface Anal.* 2000;29(6):403–406. https://doi.org/10.1002/1096-9918(200006)29:6<403::AID-SIA884>3.0.CO;2-8
- 130. Cui Yi-T., Tougaard S., Oji H., Son J.-Y., Sakamoto Y., Matsumoto T., Yang A., Sakata O., Song H., Hirosawa I. Thickness and structure of thin films determined by background analysis in hard X-ray photoelectron spectroscopy. *J. Appl. Phys.* 2017;121(22):225307-1-10. https://doi.org/10.1063/1.4985176
- 131. Tougaard S. Novel Applications of Inelastic Background XPS Analysis: 3D Imaging and HAXPES. *J. Surf. Anal.* 2017;24(2):107–114. https://doi.org/10.1384/jsa.24.107
- 132. Paynter R.W. An ARXPS primer. *J. Electron. Spectrosc. Relat. Phenom.* 2009;169(1):1–9. https://doi.org/10.1016/j.elspec.2008.09.005
- 133. Cumpson P.J. Angle-resolved XPS and AES: depth-resolution limits and a general comparison of properties of depth-profile reconstruction methods. *J. Electron. Spectrosc. Relat. Phenom.* 1995;73(1):25–52. https://doi.org/10.1016/0368-2048(94)02270-4
- 134. Oswald S., Oswald F. Computer simulation of angle-resolved X-ray photoelectron spectroscopy measurements for the study of surface and interface roughnesses. *J. Appl. Phys.* 2006;100(10):104504(9 p.). https://doi.org/10.1063/1.2386938
- 135. Oswald S., Oswald F. A promising concept for using near-surface measuring angles in angle-resolved X-ray photoelectron spectroscopy considering elastic scattering effects. *J. Appl. Phys.* 2011;109(3):034305(11 p.). https://doi.org/10.1063/1.3544002

- 136. Herrera-Gomez A., Grant J. T., Cumpson P., Jenko M., Aguirre-Tostado F.S., Brundle C.R., Conard T., Conti G., Fadley C.S., Fulghum J., Kobayashi K., Kövér L., Nohira H., Opila R.L., Oswald S., Paynter R.W., Wallace R.M., Werner W.S.M., Wolstenholme J. Report on the 47th IUVSTA Workshop "Angle-Resolved XPS: The current status and future prospects for angle-resolved XPS of nano and subnano films." *Surf. Interface Anal.* 2009;41(11):840–857. https://doi.org/10.1002/sia.3105
- 137. Liu Y., Hofmann S., Wang J.Y. An analytical depth resolution function for the MRI model. *Surf. Interface Anal.* 2013;45(11–12):1659–1660. https://doi.org/10.1002/sia.5319
- 138. Yang J., Li W., Wang D., Li Y. Electronic Metal–Support Interaction of Single-Atom Catalysts and Applications in Electrocatalysis. *Adv. Mater.* 2020;32(49):2003300(29 p.). https://doi.org/10.1002/adma.202003300
- 139. Moretti G. Auger parameter and Wagner plot in the characterization of chemical states by X-ray photoelectron spectroscopy: a review. *J. Electron. Spectrosc. Relat. Phenom.* 1998;95(2–3):95–144. https://doi.org/10.1016/S0368-2048(98)00249-7
- 140. Moretti G. The Wagner plot and the Auger parameter as tools to separate initial- and final-state contributions in X-ray photoemission spectroscopy. *Surf. Sci.* 2013;618:3–11. https://doi.org/10.1016/j.susc.2013.09.009
- 141. Zafeiratos S., Kennou A.A study of gold ultrathin film growth on yttria-stabilized ZrO₂(100). *Surf. Sci.* 1999;443(3):238–244. https://doi.org/10.1016/S0039-6028(99)01014-6
- 142. Fu Q., Wagner T. Interaction of nanostructured metal overlayers with oxide surfaces. *Surf. Sci. Rep.* 2007;62(11):431–498. https://doi.org/10.1016/j.surfrep.2007.07.001
- 143. Fulghum J.E., Linton R.W. Quantitation of coverages on rough surfaces by XPS: an overview. *Surf. Interface Anal.* 1988;13(4):186–192. https://doi.org/10.1002/sia.740130404
- 144. Werner W.S.M., Chudzicki M., Smekal W., Powell C. Interpretation of nanoparticle X-ray photoelectron intensities. *Appl. Phys. Lett.* 2014;104(24):243106(3 p.). https://doi.org/10.1063/1.4884065
- 145. Frydman A., Castner D.G., Schmal M., Campbell C. A method for accurate quantitative XPS analysis of multimetallic or multiphase catalysts on support particles. *J. Catal.* 1995;157(1):133–144. https://doi.org/10.1006/jcat.1995.1274
- 146. Martin J.E., Herzing A.A., Yan W., Li X.-Q., Koel B.E., Kiely C.J., Zhang W.-X. Determination of the oxide layer thickness in core-shell zerovalent iron nanoparticles. *Langmuir*: 2008;24(8):4329–4334. https://doi.org/10.1021/la703689k
- 147. Tunc I., Suzer S., Correa-Duarte M.A., Liz-Marzan L. XPS Characterization of Au(Core)/SiO₂ (Shell) Nanoparticles. *J. Phys. Chem.* B. 2005;109(16):7597–7600. https://doi.org/10.1021/jp050767j
- 148. Diebold U., Pan J.-M., Madey T.E. Growth mode of ultrathin copper overlayers on TiO₂(110). *Phys. Rev. B.* 1993;47(7):3868–3876. https://doi.org/10.1103/PhysRevB.47.3868
- 149. Sharp J.C., Campbell C.T. Quantitative modeling of electron spectroscopy intensities for supported nanoparticles: The hemispherical cap model for non-normal detection. *Surf. Sci.* 2015;632:L5–L8. https://doi.org/10.1016/j. susc.2014.08.010

- 150. Yang D.Q., Gillet J.N., Meunier M., Sacher E. Room temperature oxidation kinetics of Si nanoparticles in air, determined by X-ray photoelectron spectroscopy. *J. Appl. Phys.* 2005;97(2):24303(6 p.). https://doi.org/10.1063/1.1835566
- 151. Vazquez-Pufleau M.A. Simple Model for the High Temperature Oxidation Kinetics of Silicon Nanoparticle Aggregates. *Silicon*. 2021;13(3):189–200. https://doi.org/10.1007/s12633-020-00415-3
- 152. Gillet J.N., Meunier M. General equation for size nanocharacterization of the core-shell nanoparticles by X-ray photoelectron spectroscopy. *J. Phys. Chem. B.* 2005;109(18):8733-8737. https://doi.org/10.1021/jp044322r
- 153. Shard A.G., Wang J., Spencer S.J. XPS Topofactors: Determining Overlayer Thickness on Particles and Fibres. *Surf. Interface Anal.* 2009;41(7):541–548. https://doi.org/10.1002/sia.3044
- 154. Patrone L., Nelson D., Safarov V.I., Sentis M., Marine W. Photoluminescence of silicon nanoclusters with reduced size dispersion produced by laser ablation. *J. Appl. Phys.* 2000;87(8):3829–3837. https://doi.org/10.1063/1.372421
- 155. Hofmeister H., Huisken F., Kohn B. Lattice contraction in nanosized silicon particles produced by laser pyrolysis of silane. *Eur. Phys. J. D.* 1999;9(1–4):137–140. https://doi.org/10.1007/s100530050413
- 156. Werner W.S.M., Smekal W., Powell C.J. Simulation of Electron Spectra for Surface Analysis. Version 2.1 User's Guide. 2017. 134 p. https://doi.org/10.6028/NIST.NSRDS.100-2017. Accessed April 01, 2023.
- 157. Risterucci P., Renault O., Zborowski C., Bertrand D., Torres A., Rueff J.-P., Ceolin D.,Grenet G., Tougaard S. Effective inelastic scattering cross-sections for background analysis in HAXPES of deeply buried layers. *Appl. Surf. Sci.* 2017;402:78–85. https://doi.org/10.1016/j.apsusc.2017.01.046
- 158. Baer D.R., Wang Y.-C., Castner D.J. Use of XPS to Quantify Thickness of Coatings on Nanoparticles. *Micros. Today.* 2016;24(2):40–45. https://doi.org/10.1017/S1551929516000109
- 159. Pauly N., Tougaard S., Yubero F. Modeling of X-ray photoelectron spectra: surface and core hole effects. *Surf. Interface Anal.* 2014;46(10–11):920–923. https://doi.org/10.1002/sia.5372
- 160. Hajati S., Zaporojtchenko V., Faupel F., Tougaard S. Characterization of Au nano-cluster formation on and diffusion in polystyrene using XPS peak shape analysis. *Surf. Sci.* 2007;601(15):3261–3267. https://doi.org/10.1016/j. susc.2007.06.001
- 161. Mansilla C., Gracia F., Martin-Concepcion A.I., Espinós J.P., Holgado J.P., Yubero F., González-Elipe A.R. Study of the first nucleation steps of thin films by XPS inelastic peak shape analysis. *Surf. Interface Anal.* 2007;39(4):331–336. https://doi.org/10.1002/sia.2509
- 162. Mourdikoudis S., Pallares R.M., Thanh N.T.K. Characterization techniques for nanoparticles: comparison and complementarity upon studying nanoparticle properties. *Nanoscale*. 2018;10(27):12871–12934. https://doi.org/10.1039/C8NR02278J
- 163. Baer D.R. Guide to making XPS measurements on nanoparticles. *J. Vac. Sci. Technol. A.* 2020;38(3):031201. https://doi.org/10.1116/1.5141419

164. Baer D.R., Wang Y.-C., Castner D.J. Use of XPS to Quantify Thickness of Coatings on Nanoparticles. *Micros. Today.* 2016;24(2):40–45. https://doi.org/10.1017/S1551929516000109

165. Kjærvik M., Hermanns A., Dietrich P., Thissen A., Bahr S., Ritter B., Kemnitz E., Unger W.E.S. Detection of suspended nanoparticles with near-ambient pressure X-ray photoelectron spectroscopy. *J. Phys.: Condens. Matter.* 2017;29(47):474002(9 p.). https://doi.org/10.1088/1361-648x/aa8b9d

About the authors:

Anatoly A. Ischenko, Dr. Sci. (Chem.), Professor, Head of the I.P. Alimarin Department of Analytical Chemistry, M.V. Lomonosov Institute of Fine Chemical Technologies, MIREA – Russian Technological University (86, Vernadskogo pr., Moscow, 119571, Russia). E-mail: aischenko@yasenevo.ru. Scopus Author ID 6701507307, ResearcherID B-2767-2014, https://orcid.org/0000-0003-1532-377X

Mikhail A. Lazov, Cand. Sci. (Chem.), Assistant Professor, I.P. Alimarin Department of Analytical Chemistry, M.V. Lomonosov Institute of Fine Chemical Technologies, MIREA – Russian Technological University (86, Vernadskogo pr., Moscow, 119571, Russia). E-mail: lazovm@gmail.com. Scopus Author ID 56466030700, https://orcid.org/0000-0001-8578-1683

Elena V. Mironova, Senior Lecturer, I.P. Alimarin Department of Analytical Chemistry, M.V. Lomonosov Institute of Fine Chemical Technologies, MIREA – Russian Technological University (86, Vernadskogo pr., Moscow, 119571, Russia). E-mail: mironova.ev.mitht@yandex.ru. https://orcid.org/0000-0001-8213-7059

Alexey Yu. Putin, Cand. Sci. (Chem.), Assistant Professor, Department of General Chemical Technology, M.V. Lomonosov Institute of Fine Chemical Technologies, MIREA – Russian Technological University (86, Vernadskogo pr., Moscow, 119571, Russia). E-mail: putin@mirea.ru. https://orcid.org/0000-0003-1333-7318

Andrey M. Ionov, Dr. Sci. (Phys.-Math.), Professor, Leading Researcher, Osipyan Institute of Solid State Physics, Russian Academy of Sciences (2, Akademika Osip'yana ul., Chernogolovka, Moscow oblast, 142432, Russia). E-mail: ionov@issp.ac.ru. https://orcid.org/0000-0002-2094-1065

Pavel A. Storozhenko, Academician at the Russian Academy of Sciences, Dr. Sci. (Chem.), Professor, Scientific Director of State Scientific Research Institute of Chemistry and Technology of Organoelement Compounds (38, Entuziastov shosse, Moscow, 111123, Russia). E-mail: bigpastor@mail.ru. Scopus Author ID 9633186700, ResearcherID D-4645-214

Об авторах:

Ищенко Анатолий Александрович, д.х.н., профессор, заведующий кафедрой аналитической химии им. И.П. Алимарина Института тонких химических технологий им. М.В. Ломоносова ФГБОУ ВО «МИРЭА – Российский технологический университет» (119571, Россия, Москва, пр-т Вернадского, д. 86). E-mail: aischenko@yasenevo.ru. Scopus Author ID 6701507307, ResearcherID B-2767-2014, https://orcid.org/0000-0003-1532-377X

Лазов Михаил Александрович, к.х.н., ассистент кафедры аналитической химии им. И.П. Алимарина Института тонких химических технологий им. М.В. Ломоносова ФГБОУ ВО «МИРЭА – Российский технологический университет» (119571, Россия, Москва, пр-т Вернадского, д. 86). E-mail: lazovm@gmail.com. Scopus Author ID 56466030700, https://orcid.org/0000-0001-8578-1683

Миронова Елена Валерьевна, старший преподаватель кафедры аналитической химии им. И.П. Алимарина Института тонких химических технологий им. М.В. Ломоносова ФГБОУ ВО «МИРЭА – Российский технологический университет» (119571, Россия, Москва, пр-т Вернадского, д. 86). E-mail: mironova.ev.mitht@yandex.ru. https://orcid.org/0000-0001-8213-7059

Путин Алексей Юрьевич, к.х.н., доцент кафедры общей химической технологии Института тонких химических технологий им. М.В. Ломоносова ФГБОУ ВО «МИРЭА – Российский технологический университет» (119571, Россия, Москва, пр-т Вернадского, д. 86). E-mail: putin@mirea.ru. https://orcid.org/0000-0003-1333-7318

Ионов Андрей Михайлович, д.ф.-м.н., профессор, ведущий научный сотрудник, ФГБУН «Институт физики твердого тела им. Ю.А. Осипьяна» Российской академии наук (142432, Россия, Московская обл., г. Черноголовка, ул. Академика Осипьяна, д. 2). E-mail: ionov@issp.ac.ru. https://orcid.org/0000-0002-2094-1065

Стороженко Павел Аркадъевич, академик РАН, д.х.н., профессор, научный руководитель ГНЦ РФ АО «Государственный научно-исследовательский институт химии и технологии элементоорганических соединений» (111123, Россия, Москва, шоссе Энтузиастов, д. 38). E-mail: bigpastor@mail.ru. Scopus Author ID 9633186700, ResearcherID D-4645-214

The article was submitted: June 06, 2022; approved after reviewing: November 07, 2022; accepted for publication: March 27, 2023.

Translated from Russian into English by H. Moshkov

 $MIREA-Russian\ Technological\ University$ МИРЭА – Российский технологический университет 78, Vernadskogo pr., Moscow, 119454, Russian Federation. Publication date *April 30, 2023.* 119454, РФ, Москва, пр-т Вернадского, д. 78. Дата опубликования *30.04.2023*. Not for sale Не для продажи

www.fine chem‐mirea.ru

